Digital copy produced with permission of the author.

Julkaisu digitoitu tekijän luvalla.

Lappeenrannan teknillinen yliopisto
Lappeenranta University of Technology

Kari Leinonen

FABRICATION AND CHARACTERIZATION OF SILICON POSITION SENSITIVE PARTICLE DETECTORS

Acta Universitatis
Lappeenrantaensis 235

ISBN 952-214-142-9 (PDF)

LAPPEENRANTA
UNIVERSITY OF TECHNOLOGY

Kari Leinonen

FABRICATION AND CHARACTERIZATION OF SILICON POSITION SENSITIVE PARTICLE DETECTORS

Thesis for the degree of Doctor of Science (Technology) to be presented with due permission for public examination and criticism in the Auditorium 1383 at Lappeenranta University of Technology, Lappeenranta, Finland on the 10th of February, 2006, at noon.

Acta Universitatis
Lappeenrantaensis
235

Supervisor Professor Tuure Tuuva
Department of Electrical Engineering
Lappeenranta University of Technology
Lappeenranta
Finland

Reviewers Professor Hartmut F.-W. Sadrozinski
Physics Department
University of California Santa Cruz
Santa Cruz
USA

PhD Risto Punkkinen
Department of Information Technology
University of Turku
Turku
Finland

Opponent Professor Hartmut F.-W. Sadrozinski
Physics Department
University of California Santa Cruz
Santa Cruz
USA

ISBN 952-214-141-0
ISBN 952-214-142-9 (PDF)
ISSN 1456-4491

Lappeenrannan teknillinen yliopisto
Digipaino 2006

Abstract

Kari Leinonen

Fabrication and characterization of silicon position sensitive particle detectors

Lappeenranta 2006

91 p.

Acta Universitatis Lappeenrantaensis 235

Diss. Lappeenranta University of Technology

ISBN 952-214-141-0, ISBN 952-214-142-9 (PDF), ISSN 1456-4491

Position sensitive particle detectors are needed in high energy physics research. This thesis describes the development of fabrication processes and characterization techniques of silicon microstrip detectors used in the work for searching elementary particles in the European center for nuclear research, CERN. The detectors give an electrical signal along the particles trajectory after a collision in the particle accelerator. The trajectories give information about the nature of the particle in the struggle to reveal the structure of the matter and the universe. Detectors made of semiconductors have a better position resolution than conventional wire chamber detectors. Silicon semiconductor is overwhelmingly used as a detector material because of its cheapness and standard usage in integrated circuit industry.

After a short spread sheet analysis of the basic building block of radiation detectors, the pn junction, the operation of a silicon radiation detector is discussed in general. The microstrip detector is then introduced and the detailed structure of a double-sided ac-coupled strip detector revealed.

The fabrication aspects of strip detectors are discussed starting from the process development and general principles ending up to the description of the double-sided ac-coupled strip detector process.

Recombination and generation lifetime measurements in radiation detectors are discussed shortly. The results of electrical tests, ie. measuring the leakage currents and bias resistors, are displayed. The beam test setups and the results, the signal to noise ratio and the position accuracy, are then described.

It was found out in earlier research that a heavy irradiation changes the properties of radiation detectors dramatically. A scanning electron microscope method was developed to measure the electric potential and field inside irradiated detectors to see how a high radiation fluence changes them. The method and the most important results are discussed shortly.

Keywords: high energy physics, particle detector, double-sided fabrication, strip detector, scanning electron microscope, voltage-contrast

UDC 539.1.073 : 546.28

Acknowledgements

The research work for the first three publications included in this thesis was carried out in the Semiconductor Laboratory of Technical Research Center of Finland (VTT), later in a new organization a part of VTT Electronics. The development of radiation detectors started in 1989 for a project "Development of an energy dispersive silicon radiation detector" funded by Technology Development Center of Finland (TEKES), the industrial partner being Outokumpu Electronics Oy (later known as Metorex International Oy and now a part of Oxford Instruments). The research work for the project was performed in VTT and in the Research Institute for High Energy Physics (SEFT) at Helsinki University.

After the initial development period the work with radiation detectors continued in 2004 in the Department of Electrical Engineering at Lappeenranta University of Technology (LUT) with the aim to improve the radiation tolerance of the detectors in the framework of CERN (the European Organization for Nuclear Research) RD50 project.

I thank my supervisor, Professor Tuure Tuuva, for his continuous interest on this work during all these years. He pushed us to develop and fabricate the first Finnish position sensitive silicon radiation detectors for high energy physics applications for CERN, almost forced us to continue the process development to be finally capable of fabricating the worlds first double-sided ac-coupled strip detectors with integrated bias resistors and coupling capacitors and selling them to CERN, and invited me to Lappeenranta University of Technology to continue the work for detector development and to finish my dissertation. I am also grateful for the relaxed working atmosphere in the Microelectronics Laboratory at LUT and the academic freedom to do this work independently on time and location utilizing modern telecommunication.

It is too late to thank Dr. Tapio Wiik, the leader of the Silicon Technology group in VTT until year 2000, for creating the excellent working environment including all the necessary equipment and all the necessary professionals. But it is not too late to thank these professionals: Hannu Ronkainen being a continuous source of new ideas, Markku Orpana and Sami Franssila developing the dry etching processes, Teija Häkkinen and Tuula Virolainen co-operating in the development of the processing practices, Risto Hautakoski, Ari Häärä, Kalle Komsi, Risto Salo and Jyrki Repo maintaining and improving the mechanical and electrical systems, Martti Blomberg, Simo Eränen and Jyrki Kiihamäki for sound criticism against everything and Arto Salin providing top quality photo masks. Also I wish to thank Mikael Anderson, Kaj Grahn, Marko Grönlund and Helena Pohjonen from the IC design group of VTT for simulating and designing many detector structures.

I thank Professors Juha Sinkkonen and Pekka Kuivalainen from Helsinki University of Technology for organizing interesting post graduate courses in microelectronics.

Many thanks are due to Jaakko Härkönen, the leader of CERN RD50 Pad Detector Characterization group, for valuable comments, and to Tanja Palviainen from LUT Microelectronics Laboratory for enthusiastic co-operation especially in electrical simulations.

Finally I would like to gratefully acknowledge Juha Pyrhönen, the head of LUT Electrical Engineering department, and Jarmo Partanen, the head of the Graduate School of Electrical Engineering, for supporting this work and North Karelia Polytechnic, Information Technology, and its current leader Jyri Roihuvuo for providing the facilities for scanning electron microscopy during the past year.

Joensuu, October 2005

Kari Leinonen

List of Publications

I Iiro Hietanen, Jukka Lindgren, Risto Orava, Tuure Tuuva, Richard Brenner, Mikael Andersson, Kari Leinonen, Hannu Ronkainen, Ion-implanted silicon detectors processed on a 100 mm wafer, Nuclear Instruments and Methods in Physics Research A 301 (1991), pp. 116-120.

II Iiro Hietanen, Jukka Lindgren, Risto Orava, Tuure Tuuva, Martti Voutilainen, Richard Brenner, Mikael Andersson, Kari Leinonen, Hannu Ronkainen, Ion-implanted capacitively coupled silicon strip detectors with integrated polysilicon bias resistors processed on a 100 mm wafer, Nuclear Instruments and Methods in Physics Research A 310 (1991), pp. 671-676.

III Richard Brenner, Iiro Hietanen, Jukka Lindgren, Risto Orava, Camilla Rönnqvist, Tom Schulman, Tuure Tuuva, Mikael Andersson, Kari Leinonen, Hannu Ronkainen, Double-Sided Capacitively Coupled Silicon Strip Detectors on a 100 mm wafer, Nuclear Instruments and Methods in Physics Research A 315 (1992), pp. 502-506.

IV Kari Leinonen, Investigation of Voltages and Electric Fields in Silicon Radiation Detectors using a Scanning Electron Microscope, Nuclear Instruments and Methods in Physics Research A 555 (2005), pp. 411-419.

V Kari Leinonen, Tanja Palviainen, Tuure Tuuva, Esa Tuovinen, Jaakko Härkönen, Panja Luukka, Investigation of type inversion of n-bulk in 10 MeV proton irradiated FZ silicon detectors using a scanning electron microscope, Nuclear Instruments and Methods in Physics Research A 552 (2005), pp. 357-363.

VI Kari Leinonen, Patterning large area devices with a 5:1 reduction stepper, Nuclear Instruments and Methods in Physics Research A 555 (2005), pp. 59-64.

Contents

Abstract

Acknowledgements

List of Publications

Contents

Nomenclature

1 Introduction **13**

1.1 CERN ... 13

1.2 Particle physics ... 14

1.3 Accelerators and detectors ... 20

1.3.1 LEP and DELPHI ... 23

1.3.2 LHC ... 25

1.4 Luminosity requirements ... 27

1.5 Summary of publications ... 29

2 Semiconductor particle detectors **31**

2.1 Basic analysis of a pn junction ... 31

2.2 Operation of a silicon radiation detector ... 38

2.3 The microstrip detector ... 40

3 Fabrication of particle detectors 47

3.1 Development of the process parameters 48

3.1.1 The Kemmer principle 50

3.1.2 Oxidation 51

3.1.3 Gettering 52

3.2 The double-sided strip detector process 53

3.2.1 Wafer cleaning 54

3.2.2 Two-sided lithography 56

3.2.3 Using a wafer stepper 56

3.2.4 Polysilicon resistors 59

3.2.5 The process 60

4 Characterization 67

4.1 Lifetime measurement 67

4.2 Electrical tests 69

4.3 Beam tests 71

4.4 SEM measurements 74

5 Conclusions 87

References 89

Nomenclature

<100> crystal orientation

<111> crystal orientation

A area

AD analogue to digital

ADC analogue to digital converter

BHF buffered HF acid

c velocity of light, $2.998 \cdot 10^{8}$ m/s

c donor removal coefficient during irradiation

C capacitance

C contrast in voltage-contrast measurements

CMOS complementary metal oxide semiconductor

CVD chemical vapor deposition

CZ Czochralski

d depth

DI de-ionized

e elementary charge, $1.6021 \cdot 10^{-19}$ As

eV electron volt, $1\ \text{eV} = 1.6021 \cdot 10^{-19}$ J

E energy

E electric field

EBIC electron beam induced current

E_P energy required to generate an electron-hole pair

E_{PGe} energy required to generate an electron-hole pair in germanium

E_{PSi} energy required to generate an electron-hole pair in silicon

E13 replacement for the scientific notation 10^{13} (for instance)

fb femtobarn, $1\ \text{fb} = 10^{-39}\ \text{cm}^2$

F Fano factor

FWHM full width at half maximum

FZ float zone

i abbreviation for minute

ii abbreviation for minute expressed with two numbers

I	current
I_g	generation current
I_l	leakage current
I_r	reverse current
k	Boltzmann constant, $1.38 \cdot 10^{-23}$ J/K
K	contrast scaling factor
LEP	Large Electron Positron Collider
LHC	Large Hadron Collider
LSI	large scale integration
LTO	low temperature oxide
m	mass
M	voltage constant in voltage-contrast measurements
MOS	metal-oxide-semiconductor
n_i	intrinsic concentration of holes and electrons, $1.45 \cdot 10^{10}$ cm^{-3} (Si, 300 K)
n	electron concentration
n	neutron
N	dopant concentration
N_A	acceptor concentration
N_D	donor concentration
N_{eff}	effective doping density
$N_{eff,0}$	effective doping concentration before irradiation
OBIC	optical beam induced current
p	hole concentration
p	proton
pb	picobarn, 1 pb = 10^{-36} cm^2
PMOS	p-channel MOS
q	elementary charge, $1.6021 \cdot 10^{-19}$ As
Q	quality factor of a capacitor
Q_S	collected charge
Q_{SS}	surface state density
RMS	root mean square
sigma	standard deviation
SCSI	space charge sign inversion
SEM	scanning electron microscope

T	absolute temperature
TCT	transient current technique
V	voltage
V_0	built-in potential of a pn junction
V_a	applied voltage over the pn junction
V_{dep}	depletion voltage
V_T	voltage equivalent of temperature, $V_T = kT/q$
W	thickness of the wafer or the diode
x	distance
x	number of pixels in horizontal direction or x-position
x_j	junction depth
x_d	length of the depletion layer in x-direction
x_n	length of the depletion layer in the n-side
x_p	length of the depletion layer in the p-side
y	number of lines or number of pixels in vertical direction or y-position

Greek letters

β	acceptor introduction rate during irradiation
ε	permittivity, dielectric constant
ε_0	permittivity of vacuum, $8.854 \cdot 10^{-12}$ F/m
ε_s	permittivity of semiconductor
ε_{Si}	permittivity of silicon, $11.7 \cdot \varepsilon_0$
Φ	radiation fluence
Λ	volume
μ_n	mobility of electrons, 1350 cm^2/Vs (Si, 300 K)
ρ	resistivity
σ	conductivity
τ	lifetime

Chapter 1

Introduction

1.1 CERN

The main objective of this thesis are radiation detectors for high energy physics experiments done in CERN (the acronym stands for the council "Conseil Européen pour la Recherche Nucléaire", that was founded in 1951 and decided to build a central laboratory near Geneva Switzerland).

CERN is the European Organization for Nuclear Research, the world's largest **particle physics** centre. Here physicists come to explore what matter is made of and what forces hold it together. CERN exists primarily to provide them with the necessary tools. These are **accelerators**, which accelerate particles to almost the speed of light and **detectors**, which make the particles visible.

The CERN laboratory was one of Europe's first joint ventures and includes now 20 member states. The current member states are shown in figure 1.1: Austria, Belgium, Bulgaria, the Czech Republic, Denmark, Finland, France, Germany, Greece, Hungary, Italy, The Netherlands, Norway, Poland, Portugal, the Slovak Republic, Spain, Sweden, Switzerland and the United Kingdom. Finland joined CERN in January 1991, and 87 people were involved in 2003.

Member states have special duties and privileges. They make a contribution to the capital and operating costs of the CERN programmes, and are represented in the Council, responsible for all important decisions about the organization and its activities.

Some states (or international organizations) for which membership is either not possible or not yet feasible are observers. Observer status allows non-member states to attend Council meetings and to receive Council documents, without taking part in the decision-making procedures of the organization. Observer states and organizations currently involved in CERN programmes are: the European Commission, India, Israel, Japan, the Russian Federation, Turkey, UNESCO and the USA.

Scientists from 220 institutes and universities of non-members states also use CERN's facilities. Non-member states currently involved in CERN programmes are: Algeria, Argentina, Armenia, Australia, Azerbaijan, Belarus, Brazil, Canada, China, Croatia, Cyprus, Estonia, Georgia, Iceland, India, Iran, Ireland, Mexico, Morocco, Pakistan, Peru, Romania, Serbia, Slovenia, South Africa, South Korea, Taiwan and the Ukraine.

Physicists and their funding agencies from both member and non-member states are responsible for the financing, construction and operation of the experiments on which they collaborate. CERN spends much of its budget on building new machines (such as the Large Hadron Collider), and it can only partially contribute to the cost of the experiments.

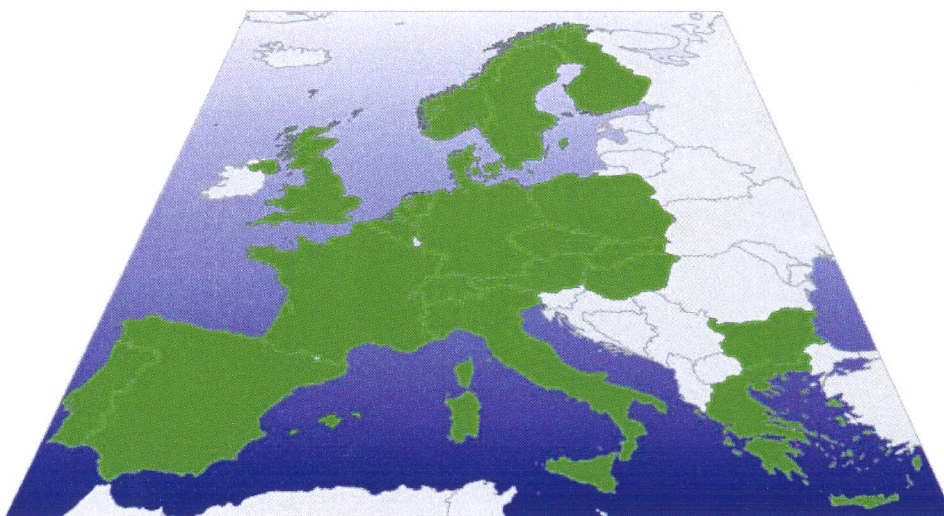

Figure 1.1 The current member states of CERN (http://public.web.cern.ch/Public/Content/Chapters/AboutCERN/WhatIsCERN/InvolvedCountries/InvolvedCountries-en.html).

Countries spend some fraction of their gross national product on fundamental research, but there are fields where the equipment needed is so expensive that it can be put together only with international efforts and collaboration. For particle physics, even the larger European countries could not afford to construct a laboratory as big as CERN, and the human resources to run it could not be found within a single nation. CERN was founded thanks to the joint efforts of 12 European States. Nowadays, thanks to this venture, most of the European countries have the chance to participate in the world's most advanced physics experiments without consuming an unacceptable fraction of their national science budget.

CERN employs just under 3000 people, representatives of a wide range of skills - physicists, engineers, technicians, craftsmen, administrators, secretaries, workmen. Some 6500 visiting scientists, half of the world's particle physicists, come to CERN for their research. They represent 500 universities and over 80 nationalities.

1.2 Particle physics

Everything in the Universe is made up from a small number of basic building blocks called **elementary particles**, governed by a few **fundamental forces**. Some of these particles are stable and form the normal matter, the others live for fractions of a second and then decay to the stable ones. All of them coexisted for a few instants after the Big Bang at the origin of our Universe. Since then, only the enormous concentration of energy that can be reached in an accelerator at CERN can bring them back to life. Therefore, studying particle collisions is like "looking back in time", recreating the environment present at the origin of the Universe.

The idea that matter should be made out of fundamental building blocks is more then 2000 years old. The blocks were assumed to be simple and structureless and not made of anything smaller.

"... the nature of the perpetual things consist of small particles infinite in number... the particles are so small as to be imperceptible to us, and take all kinds of shapes and all kinds of forms and differences of size. Out of them, like out of elements (earth, air, fire, water) he now lets combine and originate the visible and perceptible bodies..." (Democritus ~ 450 B.C.)

We know today that all matter in the Universe is built from nearly a hundred different types of **atoms** (see figure 1.2), each one made up of **electrons** (yellow in figure 1.2) with negative electric charge circulating a positively charged **nucleus**. The nucleus itself further consists of nucleons: positive **protons** (red in figure 1.2) and neutral **neutrons** (blue in figure 1.2). Physicists call all these components of matter **particles**.

The electron seems to have no internal structure. Protons and neutrons are composite particles, each containing three **quarks** (green in figure 1.2). Like the electron, the quarks appear to have no structure. Only two types of quark, called "up" and "down", are needed to build the proton and the neutron.

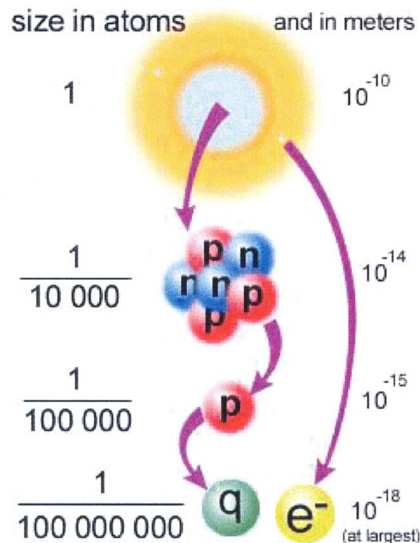

Figure 1.2. The picture shows a simple model of an atom and how it would look like if we would penetrate deeper and deeper into it. The scales of the picture are not correct (http://hands-on-cern.physto.se/hoc_v21en/index.html).

The nucleus of the atom consists of protons and neutrons. These are built up of quarks, which are tied to each other by the strong interaction mediated by gluons. The nucleus is very small, only about 1/10000 of the diameter of the atom. The structure of protons and neutron is displayed in figure 1.3.

One more structureless particle must be added to complete the picture: a neutral and very light particle called the **neutrino**. It plays a vital role in reactions that convert neutrons to protons and vice versa. Such reactions allow matter to stay in the stable form we observe and are also important in fuelling the Sun and the other stars.

These four particles are all we need to build the ordinary matter around us: the electron, the up-quark and the down-quark and the neutrino.

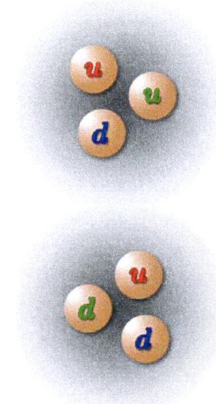

Figure 1.3. On top the proton (with quarks uud) and below the neutron (udd) (http://hands-on-cern.physto.se/hoc_v21en/index.html).

In fact, there are less ordinary forms of matter that exist which we can't see: cosmic matter coming from the space, high energy matter that is created in the accelerator and the "mirror image" of all of it, antimatter. To include them in the picture, we need a more general description and more particles.

The Standard Model summarises current understanding of fundamental particles and the forces that act between them. The Standard Model describes how matter is built up of a group of elementary particles. It also explains how another group of particles, the so called force carriers, affects other particles through different kinds of interactions, and forms all structures in the micro cosmos.

The Standard Model describes two basic types of particles (tables 1.1 and 1.2):

Matter particles:	6 quarks
	6 leptons
Force carriers:	1 photon
	3 vector bosons
	8 gluons

The Standard Model also includes the so called *Higgs particle*, which is thought to be responsible for the different masses of the particles. The quarks and leptons also have corresponding *anti particles*. The most important difference between a particle and its corresponding anti particle is that their electrical charges have opposite signs.

The word lepton comes from the Greek "light" (opposite to heavy). The six leptons are all elementary, meaning they are not composed of other components. The three charged leptons are the electron (e^-), the muon (μ^-) and the tau (τ^-). Their antiparticles have a positive charge (+1 elementary charge). The three neutral leptons are: the electron-neutrino (ν_e), the muon-neutrino (ν_μ) and the tau-neutrino (ν_τ). Also the neutrinos have their antiparticles. They are different from the neutrinos through so-called inner quantum numbers.

The muons (μ^+ and μ^-) are created in the cosmic radiation that constantly bombards the earth's atmosphere. The major part of this radiation consists of protons, which produce new particles (most often pi-mesons) in the collision with the molecules of the atmosphere. These particles decay into (among other things) muons. The muons also decay rapidly into other particles (e^+, e^- and neutrinos).

Table 1.1. The Matter Particles described by the Standard Model.

Matter particles		
quarks	up	u
	down	d
	charm	c
	strange	s
	top	t
	bottom	b
leptons	electron neutrino	ν_e
	electron	e
	muon neutrino	ν_μ
	muon	μ
	tau neutrino	ν_τ
	tau	τ

Table 1.2. The Force Carriers described by the Standard Model.

Force carriers	
photon	γ
vector bosons	W^+, W^-, Z^0
gluons (8)	g

The tau particle was discovered in the 1970's in experiments with highly energetic particle collisions (between electrons and positrons with a total energy of about 5 GeV). The properties of the tau particle are similar to the properties of the electron, but it has a much greater mass (3500 times higher). Therefore it decays into other lighter particles (to other leptons or to one or more hadrons).

The three other leptons, the neutrinos, are among the particles that are most difficult to observe. They have no electrical charge and only a very small mass. They react very seldom with matter and are therefore virtually undetectable.

The Standard Model divides *quarks* and *leptons* into three groups, so called families. Table 1.3 gives an overview showing the labels and electrical charges of the matter particles in units of the electron charge *e*. Note that quarks have charges in fractions of *e*, while the three charged leptons have the same charge as the electron (-*e*, or shorter, -1).

Table 1.3. The charges of quarks and leptons.

family	quarks		leptons	
1	u	d	ν_e	e
	+2/3	-1/3	0	-1
2	c	s	ν_μ	μ
	+2/3	-1/3	0	-1
3	t	b	ν_τ	τ
	+2/3	-1/3	0	-1

All matter that we see in our surroundings is built up of u and d quarks and of electrons. These three belong to the first family. All three families were important in the very early universe, but since then the particles in the second and third family have decayed into particles of the first family.

All quarks interact with each other through the strong interaction. Quarks are combined together into particles called hadrons (Greek hadros = strong). The name comes from the fact that the strong interaction is used when hadrons interact with each other. Hadrons are divided into two groups of particles. Particles built up of three quarks (or three antiquarks) are called baryons (Greek baros = heavy). Neutrons and protons belong to this group of heavy particles. Particles built up of two quarks (one quark and one antiquark) are called mesons (Greek mesos = medium/middle). There are no hadrons consisting of a single quark, and at the present we have no evidence of hadrons containing more than three quarks. The quarks in the first family build up the atomic nuclei in the universe. The four remaining quarks (and their antiquarks) are used as building blocks for short-lived particles that do exist in our natural environment. But they existed in great numbers at the birth of the universe and they are recreated at physics experiments with high energy particle collisions.

Three forces act in the micro cosmos. They interact directly between quarks and leptons at this level. The Standard Model describes the different interactions with the help of force carrying particles. The three types of interaction are:

the strong interaction (acts on quarks; mediated by the eight gluons)
the weak interaction (acts on both quarks and leptons; mediated by the three vector bosons W^+, W^- and Z^0)
the electromagnetic interaction (acts on charged particles; mediated by the photon)

There is a fourth type of interaction that is not a part of the Standard Model: gravity. It is supposed to be mediated by the graviton (not yet discovered). The gravity between single particles is so weak that it is negligible in micro cosmos.

The relative strengths and ranges of interaction are given in table 1.4. The gravity is much weaker than the others, even compared to the weak interaction, and it does not play any important role in the world of particles.

Table 1.4. The relative strength of the four interactions. The strength is normalised to 1 for the strong interaction. (http://hyperphysics.phy-astr.gsu.edu/hbase/forces/funfor.html)

type	strength	range	mediator
strong	1	10^{-15} m	gluons (8)
electromagnetic	10^{-2}	∞	photon
weak	10^{-6}	10^{-18} m	W^+, W^-, Z^0
gravity	10^{-38}	∞	graviton

Among the force carrying particles it is only the three vector bosons of the weak interaction that have mass. The others, the photon and the eight gluons, are all massless. The quarks and the leptons all have different masses. The three neutral leptons, the neutrinos, have a very small mass. Until recently it was believed that they were massless.

The masses of the particles are given in the unit *electron volt*, which is written as eV.
An electron gains an energy of one eV, when it is accelerated with a voltage of one V.
1 eV equals $1.6021 \cdot 10^{-19}$ J (joule).

Energy takes the form as, among other things, kinetic energy and mass. In 1905 *Albert Einstein* derived an equation for the relation between mass and energy:

$$E = m c^2 \quad , \qquad (1\text{-}1)$$

where E = energy, m = mass and c = the speed of light in vacuum. The equation tells how much energy is needed to create a particle of mass *m*. Conversely mass can be converted to energy. For example when a particle and an anti-particle are destroyed when they meet (annihilation), or when an unstable particle decays into other particles and a small part of the mass becomes energy. Table 1.5 shows the masses of elementary particles. It also tells how much energy is needed to create them.

Table 1.5. Elementary particles with masses expressed in electron volts. (http://particleadventure.org/particleadventure/frameless/chart.html)

quarks		leptons	
u 3 MeV	d 6 MeV	ν_e < 10 eV	e 511 keV
c 1.3 GeV	s 100 MeV	ν_μ < 200 keV	μ 106 MeV
t 175 GeV	b 4.3 GeV	ν_τ < 20 MeV	τ 1.78 GeV

vector bosons		
W^+ 80 GeV	W^- 80 GeV	Z^0 91 GeV

1.3 Accelerators and detectors

Particles are extremely tiny, and to be able to see and study them, scientists need very special tools. They need **accelerators**, huge machines able to speed up particles to very high energies before smashing them into other particles. Around the points where the smashing occurs, scientists build **experiments** which allow them to observe and study the collisions. These are instruments, sometimes huge, made of several kinds of **particle detectors**. By accelerating and smashing particles, physicists can identify their components or create new particles, revealing the nature of the interactions between them.

The accelerator complex at CERN, displayed in figure 1.4, is a succession of machines with increasingly higher energies, injecting the beam each time into the next one, which takes over to bring the beam to an energy even higher, and so on. The flagship of the complex will be the Large Hadron Collider (LHC).

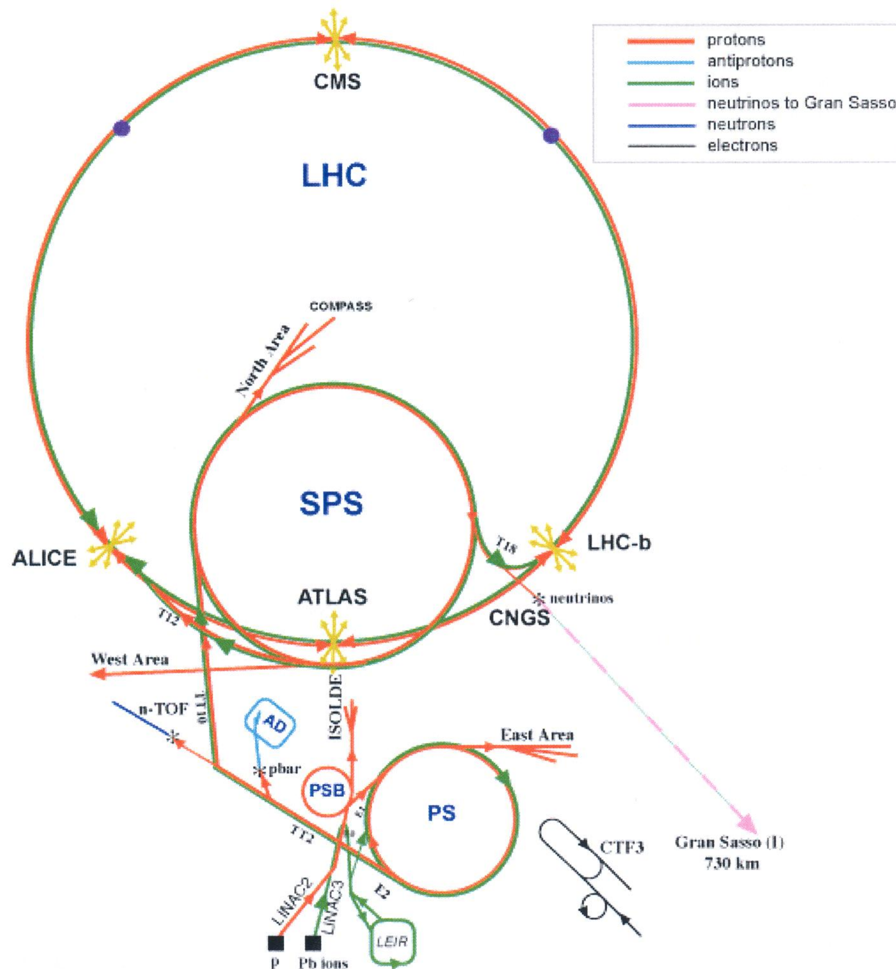

Figure 1.4. The CERN accelerator complex. The circumference of the LHC ring is 27 km (http://public.web.cern.ch/Public/Content/Chapters/AboutCERN/HowStudyPrtcles/CERNAccelComplex/CERNAccelComplex-en.html).

Physicists smash particles into each other with two main objectives:

to find out what is inside them

to use the energy available in the collision to create new particles.

For each **collision**, which is called an **event**, the physicist's goal is to **count**, **trace** and **characterize** all the different particles that were produced and fully **reconstruct** the process. However, particles are extremely small, too small for even the strongest microscope to observe. So physicists need instruments more sensitive and specialized, called **particle detectors**. These consist of many different pieces of equipment, each one able to recognize and measure a special set of particle proprieties, such as charge, mass and energy.

As displayed in figures 1.5 and 1.6 primarily three kinds of subdetectors are used at particle physics experiments:

Closest to the collision point are track detectors that show the trajectories and scattering angles of charged particles.

Outside the track detectors are calorimeters that measure the energy of both charged and neutral particles.

Furthest from the collision point are muon detectors that identify muons.

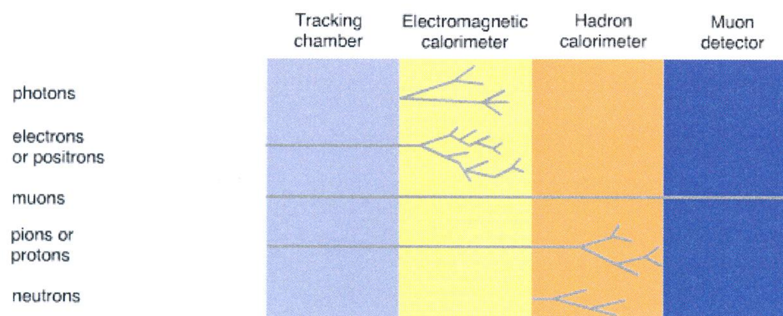

Figure 1.5. A schematic diagram of the layers of a particle detector (http://public.web.cern.ch/Public/Content/Chapters/AboutCERN/HowStudyPrtcles/HowSeePrtcles/HowSeePrtcles-en.html).

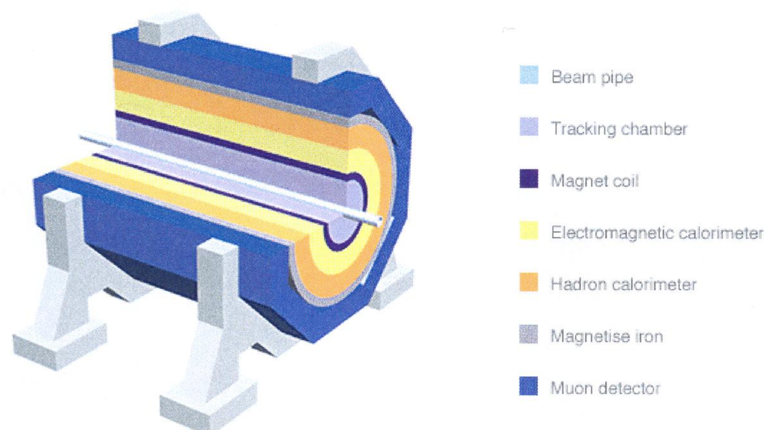

Figure 1.6. A three-dimensional presentation of a particle detector (http://public.web.cern.ch/Public/Content/Chapters/AboutCERN/HowStudyPrtcles/HowSeePrtcles/HowSeePrtcles-en.html).

Tracking chambers make the paths of the particles, the tracks, directly visible. Just the track of the particle gives a lot of useful information, especially if the detector is placed inside a magnetic field: the charge of the particle, for instance, will be obvious since particles with positive electric charge will bend one way and those with negative charge will bend the opposite way. Also the momentum of the particle (the 'quantity of motion', which is equal to the product of the mass by the velocity) can be determined: very high momentum particles travel in almost straight lines, low momentum particles make tight spirals.

Early research in particle physics used, for instance, detectors called cloud chambers, where trails of droplets form along the tracks left by particles, rather like the vapour trails of aeroplanes. In a bubble chamber, particles leave trails of bubbles in a liquid. In a spark chamber, sparks occur when a gas is ionized by a passing particle. Most modern tracking devices do not make the tracks of particles directly visible. Instead, they produce tiny electrical signals that can be recorded as computer data. A computer program then reconstructs the patterns of tracks recorded by the detector, and displays them on a screen as shown in the example of figure 1.7.

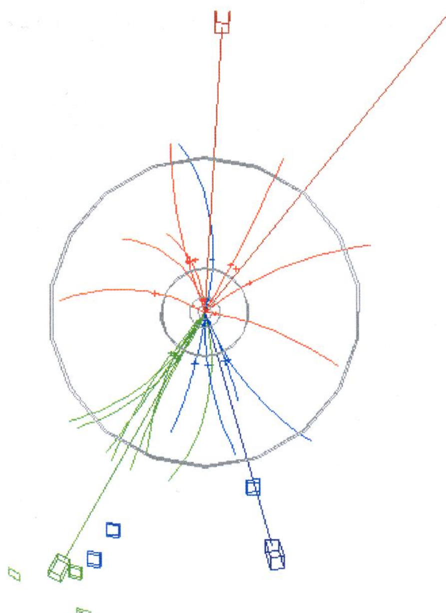

Figure 1.7. An end view of tracks of particles in DELPHI run 83024 event 05850 year 1998.
A screen dump of WIRED program (http://hands-on-cern.physto.se/wired/ch/cern/wired/html/z0_1998_01.html).

Track detectors can be dived into two main types: semiconductor detectors and wire chambers. Semiconductor detectors consist of silicon or some other kind of semiconducting material, while wire chambers are built up of gas filled chambers interspaced with wires. Common for both types is that only charged particles can be detected. Neutral particles traverse the tracking detectors undetected.

Wire chambers are based on the idea that charged particles can be registered when they traverse through a gas. The particles will collide with the atoms in the gas and knock out electrons from the atoms. This is called ionisation since the atoms become ions. An electrical potential makes the electrons move to the anode and the ions to the cathode. The electrons will then be registered as an electrical current.

A multi wire proportional chamber (MWPC), one type of track detectors used in modern particle experiments, has several anode wires attached between two cathode planes. The distance between the anode wires is about 2 mm and the distance between the cathode planes is about 2 cm. The particles way through the chamber can be calculated using the positions of the anode wires. Several chambers are positioned at a distance from each other to register tracks of the charged particles.

Another type of track detectors is based on semiconductors. When a charged particle hits a semiconductor is an electron-hole pair created in the semiconductor. By applying an electrical field in the semiconductor do the electrons and the holes separate. These are collected at the electrodes, which gives a measurable signal.

The greatest advantage with semiconductor detectors is their high precision; they can register the position of particles with an accuracy of the order of 10 μm. Among the drawbacks are that they are sensitive to radiation and expensive to produce.

Semiconductor detectors are located closest to the particle collision, inside the wire chambers, since it is there one has the greatest advantage of their high precision to locate the positions of particle tracks. One usage is to study short-lived particles.

However, more information is needed and usually a tracking device is associated with a calorimeter. Calorimeters stop and fully absorb most of the particles, providing a measurement of their energy. Muons and neutrinos are often the only particles capable of escaping a calorimeter.

Muons can hardly be stopped, but at least they can be identified: special muon detectors are located outside the calorimeter, and only muons can emerge and leave a track there.

Neutrinos, by contrast, escape and do not even leave a track, going through all the detectors undetected. However, as they are the only known particles that can escape, their presence can be inferred from an imbalance of the initial and final energies of the event.

Assembling all the pieces of information from each track, physicists can fully characterize each particle, and by arranging all the tracks coming from a collision, they can reconstruct the event with a great precision.

1.3.1 LEP and DELPHI

The biggest electron accelerator built so far is LEP (Large Electron Positron Collider) at CERN. Its circumference is 27 kilometers and the whole accelerator is situated more than 100 meters below ground. LEP is a collider where the two particle beams consist of electrons and positrons (anti electrons) respectively. The beams of particles are accelerated in opposite directions in orbits next to each other inside the beam tube. There after the beams are made to collide with each other.

The operation of the LEP collider at CERN started in August 1989 opening a new chapter in the history of particle physics. LEP stopped in November 2000, but the analysis of data is still going on, with the possibility of discovering new physics phenomena.

LEP accelerates electrons and positrons, in opposite directions in a vacuum pipe inside a retaining ring of magnets, before inducing them to collide head-on. In their annihilation, the energy released in a small volume is comparable to that which existed in the Universe a fraction

of a second after its creation in the Big Bang, so there is a synthesis between the very large (cosmology) and the very small (particle physics).

To achieve the high energy needed, the particles are accelerated turn after turn in the circular accelerator. Special acceleration fields increase the energies of the particles for each turn. Different types of magnets force the particles to move in well-defined orbits. Four steps of acceleration increase the energies of the particles with up to 400 MeV per turn, to a top energy of about 100 GeV. Four bunches of electrons and positrons can circulate inside the ring for hours, with a speed very close to the speed of light.

The LEP collider's initial energy was chosen to be around 91 GeV, so that in these collisions a Z^0 particle would be produced. The Z^0 and its charged partner the W^+ were both discovered at CERN in 1983. The Standard Model has been critically tested by studying the creation and decay of the Z^0. The Z^0 is very short-lived, so its presence has to be inferred from its disintegration fragments, which may vary from two to nearly a hundred.

Since the end of 1995, LEP moved on from the Z^0 and entered its second phase. Its energy was doubled to allow the study of the production of the Z^0Z^0 pairs and of W^+W^- pairs thus opening a new domain of investigations and the Standard Model tests, the search for new particles, in particular the Higgs boson and/or supersymmetric particles, in a new energy domain. LEP attained the world energy record of about 210 GeV , enough to create more than 220 protons.

The LEP accelerator was in operation between 1989 and 2000. Then the whole machine was dismantled to make room for a new accelerator in the same tunnel. The name of the new accelerator is Large Hadron Collider, LHC.

LEP had four intersection regions, each surrounded by a particle detector to measure the properties of the secondary particles created from the electron-positron collision. Each of the detectors (DELPHI, ALEPH, L3 and OPAL) has been optimised differently to study various physics aspects. During almost 12 years of running, the experiments have allowed extremely precise tests of the Standard Model, and more results will come from the ongoing data analysis.

The DELPHI detector was one of the four big detectors in the LEP accelerator. DELPHI was constructed and installed in 1989, at the same time as LEP itself. In December 2000 the data taking with DELPHI stopped to leave room for the construction of the LHC accelerator in the LEP tunnel.

DELPHI is an advanced detector. As well as having high precision and 'granularity', it has the specific ability, using the Ring Imaging Cherenkov technique, to differentiate between all the various secondary charged particles. It also has an advanced silicon detector providing very precise tracking, principally in order to detect very short lived particles by extrapolating the tracks back towards the interaction point. Design and construction of the DELPHI detector took 7 years; data was taken every year for 12 years. The latest collaboration consisted of about 550 physicists from 56 participating universities and institutes in 22 countries.

The structure of the DELPHI detector is displayed in figure 1.8. The detector consisted of three parts; a cylinder shaped central part and two endcaps. The length and diameter was about 10 meters and the total weight was 3500 tons. DELPHI's most important components were about 20 subdetectors of the different types discussed in the previous pages. A large superconducting magnet, crucial for the detector, was located between the electromagnetic and hadronic calorimeters. The magnetic field from this magnet deflects charged particles so that their charge and momenta can be measured.

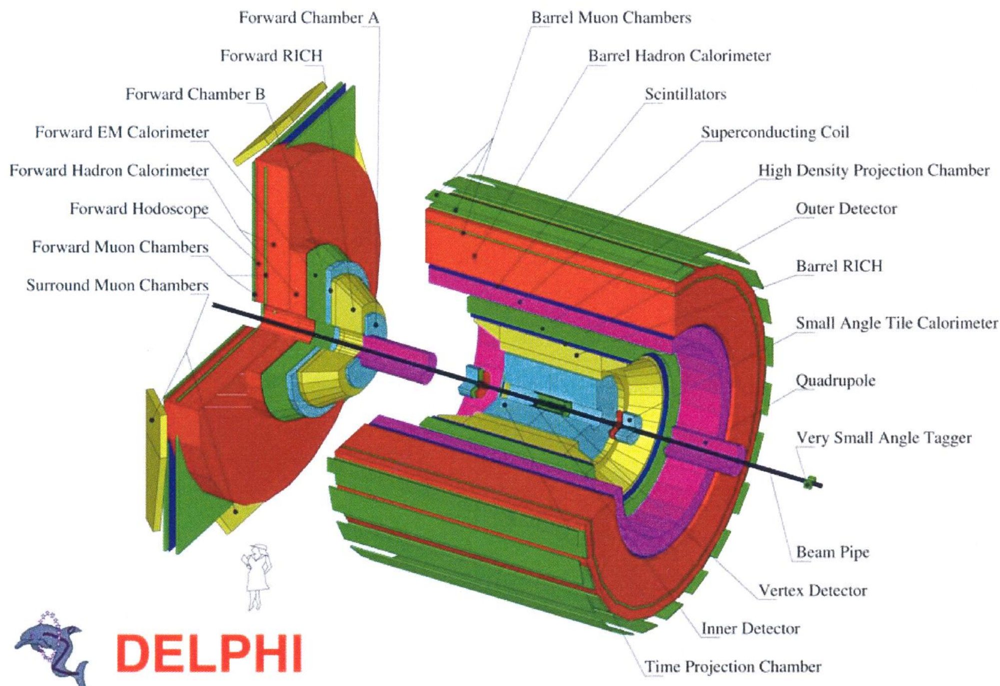

Figure 1.8. An illustration of the DELPHI detector. One of the endcaps is visible to the left, and to the right is the cylindrical centre part (the other endcap is not shown). The different subdetectors are coloured to make it easier to identify their locations (http://hands-on-cern.physto.se/hoc_v21en/index.html).

1.3.2 LHC

The LEP accelerator has now been stopped and removed from the underground tunnel to make room for the Large Hadron Collider. In the LHC very high energy protons will collide against protons, and heavy ions (like the nuclei of lead) will be smashed against heavy ions. This will allow scientists to penetrate still further into the structure of matter and recreate the conditions prevailing in the Universe just a few picoseconds after the Big Bang (10^{-12} s).

Due to switch on in 2007, the LHC will ultimately collide beams of protons at an energy of 14 TeV . Beams of lead nuclei will be smashed together with a collision energy of 1150 TeV.

The LHC has some fundamental questions to answer. When the Universe was young and much hotter than today, perhaps all forces behaved as one. Particle physicists hope to find a single theoretical framework to prove this, and have already had some success. Two forces, the electromagnetic force and the weak force were unified into a single theory in the 1970s. This theory was experimentally verified in a Nobel prize winning experiment at CERN a few years later. The weakest and the strongest forces, gravity and the strong force, however, remain apart.

A very popular idea suggested by the unification of the forces is called supersymmetry, or SUSY for short. SUSY predicts that for each known particle there is a supersymmetric partner. If SUSY is right, then supersymmetric particles should be found at the LHC.

The LHC will help us also to solve the riddle of antimatter. It was once thought that antimatter was a perfect reflection of matter - that if you replaced matter with antimatter and looked at the result in a mirror, you would not be able to tell the difference. We now know that the reflection is imperfect, and this could have led to the matter-antimatter imbalance. The LHC will be a very good antimatter-mirror, allowing us to put the Standard Model through one of its most gruelling tests yet.

These are just a few of the questions the LHC should answer, but history has shown that the greatest advances in science are often unexpected. Although we have a good idea of what we hope to find at the LHC, nature may well have surprises in store. One thing is certain, the LHC will change our view of the Universe.

The new LHC accelerator will have two big detectors of the same kind as DELPHI in LEP. These two are named ATLAS and CMS. In addition three other experiments, LHCb, ALICE and TOTEM, have been approved for the LHC.

The construction of the ATLAS detector is similar to that of the DELPHI detector, but ATLAS is much bigger. When it has been completely assembled ATLAS will be about 22 meters high and 44 meters long.

The CMS collaboration decided to use an all-silicon solution for the tracker. In total the CMS tracker implements 25 000 silicon strip sensors covering an area of 210 m^2. Connected to 75 000 APV chips, one has to control 9 600 000 electronic readout channels, needing about 26 million microbonds. This large detector system will be realized, applying industrialized methods in production and quality assurance. A cross section of the CMS tracker is displayed in figure 1.9.

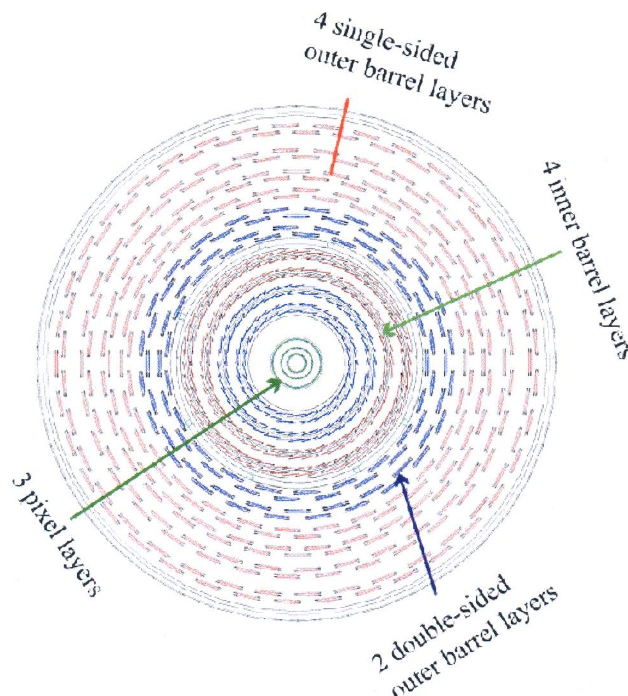

Figure 1.9. The CMS tracker. The diameter of the barrel is 2.4 m and the length 5.4 m (http://cmsinfo.cern.ch/Welcome.html/CMSdetectorInfo/TrackingDetectors/page3.html).

1.4 Luminosity requirements

Luminosity in a particle collider such as LEP indicates how intense the beams are before they collide, and it is usually given as a number per square centimetre per second. Adding up (integrating) the luminosity over the number of seconds for the whole run, gives the total luminosity as a number per square centimetre, or per picobarn (pb^{-1}), where a picobarn is 10^{-36} cm^2. Particle rate is of course the luminosity multiplied by the cross section.

In experimental particle physics, achieving high luminosity is as important as achieving high energy. Not all collisions produce the same effects, and the types of collisions that we are trying to study are extremely rare. Therefore we need huge numbers of ordinary collisions (hence lots of luminosity) to see just a few of the interesting ones. With the anticipated luminosity of the LHC, we expect as many as one billion total collisions per second, of which at most 10 to 100 per second might be of potential scientific interest. In fact, some of the most interesting types of collisions are so rare that they may occur only once every few hours or every few days. If the luminosity were one tenth as much, we might see one only every few weeks, and that would make its discovery vastly more difficult.

Figure 1.10 shows the achieved peak luminosities of the LEP collider. The continuous trend is towards higher and higher luminosities. The particle detectors have to tolerate the integrated luminosity during their operation time. This is shown in figure 1.11 for the total time of the LEP operation.

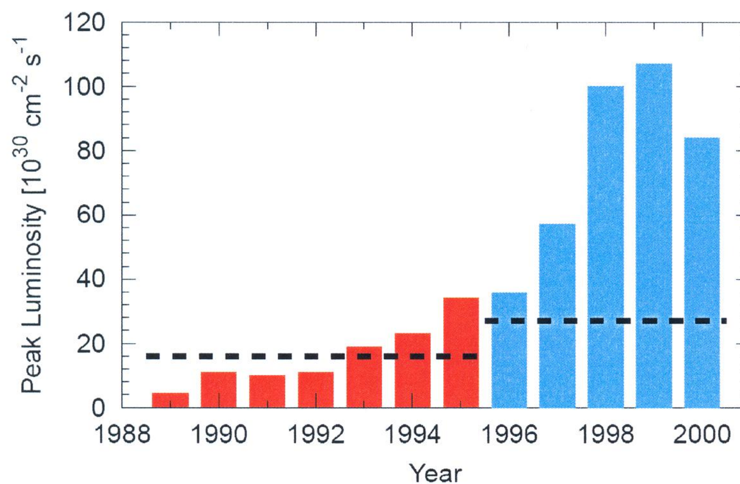

Figure 1.10. Peak luminosity for each year of LEP operation. The dashed lines indicate the design luminosities for LEP1 (red bars) and LEP2 (blue bars) (Assman).

The luminosity of the LHC will be 10^{34} $cm^{-2}s^{-1}$ in 10 years of operation, which is about 100 times higher than the maximum in LEP. For example the pixel detectors of the CMS tracker will see a neutron equivalent fluence of 10^{15} n/cm^2 and the strip detectors a fluence of 10^{14} n/cm^2 .

The LHC upgrade, Super-LHC or S-LHC, after year 2010 will raise the fluence up to 10^{35} $cm^{-2}s^{-1}$ and the integrated fluence seen by the detectors up to 10^{16} cm^{-2} after five years.

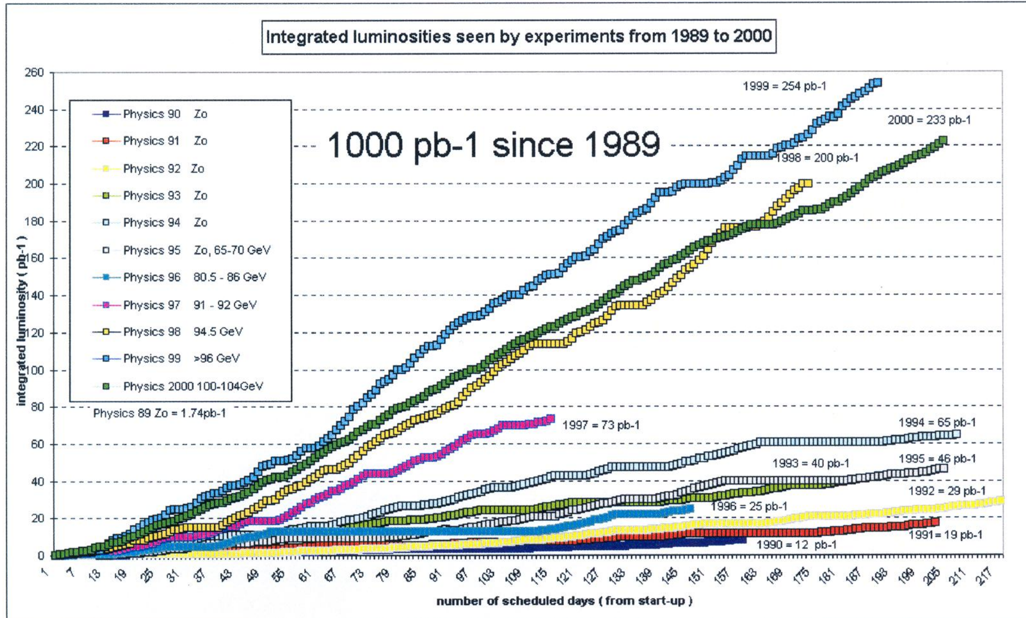

Figure 1.11. Integrated luminosities of the LEP collider. pb is 10^{-36} cm^2 (http://greybook.cern.ch).

Table 1.6 displays the anticipated radiation environment for the Super LHC. The table lists the hadron fluences and the radiation doses in different radial layers of the CMS tracker for an integrated luminosity of 2500 fb^{-1} (Bruzzi, Fretwurst et al.).

Table 1.6. The anticipated radiation environment for the Super-LHC.

Radius [cm]	Fluence of fast hadrons [cm^{-2}]	Dose [kGy]
4	$1.6 \cdot 10^{16}$	4200
11	$2.3 \cdot 10^{15}$	940
22	$8.0 \cdot 10^{14}$	350
75	$1.5 \cdot 10^{14}$	35
115	$1.0 \cdot 10^{14}$	9.3

1 Gy (Gray) tells that 1 J of ionizing energy is absorbed in 1 kg. Those still more familiar with Mrads should divide the doses given in kGy by 10. To compare, during LEP1 operation, we were talking about a radiation tolerance of 1 Mrad for silicon strip detectors.

1.5 Summary of publications

Publication I briefly describes our first tests to produce strip detectors on a 100 mm wafer. A large strip detector with an active area of 32 x 58 mm^2 was designed, manufactured and tested. I personally designed the process and tested several process parameters to find the best processing conditions. Backside gettering and an anneal at 900 °C was found to produce the lowest leakage current. Oxidation tests were performed in several temperatures in dry and wet atmosphere. <100> wafers were better and dry oxidation produced fewest surface states. With <111> wafers the best oxidation temperature was 1050 °C regardless of the oxidation atmosphere. When measuring the complete detector attached to the readout electronics, a signal to noise ratio 14 was measured with a ^{90}Sr source.

Publication II presents a capacitively coupled double-sided strip detector with integrated polysilicon bias resistors. I personally designed the rather complicated two-sided process and the details of the layout, like comprehensive test structures and a novel field plate structure around the ends of n-strips. I also made several test processes to develop polysilicon resistors with a constant and stabile resistance. A leakage current of 40 nA/cm^2 at 50 V and a signal to noise ratio 35 were achieved.

Publication III describes the measurement results on both sides of a double-sided strip detector. The paper describes the principle of the cross-electrode readout on the n-side and the isolation of the ends of n-strips with polysilicon rings. Static measurements yielded the depletion voltage and the leakage current. The surface state density was measured to be $5.4 \cdot 10^{11}$ cm^{-2}. The polysilicon resistor accuracy was better than ±10 %. The same signal height was achieved on both p-side and n-side when using a ^{90}Sr source. The signal to noise ratio was 21 on the p-side and 18 on the n-side.

Publication IV describes the method to measure voltages and electric fields in a biased silicon radiation detector using a scanning electron microscope. The detector was split for measuring the electric potential on the cross section of the detector using the commonly known voltage-contrast effect. The contrast was read into a PC with an ADC card and a home-made c++ software and converted to voltage and accordingly to electric field and charge density with simple mathematical formulas. The results were compared to 2D electrical simulations. I personally developed this measurement system including the physical setup and the software and made all the measurements starting from initial trials to final results. I also made the 2D simulations with Silvaco Atlas software.

In *Publication V* the voltage measurement system with a scanning electron microscope was applied to 10 MeV proton irradiated float zone silicon radiation detectors. The results were compared with those acquired with other methods. The same semiconductor type inversion of n-bulk and a double-junction behavior were observed in this study but with a better accuracy.

Publication VI describes the patterning of silicon strip detectors with a 5:1 reduction stepper. This method was originally considered to be impossible for many reasons, but was however successfully used in the fabrication of double-sided silicon strip detectors. The demand to use a stepper instead of a contact aligner came from process technicians. I developed the method and finally wrote the publication describing exactly how the job was done.

Chapter 2

Semiconductor particle detectors

2.1 Basic analysis of a pn junction

The operation of a semiconductor particle detector is based on a pn junction. A pn junction is formed when a single crystal of semiconductor is doped with acceptors on one side and with donors on the other side. In figure 2.1 the positive donor ions are represented by plus signs and free electrons by small filled circles. The negative acceptor ions are depicted by minus signs and the holes by small unfilled circles. The structure is originally electrically neutral, ie. the number of holes is the same as the number of acceptor ions and the number of free electrons is the same as the number of donor ions.

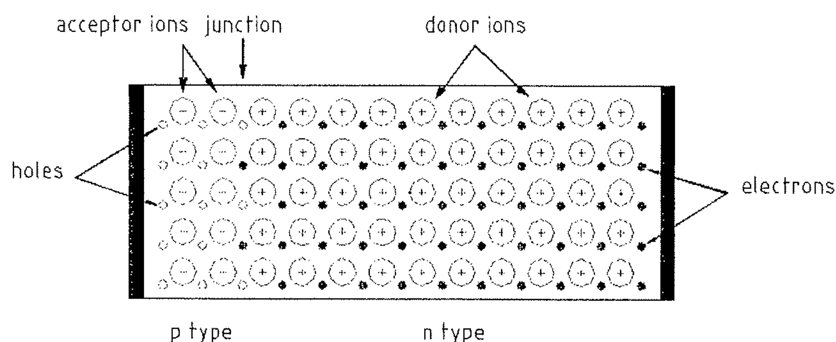

Figure 2.1. A schematic representation of a pn junction before reaching equilibrium conditions.

Initially a concentration gradient of electrons and holes exists across the junction, causing holes to diffuse to the right and electrons to the left across the junction. An electron and a hole which meet at the junction will recombine and thus both disappear. This will lead the acceptors and the donors in the neighborhood of the junction to loose their mobile electrons and holes. The electrically unneutralized ions in the neighborhood of the junction result in a charge density ρ. Since this region is depleted from mobile charges, it is called the depletion region.

Because of the uncovered fixed donor and acceptor ions, a charge distribution is formed over the depletion region. The depletion region is hence also called the space-charge region. Because the n-side of the depletion region is positive and the p-side negative, an electric field exists across the depletion region. This field points from right to left, from the fixed positive charges towards the fixed negative charges, and it resists the motion of both electrons and

holes. Finally the electric field strength will be such that no more electrons and holes can diffuse across the pn junction. Then the pn junction has reached its equilibrium condition as displayed in figure 2.2.

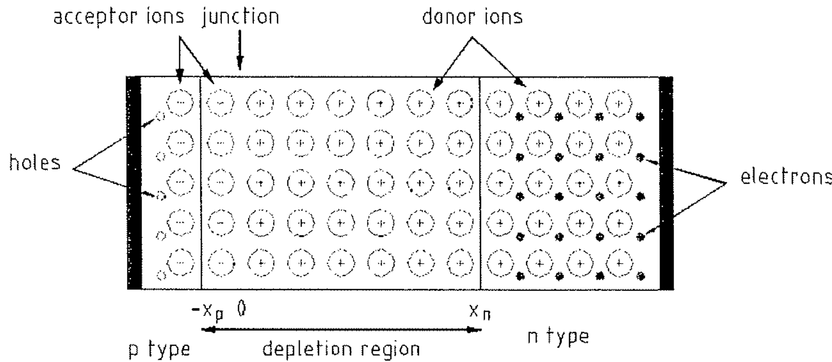

Figure 2.2. A schematic representation of a pn junction after reaching equilibrium conditions.

Because of the electric field, a potential difference or a voltage develops across the depletion region without any external voltage connected to the structure. This is known as the built-in potential V_0. The potential V at any point in the depletion region can then be calculated with the Poisson's equation

$$\frac{d^2V}{dx^2} = -\frac{\rho}{\varepsilon} \quad , \tag{2-1}$$

where x is the horizontal coordinate in figure 2.2, ρ is the charge density and ε the dielectric constant of the semiconductor. The length (in the x direction) of the depletion region can be calculated using the Poisson's equation together with the value of the built-in potential.

The built-in potential makes the pn junction reverse biased. In particle detector applications an external reverse bias is added to this built-in potential causing the depletion region to become longer. To get a good qualitative insight about the behavior of a pn junction, the electric field and the potential of a simple abrupt pn junction were calculated analytically using a spread sheet software.

The length of the structure (the thickness of the pn diode) was chosen to be 100 μm. The junction depth x_J was 10 μm. The doping concentration on the n-side bulk material, i.e. the donor concentration N_D, was near the bulk doping of a standard silicon radiation detector, 10^{13} cm^{-3}. The p-side doping, i.e. the acceptor concentration N_A, was selected to be an adequately low value, so that the spreading of the depletion region on both sides of the pn junction could be seen clearly, $N_A = 2 \cdot 10^{14}$ cm^{-3}. To get a good ohmic contact to the silicon, a higher doping concentration must be used at both end surfaces. In the calculation this concentration was 10^{18} cm^{-3} on the p-side and $2 \cdot 10^{14}$ cm^{-3} on the n-side. On the n-side the used value is still much lower than the one needed in a practical device. The p-side concentration values are negative in the calculation, because acceptor ions are negative. This structure is shown in figure 2.3. The concentration values are displayed in a signed logarithmic scale, i.e. the logarithm taken from the concentration value is multiplied by its sign.

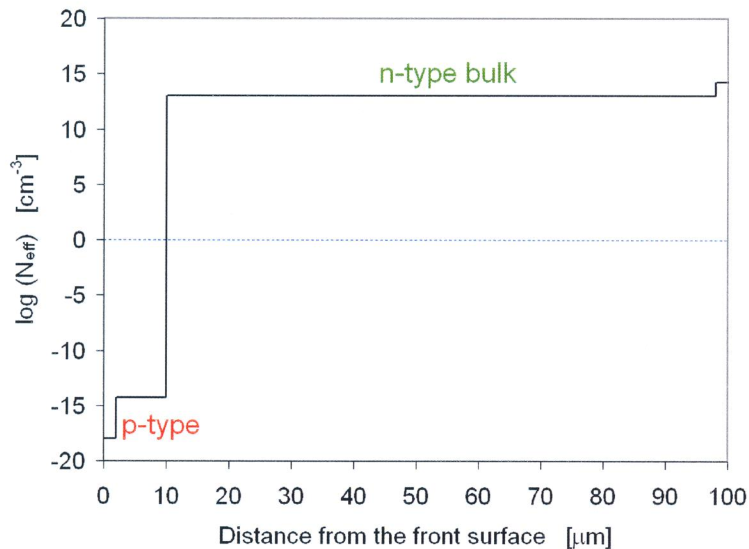

Figure 2.3. The doping profile of the calculated pn-diode in a signed logarithmic scale.

The built-in potential must be calculated first. Its value can be found by equating the force caused by diffusion with the force caused by the electric field. In the abrupt pn junction it is

$$V_0 = V_T \ln \frac{N_A N_D}{n_i^2} \quad , \qquad (2\text{-}2)$$

where n_i is the intrinsic carrier concentration in the semiconductor material, i.e. the electron and hole concentration in an intrinsic material at the examined temperature, and V_T is the voltage equivalent of temperature

$$V_T = \frac{k\,T}{q} \quad , \qquad (2\text{-}3)$$

where k is the Boltzmann constant, T the absolute temperature and q the elementary charge (Millman & Grabel). Performing this calculation for our structure manufactured on silicon substrate, with $T = 300$ K and $n_i = 1.45 \cdot 10^{10}$ cm^{-3}, V_0 is found to be 0.415 V .

Poisson's equation can be used to calculate the length of the depletion region. In a numerical analysis this could be done iteratively. In an abrupt junction the length of the depletion region can also be found with an equation (Muller & Kamins)

$$x_d = \sqrt{\frac{2\,\varepsilon}{q}\left(\frac{1}{N_A} + \frac{1}{N_D}\right)(V_0 - V_a)} \quad , \qquad (2\text{-}4)$$

where V_a is the applied voltage across the device in standard direction, i.e. from the p-side to the n-side. The positive space-charge (on the n-side) and the negative space-charge (at the p-side) must balance each other. Thus we can calculate the length of the depletion region on the p-side, x_p, and at n-side, x_n:

$$x_p N_A = x_n N_D \tag{2-5}$$

Remembering that the total length of the depletion region is

$$x_d = x_p + x_n \quad , \tag{2-6}$$

the lengths at both sides of the junction are

$$x_p = \frac{N_D}{(N_A + N_D)} x_d \tag{2-7}$$

$$x_n = \frac{N_A}{(N_A + N_D)} x_d \tag{2-8}$$

Setting the density of charges in the depletion region the same as the doping density and zero outside the depletion region, we get the graph of density of charges, which is displayed at eight bias voltages in figure 2.4 in a signed logarithmic scale. The spreading of the depletion layer can be seen in the figure, although this presentation is not the most lucid one.

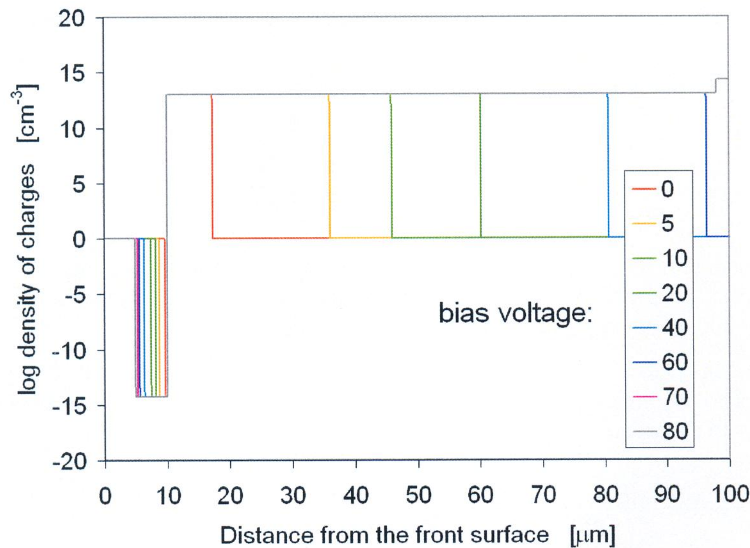

Figure 2.4. The density of charges in a signed logarithmic scale.

After using the Poisson's equation (2-1) we get the electric field

$$E = -dV/dx = \int_0^x \frac{\rho}{\varepsilon} \, dx \qquad (2\text{-}9)$$

The charge density ρ is calculated by multiplying the density of charges of figure 2.4 by the elementary charge q. The integration should formally be started at the edge of the depletion region at the p-side, but because the charge density is zero outside the depletion region, this makes no difference.

If all the calculations are correct, the electric field should start from zero at the p-edge of the depletion region, reach a negative maximum peak at the pn junction and go exactly to zero at the n-edge of the depletion region. This result is displayed in figure 2.5 for eight bias voltages.

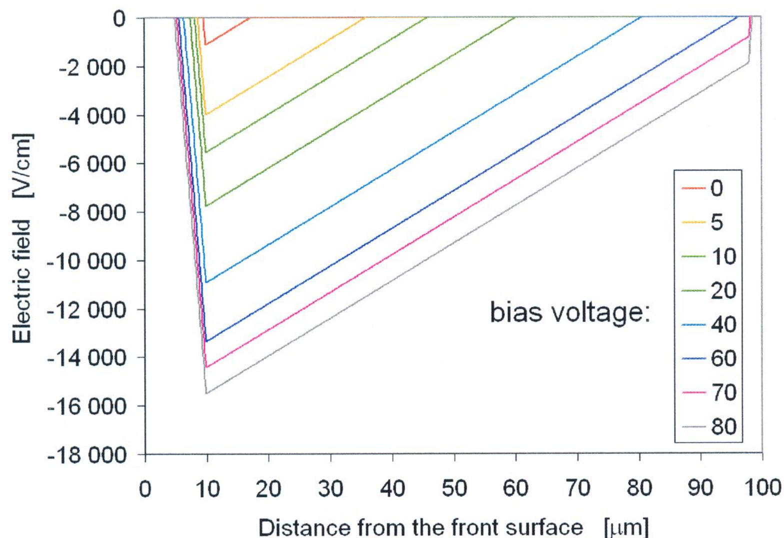

Figure 2.5. The electric field in the examined abrupt pn junction structure.
(For non-color prints, the curves are in the same order from top to bottom as in the legend.)

The electric potential is found by integrating the electric field,

$$V = -\int_0^x E \, dx \qquad (2\text{-}10)$$

The result is shown in figure 2.6 for eight bias voltages. The final inspection for the calculation is that the overall potential after this calculus should be the bias voltage plus the built-in potential V_0.

The capacitance of the pn junction is the change of the charge Q associated with the junction divided by the change of the voltage over the junction,

$$C = \frac{dQ}{dV} \tag{2-11}$$

The charge is calculated by integrating the charge density up to the junction,

$$Q = \int_0^{x_j} \rho \, dx \tag{2-12}$$

The results of the one dimensional calculation yields the capacitance per the area of the junction. It is displayed in figure 2.7.

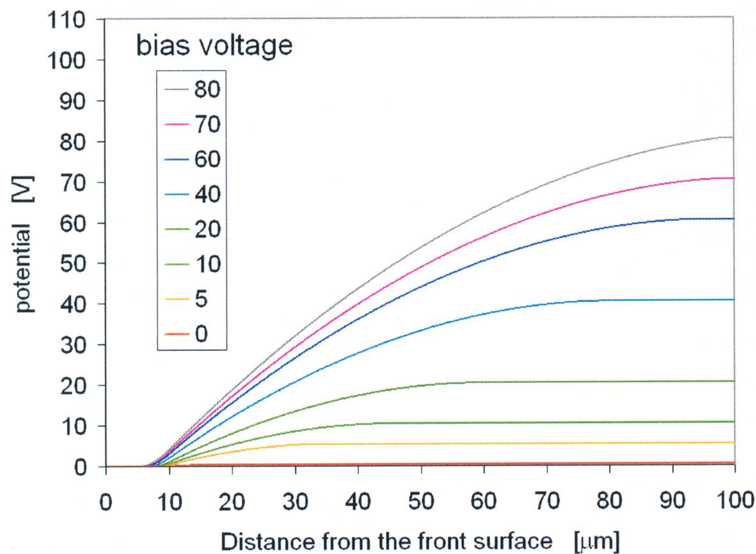

Figure 2.6. The potential distribution in the examined abrupt pn junction structure.
(For non-color prints, the curves are in the same order from bottom to top as in the legend.)

Capacitance-voltage, or CV, measurements are often done to pn junctions to find the length of the depletion layer and the bulk doping. In a special case of radiation detectors, people are interested on the full depletion voltage of the detector, i.e. the reverse bias voltage needed to extend the depletion layer across the whole detector thickness. This is difficult to deduce from a graph like the one in figure 2.7. Instead, the inverse of squared capacitance, $1/C^2$, is plotted as a function of applied voltage. This kind of graph is displayed in figure 2.8. The voltage for full depletion is clearly seen at the kink of the graph, it is 60 V. Comparing this figure with the previous figures, especially with figure 2.5 showing the electric field, reveals that not all the detector thickness is depleted, because the depletion almost stops at the higher donor concentration at the back side and because a layer at the front surface also remains undepleted.

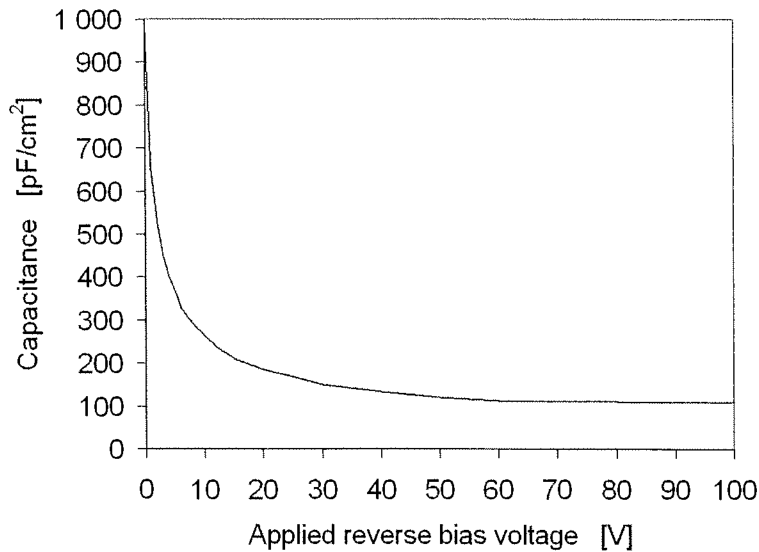

Figure 2.7. The capacitance per square centimeter of the area of the junction.

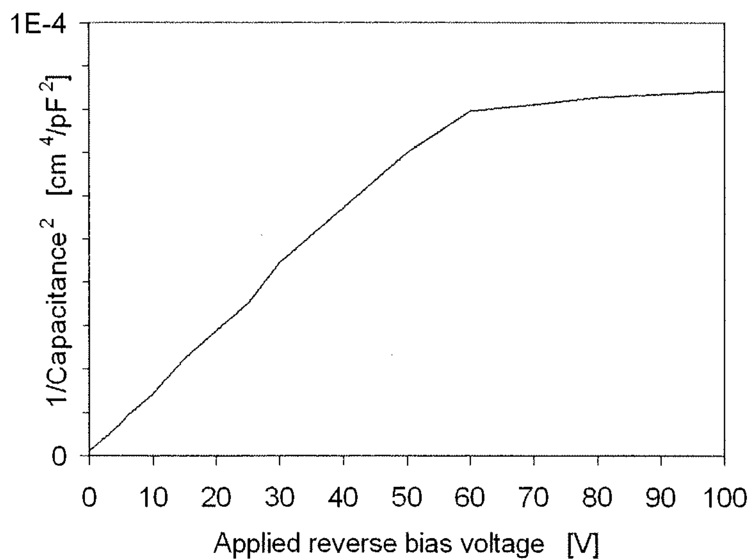

Figure 2.8. Plot of $1/C^2$ as a function of applied bias voltage. Both scales are linear.

Finally, a note on the accuracy used in these spread sheet calculations. The x step was 0.1 μm. At the edges of the depletion layer this was a too large step. The accuracy was improved by placing a suitable fraction of the doping concentration at the first x outside the depletion region. The capacitance was calculated only at voltages 0, 1, 2, 3, 4, 5, 6, 8, 10, 12, 15, 20. 25, 30, 40, 50, 60, 70, 80, 100 and 101 V. These same steps were used in the calculation of dQ/dV in equation 2-11.

2.2 Operation of a silicon radiation detector

Figure 2.9 shows a schematic cross-section of the most simple radiation detector, a p-i-n diode. The bulk of the diode is high-resistivity n-type material that is fully depleted by a negative potential applied to the p-contact on the upper surface of the detector. The respective positive potential is applied to the n-type back-contact. The incident radiation, either photons (gamma, x-rays) or charged particles (alpha, beta, ions, nuclear particles), produces tracks of electron-hole pairs. To be exact, the photon gives all of its energy in one photoelectric action at the depth depending very randomly on the energy of the radiation quantum. A charged particle, on the contrary, gives its energy to the silicon lattice little by little in a well behaving manner creating electron-hole pairs along its track, the rate of energy transfer depending mainly on the incident energy and mass of the particle. For an in-depth view, see Knoll's book (Knoll). In the presence of an electric field as shown in the figure, the electron-hole pairs separate and rapidly drift to the contacts, electrons to the positive (n-type) contact and holes to the negative (p-type) contact.

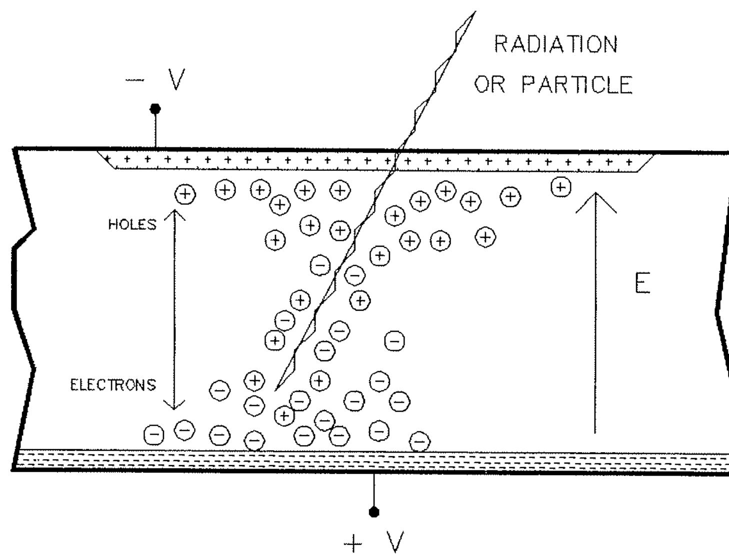

Figure 2.9. Schematic diagram of the operation of a p-i-n diode radiation detector.

The charge Q_S collected at the contacts is proportional to the energy E lost by the incident radiation in the sensitive volume of the detector:

$$Q_S = \frac{E}{E_p} \cdot q \quad , \tag{2-13}$$

where E_p is the energy required to generate one electron-hole pair; $E_{pSi} = 3.64$ eV and $E_{pGe} = 2.98$ eV. Further, the rms statistical fluctuation in Q_S is

$$\Delta Q_S = \sqrt{F \cdot E / E_p}\ q \qquad , \qquad (2\text{-}14)$$

where the Fano factor F describes the deviation from normal Poisson statistics. The value currently accepted is $F \sim 0.1$ for both silicon and germanium. Values much greater than this are indicative of signal charge collection problems (i.e. trapping centers) in the detector material. The theoretical minimum of the Fano factor is thought to be as small as 0.04 . With semiconductor detectors a value 0.06 has been measured.

The leakage current associated with a reverse biased semiconductor junction has three components, diffusion (or thermionic emission in the case of surface barriers), thermal generation and surface leakage. For silicon detectors operated at room temperature (300 K) and lower, the diffusion component is so small that it can be ignored (Grove). The surface leakage current is strongly fabrication process dependent and is discussed later. The main contribution to the leakage current in a good silicon detector should come from thermal generation in the depleted silicon volume. The value of it is

$$I_g = \frac{n_i}{2\tau} \cdot q\,\Lambda \qquad , \qquad (2\text{-}15)$$

where n_i is the intrinsic carrier concentration, τ the generation lifetime and Λ the depleted silicon volume. To minimize the leakage current, the generation lifetime must be maximized.

The capacitance and the leakage current of a semiconductor detector are determined by the volume of the depletion layer of the reverse biased pn junction. The length of the depletion layer in a one-sided abrupt junction is given by a little simpler equation than equation 2-4:

$$x_d = \sqrt{\frac{2\varepsilon}{q} \cdot \frac{V_0 - V_a}{N}} \qquad , \qquad (2\text{-}16)$$

where ε is the permittivity of the semiconductor, V_0 the built in potential of the junction, V_a the applied voltage and N the doping concentration of the weakly doped side of the junction (Muller & Kamins).

In a high resistivity n-type silicon the resistivity ρ and the doping density N are related by the equation

$$\rho = \frac{1}{\sigma} = \frac{1}{q\,N\,\mu_n} \qquad , \qquad (2\text{-}17)$$

where σ is the conductivity of the material and μ_n the mobility of electrons. Using a value 1350 cm^2/Vs for the mobility at room temperature, we get

$$\rho = \frac{4.62 \cdot 10^{19}\ \Omega / m^2}{N} \qquad , \qquad (2\text{-}18)$$

which yields a simple approximate relationship:

$$\rho = \frac{500}{N} \quad , \qquad (2\text{-}19)$$

when the resistivity ρ is expressed in kΩcm and N in $10^{10}\,\text{cm}^{-3}$.

After calculating out the constants in equation 2-16, omitting the usually insignificant built-in potential V_0 , and using the relationship 2-18, we get

$$x_d = \sqrt{2.80 \cdot 10^{-11}\ \text{m}^2/\text{V}\Omega\text{m} \cdot |V_a| \cdot \rho} \quad , \qquad (2\text{-}20)$$

which gets a simple form when ρ is expressed in kΩcm , V_a in volts and x_d in microns:

$$x_d = \sqrt{280 \cdot |V_a| \cdot \rho} \quad . \qquad (2\text{-}21)$$

The generation current of the detector is thus

$$I_g = \frac{n_i}{2\tau} \cdot q\,A\,x_d \quad , \qquad (2\text{-}22)$$

where A is the depleted area of the detector, and the capacitance is

$$C = \frac{\varepsilon A}{x_d} \quad . \qquad (2\text{-}23)$$

The resistivity of the detector material has no direct influence on the detector characteristics. The detector material needs to have a high resistivity only because it is then easier to deplete a deep volume with a reasonable voltage, and because a shallow pn junction then has a higher breakdown voltage. The first of these things also helps the situation with the other.

2.3 The microstrip detector

The silicon microstrip detector was developed for nuclear charged particle tracking applications to replace in many places the old wire-chamber detectors consisting of a large number of long parallel biased metal wires in a thin gas-filled chamber, where a charged particle produced electron-ion pairs, which were detected as a charge pulse in one wire (plus the neighbouring wires) that indicated the position of the track of the particle. The position resolution in a wire-chamber is at best 50 to 100 µm , in a microstrip detector a position resolution better than 5 µm is achieved.

Figure 2.10 shows the basic structure of a single-sided dc-coupled position sensitive silicon microstrip detector. It consists of a thin (~ 300 μm) n-type silicon wafer having a continuous n+n junction on one side of the wafer and a strip pattern of p+n junctions on the opposite side. Typical number of channels or p-strips is n times 128 , where n is an integer between 1 and 10 . The length of the strips ranges from 1 cm to 8 cm . A reverse bias voltage is applied across the wafer to deplete the detector and to provide the collection field. A fast charged particle passing through the detector produces electron-hole pairs which drift towards the electrodes under the influence of the electric field. The motion of the charge carriers induces a signal in an amplifier connected between the n+ and the p+ contacts.

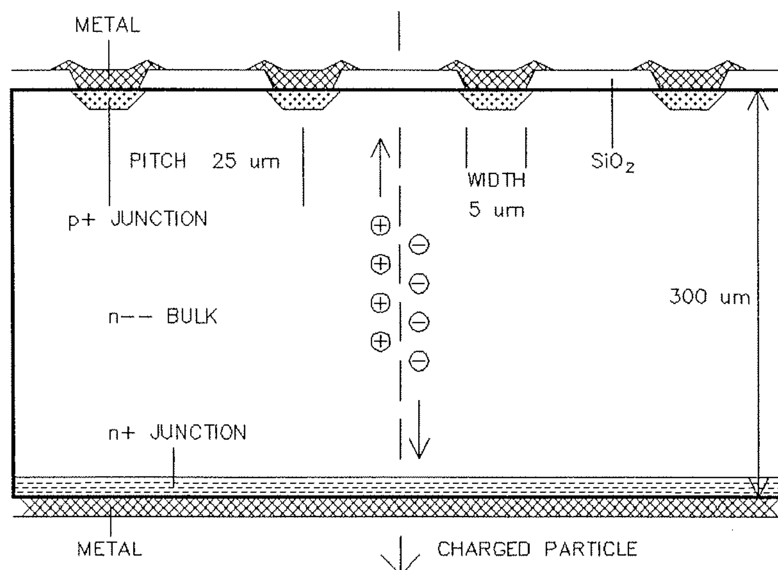

Figure 2.10. The structure of a standard parallel microstrip detector.

Position sensing in this kind of configuration is done by the granularity of p+ contacts. The method, in principle, requires as many amplifiers as the number of individual strips, ie. one amplifier must be connected to each individual p-strip. Using capacitive or resistive charge division readout, the number of amplifiers can be reduced by up to a factor of 10. A certain price is paid in the complexity of the readout channels, and the doubletrack resolution is sacrificed. The charge distribution between neighbouring strips can be utilized to reduce the number of amplifiers by a factor of 2 or 3, by not connecting an amplifier to every strip. Some accuracy is lost, but still the position resolution is much better than the strip pitch. In a common configuration, where an amplifier is connected to every second strip, a position resolution better than 5 μm is achieved with a strip pitch 25 μm and width 5 μm .

Using dc-coupled detectors together with LSI readout chips brings with it the inconvenience that the leakage current of each strip is fed into the preamplifier. It is not possible to couple capacitively to the preamplifier as in the case of conventional electronics because one needs several tens of picofarad for the coupling capacitance in order to avoid capacitive signal losses to the back plane. Leakage currents of individual strips often vary by a factor of up to 1000 across one large detector. With chip readout this phenomenon introduces considerable base line differences between the channels of one chip and requires an otherwise unnecessarily large dynamic range of the ADCs. Therefore, the detector should have built-in coupling capacitor in connection with every readout strip (Caccia et al.).

In the case of capacitive coupling in the detector, the bias voltage must be fed to the strips through individual resistors to allow voltage variation in each strip where a particle generates a signal. This has been accomplished by integrating polysilicon resistors in the detector between a common bias line and each individual strip.

The detector shown in figure 2.10 has a position sensitivity only in one dimension. To add a second dimension, there must also exist strips going perpendicular to the p-strips. In the most common design nowadays used, these perpendicular strips are processed on the back surface (n-side) of the detector. The strips on the p-side are p-type, the strips on the n-side are n-type. Also each n-strip is connected to an individual amplifier, and in an ac-coupled design must have an integrated coupling capacitor and bias resistor (Publication II). The resultant structure is shown in figure 2.11 and its circuit diagram in figure 2.12.

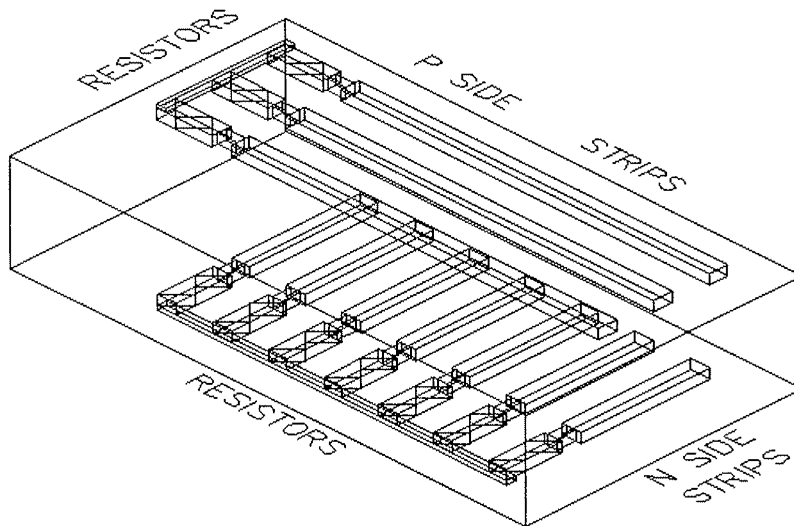

Figure 2.11. The structure of a double-sided ac-coupled strip-detector with integrated readout capacitances and bias resistors (for clarity, the readout capacitances have not been drawn, and only 3 p-strips and 7 n-strips are drawn).

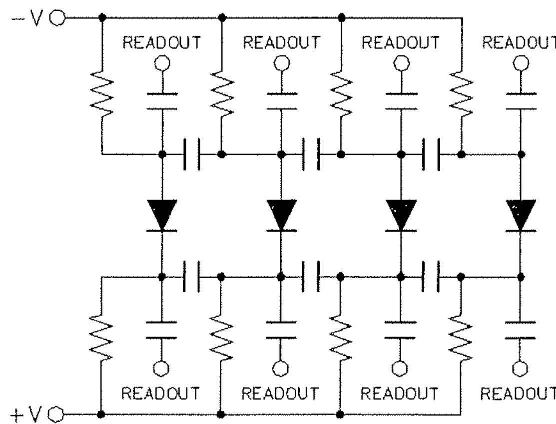

Figure 2.12. The electrical schematic of the structure shown in figure 2.11.
The interstrip capacitances are also shown.

The double-sided structure is in practice very effective and gives good signal to noise ratios on both sides, because both electrons and holes are included in the signals. However, the fabrication of a large area double-sided structure is extremely awkward. If less noisy preamplifiers would be available, the two-dimensional structure could as well be fabricated on one side of the wafer. Both strips could be on the same side of the wafer, or the pattern could also consist of separate pads. Both of these single-sided structures suffer from reduced signal to noise ratio and reduced position resolution because the same quantity of charge of only one carrier type has to be used for both dimensions.

Figure 2.13. shows the p-side layout of a corner of an ac-coupled double-sided strip detector. The meander patterns in the left are $3\ \text{M}\Omega$ polysilicon bias resistors. Every second of them is connected to the left end of the corresponding p-strip implantation with a short metallization, every second to the right end. The charge distribution is utilized so that only every second strip is read out although every strip is biased. The bonding pads are shown on the readout-strips as $50\ \mu\text{m} \times 120\ \mu\text{m}$ widenings in the metallization on the strips. On the intermediate strips there is no metallization. The readout-strip pitch is $50\ \mu\text{m}$ and the linewidth of the implantation is $5\ \mu\text{m}$. The outermost metallization surrounds the whole detector and connects all outer ends of the bias resistors to a common bias line. The other wide ring, shown in the figure going under the metallizations that connect bias resistors to strip implantations, is a guard ring surrounding the active area of the detector. This is a p-diffusion on the p-side and an n-diffusion on the n-side, and is contacted to the same potential as the strip-diffusions on the same side. It is used to collect the charge generated outside the active area.

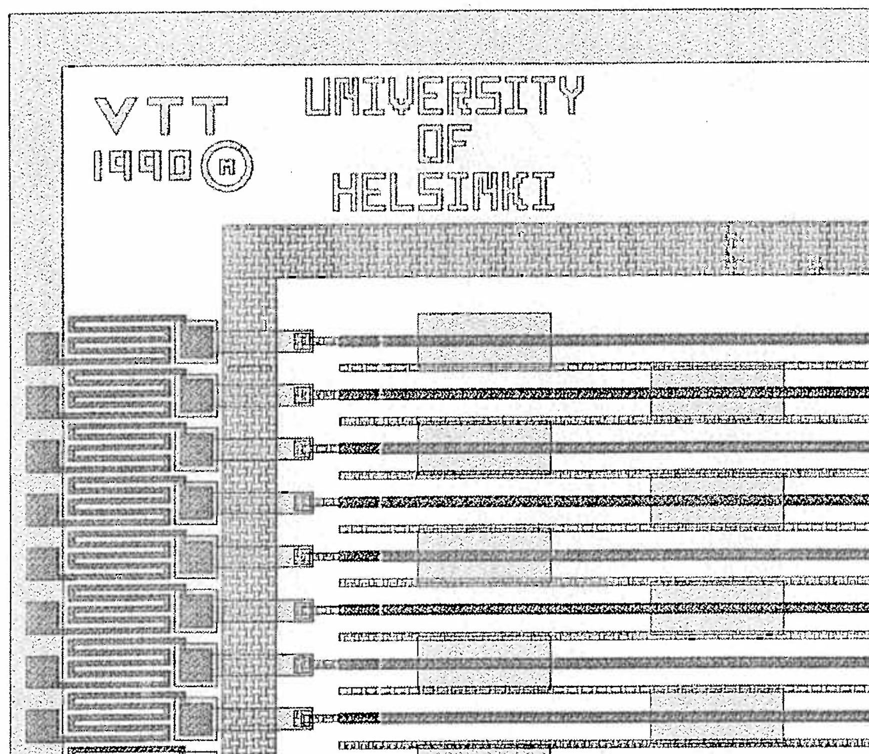

Figure 2.13. The layout of the p-side of a double-sided ac-coupled strip-detector.

The layout of the same corner of the n-side is shown in figure 2.14. The vertical lines are the n-strips with a pitch of 50 μm. The 3 MΩ bias resistors are connected to the top ends of the n-strip diffusions. The bias line and the guard ring are located as on the p-side. On the n-side the bonding pads must be located at the left end of the detector just as on the p-side. This is done with a second metallization layer that has narrow lines going from the left end to the right end of the detector. One or more diagonal series of contact holes connect the lines of the second metal layer to the first metal layer on the n-strips. By certain multiplexing technique, the strip containing the hit signal can be found out. Figure 2.15. shows the location of the contacts between the two metal layers.

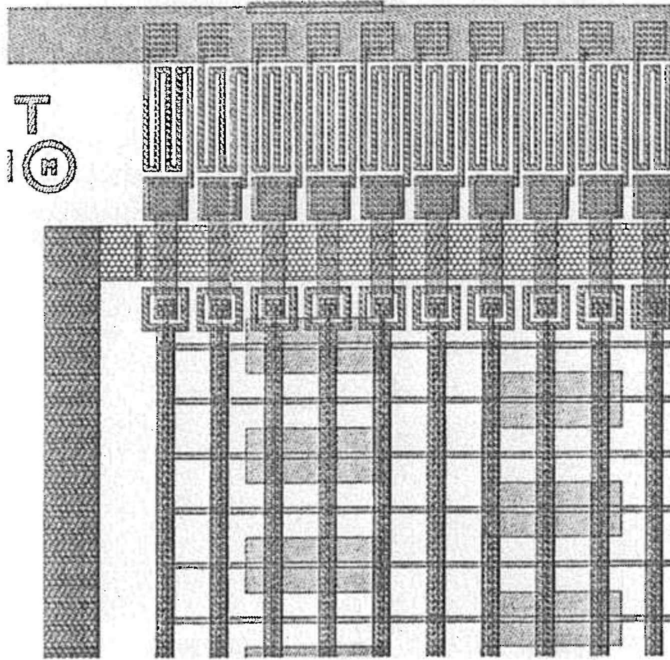

Figure 2.14. The layout of the n-side of a double-sided ac-coupled strip-detector.

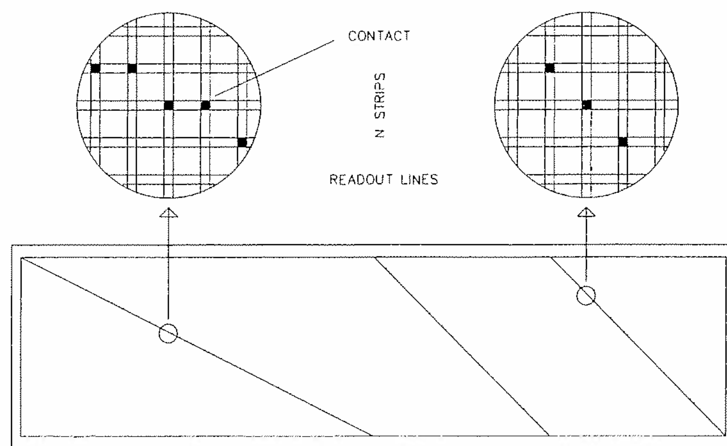

Figure 2.15. One example of n-strip multiplexing schemes.

Because there are n-diffusion strips that must be electrically isolated from each other on n-type silicon, several special organizations must be made on the n-side. First, unlike with single-sided detectors, the whole wafer thickness has to be depleted from charge carriers. Secondly, the electron accumulation layer caused by surface states and positive oxide charge has to be depleted between the n-strips, and between the guard ring and the ends of the n-strips. This is done with a negatively biased field plate extending outside the n-diffusion as shown in figure 2.16. At the other end of the strips the situation is more complex. The metal line bringing the bias voltage to the strip-diffusion has to exist. In our design, the problem was solved very simply. We used polysilicon as a readout electrode, which also forms the field plate. As seen in figure 2.14., the polysilicon forms a ring around the end of the strip. The metal line goes over this poly ring, and an oxide layer in between isolates the metal from the poly.

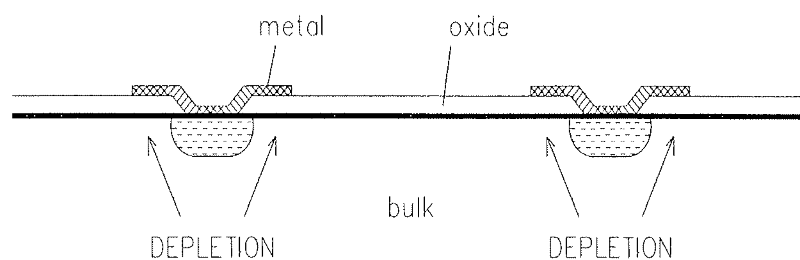

Figure 2.16. A field plate extending outside from the n-diffusion depletes the accumulation layer under the silicon dioxide and isolates the n strips from each other.

Figures 2.17. and 2.18. show the cross section of the p-side and the n-side of a double-sided detector. The bias line is seen in the left. The left end of the bias resistor is contacted to the common bias line. The right end of the resistor is contacted to a metal line, the right end of which is contacted to the strip diffusion. With this design we avoid an unreliable polysilicon-silicon contact. The guard ring that is located under this metal line, is not shown here. On the strip diffusion we have first a thin silicon dioxide layer that forms the coupling capacitance. On the oxide we have first a polysilicon layer, and on it the first metallization layer. On the n-side a thick low-temperature-oxide layer isolates the two metal layers from each other.

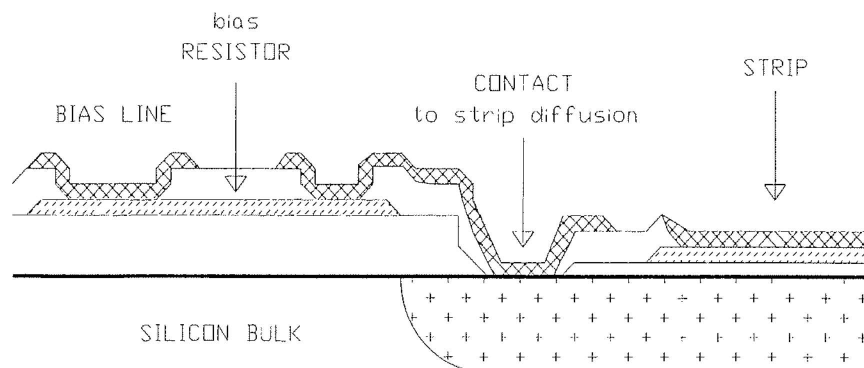

Figure 2.17. A schematic cross section of the p-side of a double-sided ac-coupled strip detector.

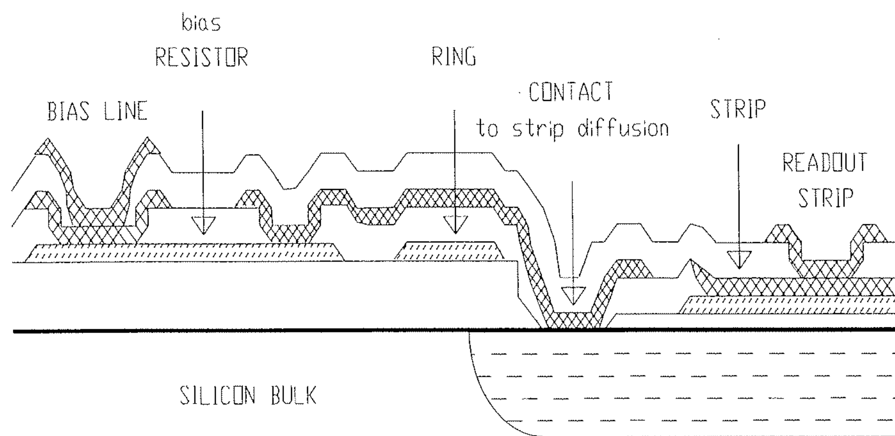

Figure 2.18. A schematic cross section of the n-side of a double-sided ac-coupled strip detector.

Chapter 3

Fabrication of particle detectors

Let us recall the basic dc-coupled p-i-n diode detector from chapter 2. If the device as shown in figure 2.9 is to be an ideal radiation detector, a set of requirements have to be met.

The noise which is caused by the reverse leakage current has to be kept small compared to the signal fluctuations. Generally this requires high generation lifetime in the detector bulk. In the case of a small-energy x-ray detector this leads to the requirement of cooling the detector (Walton& Haller).

The sensitive region must be free of charge trapping centers which could affect the amount of charge collected. The surfaces have to be passivated against detrimental effects from the ambients. Even more important it is to cover the surface with a high quality oxide or a suitable chemical compound in order to decrease the leakage current generated by the dangling bonds on the semiconductor surface. This subject is discussed more in connection with oxidation.

The incident radiation has to go through the metallization and the diffusion layer of the detector front surface. The contacts need to be thin enough to allow the passage of radiation without appreciable energy or intensity loss. This is a concern in photon detectors, but usually not in particle detectors.

The contacts need to remain non-injecting for reverse bias field strengths of 100 to 10 000 V/cm . This is easily met in silicon detectors.

The dopants could be diffused or ion-implanted. We always used ion-implantation. With ion-implantation precise control of dopant dose and penetration are obtained. The contacts can be shallower than those obtained by diffusion, 30 to 100 nm deep. The lower processing temperature also gives a higher lifetime. The passivation oxide has still to be grown and the dopants have to be annealed at 600 to 800 °C for 10 - 30 minutes. The diffusion patterning can be accomplished with photolithographicly opening the oxide windows as with diffused junctions, or by using a patterned photoresist as an implantation mask. Ion-implanted detectors are very rugged and have fairly thin entrance windows. In some cases the ion-implantation damage could increase the leakage current.

3.1 Development of the process parameters

In the very first process we made a large (58 mm x 32 mm) dc-coupled strip detector with a readout pitch of 25 μm and a strip width of 5 μm , and a variety of single dc-diodes and capacitors (Publication I). Two masks were needed: one for defining the p-diffusion and one for defining the front side metal. The process is described shortly in table 3.1.

Table 3.1. The flow of the first radiation detector process.

RAW MATERIAL		
hyperpure silicon	Wacker	
orientation	<111>	
growth	FZ	
type/dopant	n/P	
resistivity	2000 ± 600	Ωcm
lifetime	> 100	μs
thickness	525 ± 25	μm
INITIAL OXIDATION		
800 °C	wet 130 i	100 nm
LTO (Low Temperature Oxide)		
425 °C	280 mtorr	1000 nm
OXIDE ETCHING		
p area patterning		
backside stripping		
P TYPE DOPING		
implant	boron	20 keV 5E14 cm^{-2}
BACKSIDE DOPING		
implant	phosphorus	30 keV 3E15 cm^{-2}
ANNEALING ALTERNATIVES		
800 °C	30 i	x_j = 0.18 μm
900 °C	30 i	x_j = 0.28 μm
800 °C	20 h	x_j = 0.30 μm
900 °C	5 h	x_j = 0.52 μm
METALLIZATION		
aluminum	50 nm	front side
	500 nm	back side
METAL PATTERNING		

The process was designed to test two different philosophies: either maintaining the raw material properties by using only low processing temperatures, or even improving the material characteristics by using standard integrated circuit manufacturing temperatures in accordance with good backside gettering.

The lowest useful temperature, 800 °C, was chosen for the initial oxidation. To mask the boron implantation trough the oxide openings we had to deposit 1000 nm of LTO (Low Temperature Oxide) on the thermal silicon dioxide. The wafers were divided into four groups for annealing.

It was thought that the lower annealing temperature, 800 °C, does not cause significant diffusion of lifetime killing impurities. The higher annealing temperature, 900 °C, together with high-dose phosphorus implantation on the backside, was known to provide good gettering (Kang & Schroder). The different annealing times were selected to vary the depth of the pn junction x_j .

The results of leakage current measurements of the diodes are displayed in figure 3.1. "D" presents the total diode leakage current. "pn" presents the vertical leakage current of the pn junction when the lateral current is sucked away by maintaining the first guard ring of the diode in the same potential as the center but measuring only the current through the center.

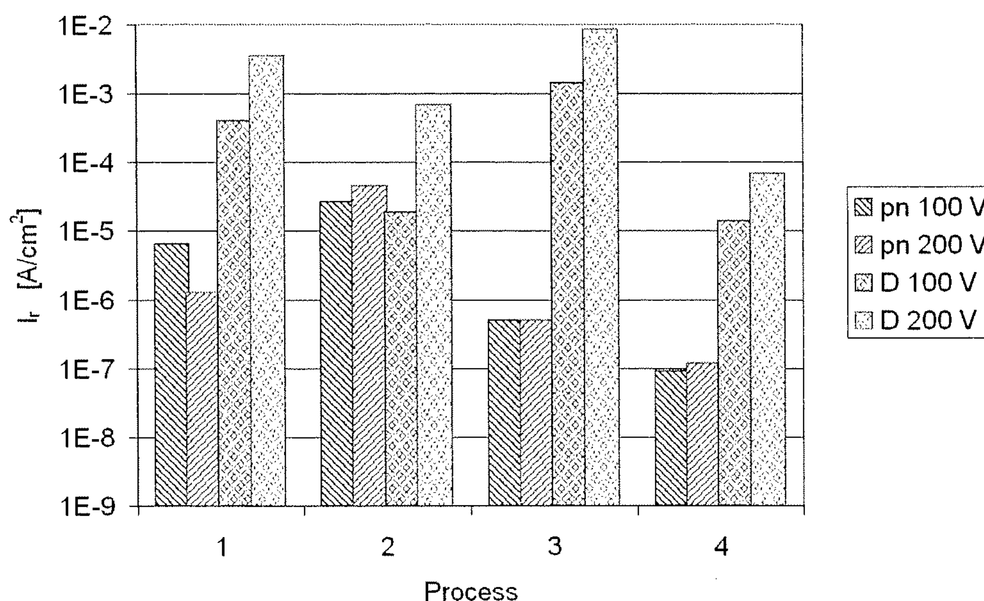

Figure 3.1. Leakage currents in the four process alternatives. Anneals: 1) 800 °C 30 i $x_j = 0.18$ µm , 2) 900 °C 30 i 0.28 µm , 3) 800 °C 20 h 0.30 µm , 4) 900 °C 5 h 0.52 µm .

Diode leakage currents are large as compared with the best values found in literature (1 nA/cm^2/100 µm) (Kemmer 1980, Kemmer 1982) and the surface and edge leakage is dominant. The high surface leakage, ie. the generation under the silicon dioxide, is caused by positive oxide charge and surface states in the silicon-oxide interface. A higher annealing temperature in processes 2 and 4 improved the interface quality and decreased the diode leakage current. Figure 3.2. shows the results of MOS-CV measurements with the same wafers. A rather satisfactory correlation between diode leakage current and surface-state density Q_{ss} can be seen.

The leakage current of the pn junction, ie. the generation in the bulk and in the junction, is lower after a long anneal. The junction depth also increases in the long anneals. The crystal defects caused by ion implantation of boron with 20 keV extend only to a depth of about 0.1 µm. The main reason for the decreasing leakage current must be gettering during the longer anneals, specially at 900 °C, but some gettering occurring already at 800 °C. The best generation lifetime calculated from equation 2-15 is 300 µs , which seems to be slightly longer than the recombination lifetime specified for the raw material mentioned in table 3.1.

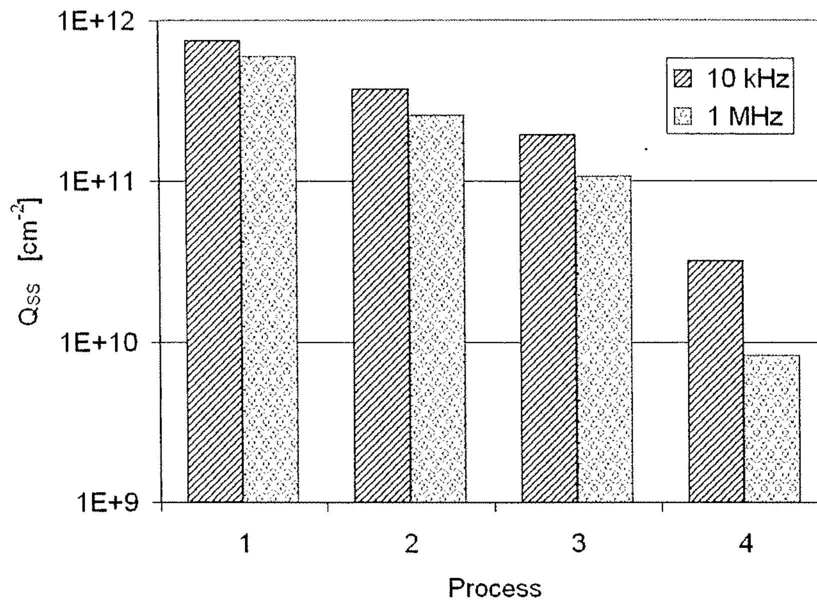

Figure 3.2. Surface state density Q_{ss} in the four processes.

What do we learn about these results? First, the initial oxidation temperature was absolutely too low. A higher oxidation temperature or also a higher annealing temperature improves the silicon-silicon dioxide interface quality remarkably. The growth temperature is the most significant factor determining the interface quality.

Secondly, we found that the lifetime killing impurities begin to move significantly already at 800 °C. A higher temperature and a longer time either increase or decrease the lifetime in the bulk depending on the cleanliness of the process and on the gettering conditions (Kang & Schroder).

3.1.1 The Kemmer principle

The fabrication of radiation detectors on high purity silicon by the planar process was first studied by Josef Kemmer in the Technical University of Munich (Kemmer 1980). Kemmer has also described many basic structures used in radiation detectors and also patented these and some fabrication steps which obey the so called "Kemmer principle" (Kemmer 1984-1985).

The Kemmer process involves two critical high temperature treatments, necessary during the passivation oxidation at 1030 °C and during implantation activation at 600 °C , which may reduce the charge carrier lifetimes. In order to get detectors of the same quality as surface barrier detectors a lifetime of at least 100 μs is necessary.

Exclusively <111> oriented wafers have been used in radiation detector fabrication. Oxide passivation is usually done at 1030 °C in dry oxygen or steam, leading to SiO_2 layers of 160 to 600 nm. To improve the quality of the oxidized wafers 1 to 3 percent of hydrogen chloride was added to the oxygen. Back diffusion of impurities during the oxidation process was avoided by closing the quartz tube of the furnace. For the p-type implantation, boron was used at an energy of 10 to 15 keV and a dose of $5 \cdot 10^{14}$ cm^{-2} and 10^{13} cm^{-2} for standard and position sensitive detectors, respectively. The rear was implanted with arsenic at an energy of 30 keV and a dose of $5 \cdot 10^{15}$ cm^{-2} . The implant activation was done at 600 °C for 30 minutes.

With the process described above, Kemmer has achieved a generation lifetime in the bulk as high as 15 ms , which is higher than the recombination lifetime of the starting material measured by the photoconductive decay method (Kemmer 1984).

The very high bulk generation lifetime obtained by Kemmer can't be explained by known gettering mechanisms. Kemmer used arsenic as the backside dopant, which is inefficient in gettering. Also oxidation is inefficient in gettering. It has even been said, that a recombination lifetime over 0.5 ms after oxidation is quite respectable (Pang et al.). In our CMOS processing line the furnace was cleaned with HCl before a critical oxidation, and no HCl was used during the oxidation. In a CMOS oven the process gases flow continuously. Kemmer's secret must be in closing the furnace during the oxidation, ie. there is no gas flow, and gettering the transition metals and silicon interstitials from the bulk with HCl. The exact mechanism is however not known. The final result is also very sensitive to the temperature at which the dopants are annealed. An attempt to incorporate higher annealing temperatures has been reported to decrease the lifetime tremendously, e.g. to less than 30 µs after annealing at 900 °C (Holland).

3.1.2 Oxidation

To find the best oxidation temperature in respect to surface states in the oxide-silicon interface, an oxidation test was made. The results are shown in figure 3.3. On the value axis we have the total effective charge density Q_{ss} calculated from a MOS-CV measurement. The quantity of this charge had no correlation with the oxide thickness, so we concluded that it must be originated only from the interface. With <100> wafers the interface is continuously improved when the oxidation temperature is raised, and dry oxidation yields a better interface than wet oxidation. Surprisingly the best oxidation temperature with <111> wafers is around 1050 °C , which has been most commonly used in detector and power device fabrication. In addition there is no difference between dry and wet oxidation.

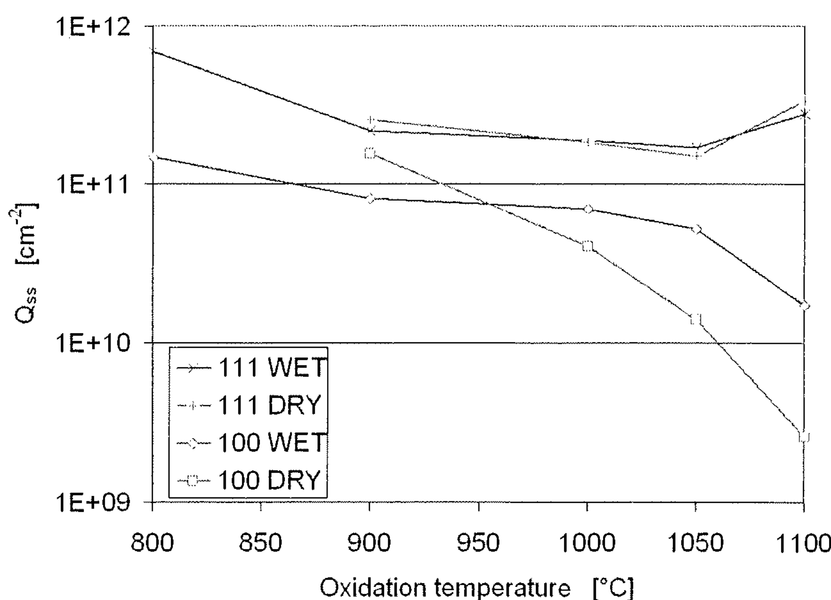

Figure 3.3. Surface state density as a function of oxidation conditions and crystal orientation.

This result means that the tradition to make radiation detectors on <111> oriented silicon wafers is not necessarily correct. If there is free silicon dioxide surface, ie. surface without a heavier p- or n-type diffusion, the contribution of the surface generated leakage current can be significant. In the strip detectors, where actually most of the detector surface is covered by silicon dioxide, the surface generated leakage is dominant when using <111> wafers. This has also been verified by measuring the diode leakage current in <100> and <111> wafers (Holland).

A further test was made to find out the best oxidation with respect to breakdown voltage of a 200 nm thick oxide layer needed in ac-coupled strip detectors. This test was made only between 1000 and 1050 °C. The results are shown in figure 3.4. A slight maximum seems to be at 1030 °C, and no difference is seen between wet and dry oxidation. The surface states were also measured, but no new results were obtained, the best temperature is still 1050 °C.

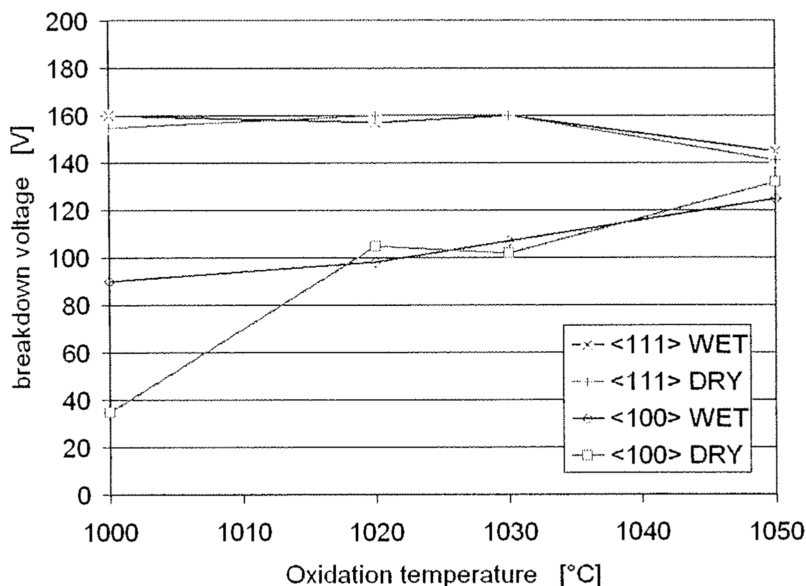

Figure 3.4. Breakdown voltage of a 200 nm silicon-dioxide layer grown at different temperatures.
The <100> wafers used in this test were polished by bright etching, which did not produce a high quality surface.

3.1.3 Gettering

By the Kemmer principle a bulk generation lifetime higher than 10 ms can be obtained. Often the strict rules of the technique can't be obeyed. Especially for the strip detectors with a large number of channels, integrated readout electronics is desired. Even on a smaller scale, devices such as the semiconductor drift chamber would also benefit greatly from integrated front-ends by reducing the circuit capacitance in order to exploit the extremely low capacitance of these detectors. Hence, a modern detector process should induce minimal contaminants and be compatible with contemporary integrated circuit fabrication techniques.

Processes compatible with conventional IC processing can be used if a gettering layer can be formed on the back side of the wafer. The sensitivity of the process to variations in the fabrication environment is greatly reduced and relatively high processing temperatures can be used, which removes a major obstacle to monolithic integration of front-end electronics with the detector.

Typical extrinsic gettering techniques (ie. gettering of impurities into the back side of the wafer) include phosphorus doping, ion implantation and deposition of thin films such as polysilicon and silicon nitride. A leakage current $0.5\ \mathrm{nA/cm^2/100\ \mu m}$ has been obtained in a standard diode process using thick (1 μm) in-situ doped polysilicon layer as a gettering layer on the back side (figure 3.5). After making PMOS transistors on the same substrate and processing the device at 900 °C for 3 hours, the leakage current is still less than $1.5\ \mathrm{nA/cm^2/100\ \mu m}$, which corresponds to a lifetime of 6 to 7 ms (Holland).

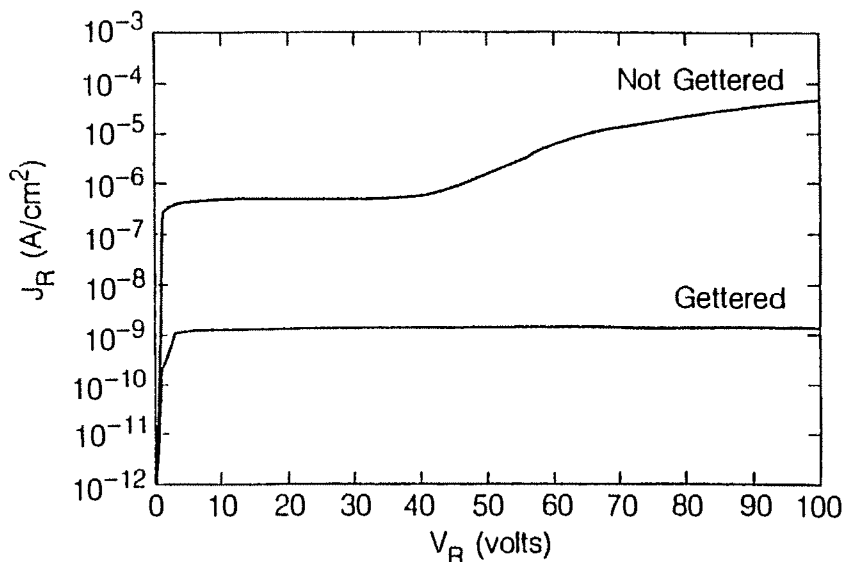

Figure 3.5. The detector reverse leakage current for a device with backside gettering compared to one without (Holland).

Very clean processing conditions and back side gettering has been applied throughout this work. In short processes the effect of back side gettering is evident. In a very long strip-detector process, where we grew the 200 nm coupling oxide in dry oxygen, we tested several extrinsic gettering techniques, like ion-implanted heavy phosphorus doping ($3\cdot10^{15}$ and $10^{16}\ \mathrm{cm^{-2}}$), heavy phosphorus deposition (900 °C 45 i) and phosphorus doped polysilicon. No difference between the methods was seen and the resulting lifetime was only around 100 μs. This could be explained by the very long process, during which the impurities diffused back to the substrate. In a shorter process the best achieved lifetime has been about 6 ms when using a back side gettering layer made by implanting a phosphorus dose of $3\cdot10^{15}\ \mathrm{cm^{-2}}$ at 30 keV .

3.2 The double-sided strip detector process

There are many common process steps in making double-sided strip detectors and modern energy dispersive detectors. Both benefit from good passivation oxide, gettering and wafer cleaning. Both are also double-sided, and two-sided lithography and alignment is needed. This applies also to the devices where a uniform p-diffusion is said to be on the back side. If there is a p-type layer on n-type wafer, and especially if there is a large reverse voltage over that junction like in the case of two-sided depletion, the p-type area can't extend to the edge of the

device. If that happens, large leakage currents are generated in the depletion region at the chip edge. In addition there must be a guard structure around the active p-area to prevent breakdown at the junction edge. Figure 3.6. shows the junction breakdown voltage in a high-resistivity material as a function of junction depth. In a radiation detector process we can't diffuse the junction very deep, so a breakdown will occur without a guard ring structure.

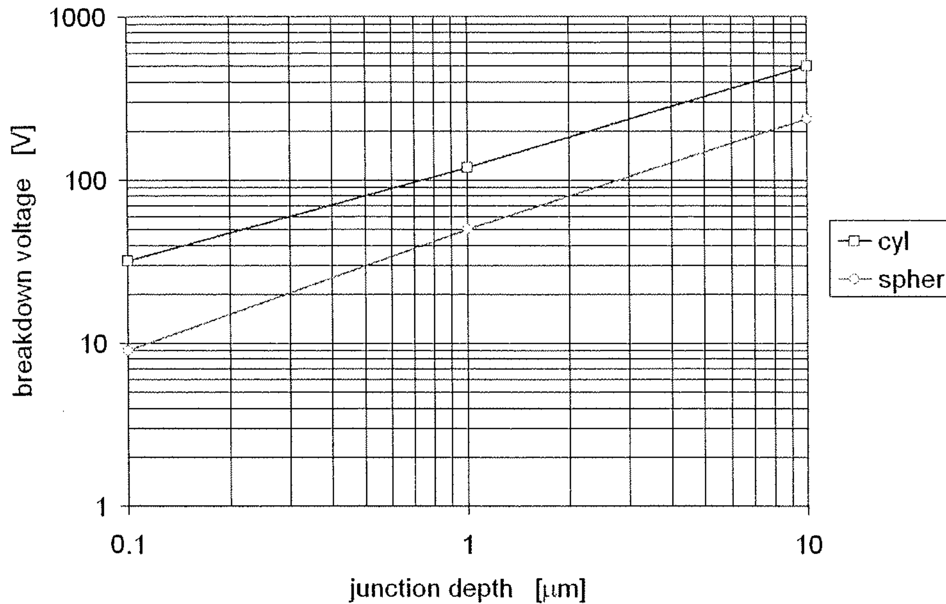

Figure 3.6. Junction breakdown voltage as a function of junction depth in high-resistivity silicon for cylindrical and spherical junctions.

3.2.1 Wafer cleaning

In order to maintain the long lifetime in the silicon bulk, the wafer surface has to be kept clean during high temperature treatments and the high temperature environment has to be cleaned before processing. This is very important in CMOS processing, still more important in power device processing and an absolute prerequisite to the success of radiation detector processing.

A preliminary clean-up treatment with a hot piranha was used for grossly contaminated wafers having visible residues, such as photoresist. This treatment is explained in table 3.2.

Table 3.2. Piranha cleaning.

STEP	SOLUTION	°C	ii:ss
Piranha	H_2SO_4 / $(NH_4)_2S_2O_8$	120	10:00
	3.5 l / 10 g		
rinse	DI water	25	10:00
dry			10:00

Standard RCA cleaning steps are applied before every high temperature treatment and film deposition. They consist of RCA-I, HF and RCA-II steps. The process is described in table 3.3.

Table 3.3. RCA cleaning.

STEP	SOLUTION	°C	ii:ss
RCA-I	NH_3 / H_2O / H_2O_2	80	10:00
	1 / 5 / 1		
rinse	DI water	25	10:00
HF dip	HF 1/50	25	00:30
rinse	DI water	25	10:00
RCA-II	HCl / H_2O / H_2O_2	80	10:00
	1 / 5 / 1		
rinse	DI water	25	10:00
drying			10:00

In the first step the wafers are exposed to a hot mixture of water-diluted hydrogen peroxide and ammonium hydroxide. This procedure was designed to remove organic surface films by oxidative breakdown and dissolution to expose the silicon or oxide surface for concurrent or subsequent decontamination reactions. Group I-B and II-B metals and several other metals, including gold, silver, copper, nickel, cadmium, zinc, cobalt and chromium, are dissolved and removed by the complexing effectiveness of ammonium hydroxide; copper, for example, forms the $Cu(NH_3)_4^{+2}$ amino-complex.

The third step exposes the rinsed wafer to a hot mixture of water-diluted hydrogen peroxide and hydrochloric acid. This procedure was designed to remove alkali ions and cations such as Al^{3+}, Fe^{3+} and Mg^{2+}, that form NH_4OH-insoluble hydroxides in basic solutions. This third step also eliminates metallic contaminants that were not entirely removed by the first treatment, such as gold. Electrochemical displacement replating of heavy metals from the solution is prevented by formation of soluble complexes with the dissolved metal ions.

Since the hydrous oxide film from the RCA-I treatment may trap trace impurities, its removal before the RCA-II step is beneficial. A 15 s immersion in 1 % HF-H_2O solution is sufficient to remove this film, as evidenced by the change from the hydrophilic oxidized surface to hydrophobic after stripping. However, unless high-purity and point-of-use ultrafiltered and particle-free HF solution is used under controlled conditions, more harm than good can result. A silicon surface that was exposed to HF is highly reactive and immediately attracts particles and organic contaminants from solutions, DI water and the ambient air. The RCA-II solution, which has no surfactant activity, will not eliminate these contaminants (Kern).

Before high temperature treatments the furnace is always cleaned with HCl. The standard treatment has been a mixture of HCl and N_2 for 30 minutes at 1050 °C.

3.2.2 Two-sided lithography

Process steps affecting only one side of the wafer at a time, like ion-implantation, need no special attention. The standard lithographic steps are applied to the wafer surface being processed. Great care must of course be taken not to damage the other surface. Photoresist baking on hot plates or wafer handling on scratching grabbers is forbidden.

At the process steps affecting both surfaces of the wafer, like wet or plasma etching, the photoresist must be in condition on both sides. The fastest way to pattern some layer on both sides of the wafer would be such that the photoresist is patterned on both sides and the wafers are wet etched. With our equipment this seemed to be impossible, because the pattern quality could not be maintained simultaneously on both sides. We chose a longer way.

If an etching step affects both sides of the wafer, photoresist is dispensed and spinned on the first surface, softbaked in an oven, exposed, immersion developed and hardbaked in an oven. Then photoresist is dispensed and spinned on the second surface, with extreme care of the first surface, and hardbaked. The wafer is etched now to pattern the layer on the first surface. The photoresist is removed from both sides. The surfaces are then reversed and the same steps are applied again to pattern the same layer on the second surface of the wafer.

The two-sided alignment is usually done with a two-sided mask aligner. The alignment system uses mirrors, which see both sides of the wafer simultaneously; or infrared light is used to see through the wafer; or two masks are aligned to each other and the wafer is transported between these masks and aligned to the top mask. No such system was available at us. Instead we utilized the good mechanical prealignment accuracy of an ASM wafer stepper. The repeatability of the alignment is $4\ \mu m$ in X direction and $7\ \mu m$ in Y-direction (1 sigma values). There could be a systematic error in rotation and symmetry, but those can be checked and adjusted to minimum before making the first alignment marks on the process wafers. In a Canon stepper the prealignment accuracy was only $\pm 40\ \mu m$, and we improved the double-sided alignment accuracy by a factor of 10 by inspecting the corners of the wafer flat with the prealignment camera and correcting the prealignment manually before exposing the first layer on each side of the wafer.

3.2.3 Using a wafer stepper

In the first process runs we used a contact aligner to pattern the photoresist. After starting to fabricate several batches of strip detectors, this method was found impractical.. The alignment was done manually and the accuracy was dependent on the operator and could not be better than 0.5 µm. The practical resolution could be reduced to 2 µm, but was generally 4 to 5 µm. The masks wore and got dirty and must be changed after a few exposures. The lithographic defects arising from the close contact between the mask and the wafer were also numerous.

The size of the double-sided strip detectors processed at VTT was about $79\ mm \times 21\ mm$, which suggests using a contact aligner, because the maximum image size of the used ASM stepper was only 10 mm x 10 mm. An important observation was made that, if the detector is divided to cells of suitable sizes, the strip detectors can be constructed from nine different parts: there are four different corner parts; each of the four edges can be assembled from one part that is repeated along the edge; the center of the detector can be assembled from only one part that is repeated for all the cell columns and rows in the central area.

The ASM stepper has a reticle blanking facility which makes it possible to select different areas on the reticle to be used as an image during the exposure of one cell. For every cell on the

wafer, an image size and shift can be selected. The image size is equal to the X and Y dimensions of the selected area on the reticle; the image shift is equal to the X and Y distance of the center of the selected area from the center of the reticle. For every shift on the reticle, a corresponding shift on the wafer (die shift) can be given. This is equal to the X and Y distance of the center of the exposure field of that particular cell from the center of the cell. Figure 3.7 visualizes the three levels of a stepper job.

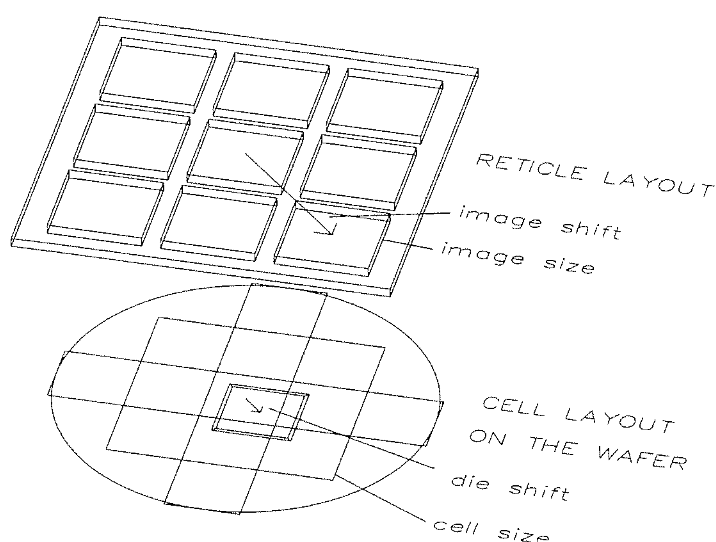

Figure 3.7. Relationships of wafer cell layout, die shifts and image sizes and shifts.

One selected area on the reticle together with its shift on the wafer forms one shift number. Our ASM stepper could use two reticles, A and B, and only seven freely usable shift numbers per one reticle. However the machine allowed to use the B shift numbers also on the A reticle. Utilizing this, we could take all the nine parts from one reticle and could use the other reticle for test structures. This design is visualized in figure 3.8.

In the figure the reticle parts are named according to ASM shift numbers. Reticle A is actually like a small detector with every part in its correct place, the only difference being that there must be a black area of at least 600 μm (on the wafer level) between the parts because of the inaccuracy of the reticle blanking system. The named reticle parts appear in the lower part of the figure, showing where (in which cell) a particular part of the reticle is exposed to assemble the detector. The parts on reticle B are test chips and can be exposed freely anywhere on the wafer.

The method has several advantages and disadvantages. Many, but not any, detector sizes can be exposed with the same reticles, because the actual size of a detector is determined by the job that tells the stepper computer what to do. With the same reticles the length or width of the detectors can be

$$L = n\,A + B \quad , \tag{3-1}$$

where n is a positive integer, A is the length or width of the center part (A0) and B is the sum of the lengths or widths of the corresponding edge parts. All factors can be selected quite freely.

The disadvantage is that only one type of detectors can be made on one wafer, so all dimension and structure tests must be made with some other method. The method to pattern strip detectors with a reduction stepper is explained in detail in Publication VI.

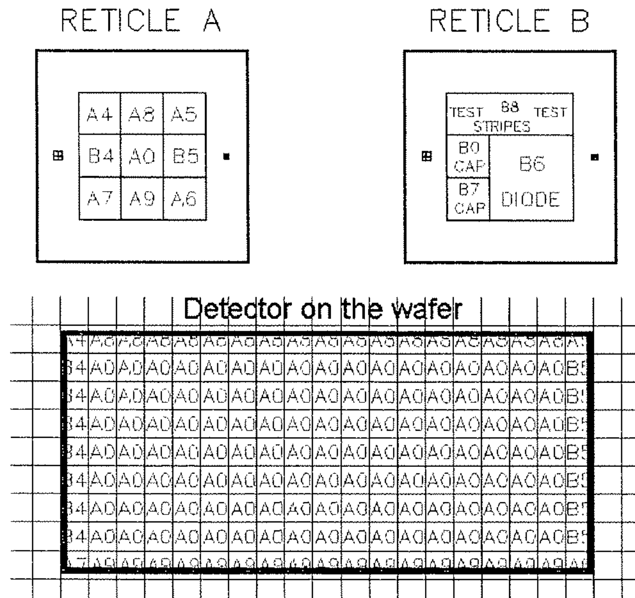

Figure 3.8. The method of assembling a large strip detector from nine small parts.

The resulting wafer layout is displayed in figure 3.9. We have fitted on the wafer two long strip detectors, two smaller strip detectors, two elementary strip detectors, diodes, capacitors and several test structures. The cell layout is shown as a square-ruling over the wafer.

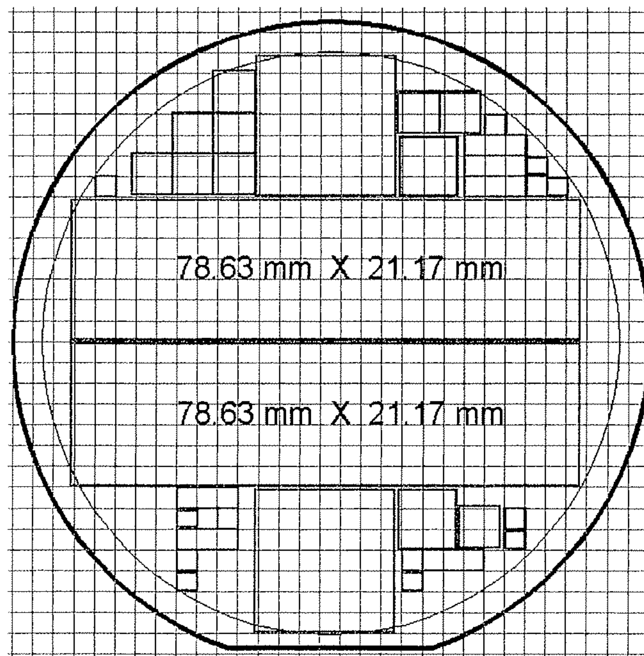

Figure 3.9. The p-side of the double-sided strip-detector wafer.

3.2.4 Polysilicon resistors

Large bias resistors are needed in ac-coupled strip detectors. The values used at VTT ranged from 3 to 20 MΩ. Several ways to produce good quality high sheet resistance polysilicon or amorphous silicon resistors were investigated. All tests obeyed the same formula. First a thin amorphous silicon layer was deposited on an oxidized silicon wafer. A dose of boron, phosphorus or arsenic was implanted into the amorphous silicon. The wafers were annealed first at low temperatures and then in higher and higher temperatures, and the sheet resistance was measured after every anneal.

First we tried to make resistors from amorphous silicon. On some wafers a uniform resistivity was obtained at about 1 MΩ/square with a very high implantation dose ($3 \cdot 10^{16}$ cm^{-2}), but this was not repeatable. Usually the sheet resistance was either too non-uniform or fell below 1 kΩ/square when the amorphous silicon started to crystallize at about 600 °C. No stable and repeatable high sheet resistance was found with any tested dopant.

In the next trial we deposited a 250 nm thick amorphous silicon layer on oxidized wafers at 570 °C at a pressure of 500 mtorr . We implanted arsenic at 120 keV with several doses, and annealed the wafers at temperatures between 400 and 1000 °C . The results are shown in figure 3.10. After annealing at a higher temperature than 600 °C the sheet resistance becomes almost independent of the annealing temperature at doses higher than 10^{14} cm^{-2} and the uniformity is better than 2 % . The obtained stable sheet resistance value is at most 100 kΩ/square . Similar, but worse, results have also been obtained elsewhere. The processing conditions were however not told (Quick Reference Manual).

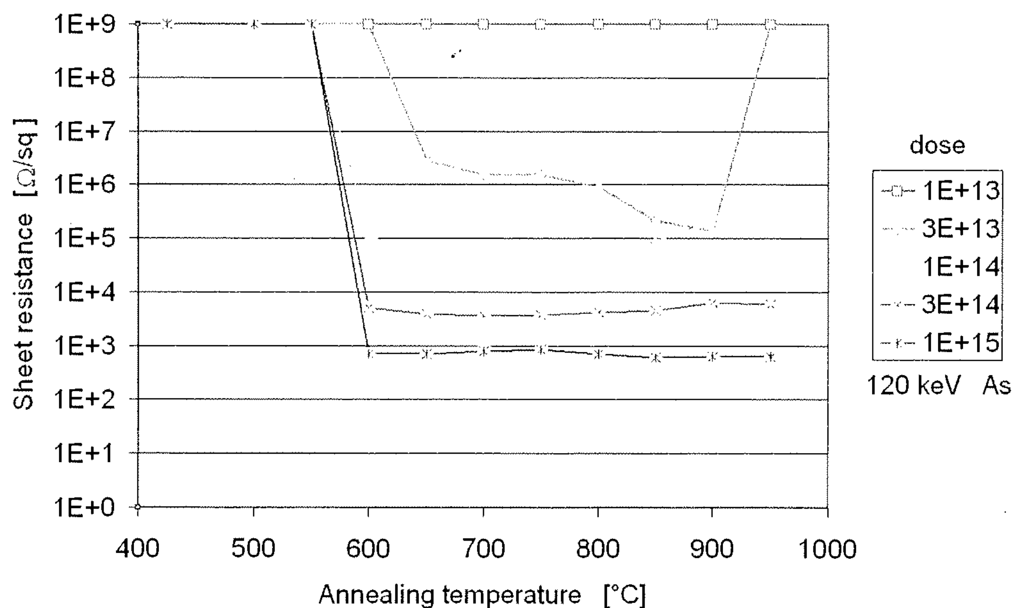

Figure 3.10. Sheet resistance versus annealing temperature for arsenic implant into amorphous silicon.

An important observation is that the resistance remains at the same value even though new anneals are made with new temperatures, which does not apply to boron doped polysilicon resistors (Evensen et al.). 3 MΩ resistors with a sheet resistance of 30 kΩ/square made with this method were irradiated with a ^{90}Sr beta dose of 190 krad and a decrease of 10 percent was measured in the resistance value.

3.2.5 The process

The cross-sections of the p and n strips are shown in figure 3.11. A thin 200 nm silicon dioxide covers the strip diffusion and forms the coupling capacitance. On top of the oxide we deposit a 250 nm polysilicon layer to protect the thin oxide. Because the sheet resistance of a polysilicon film can't be made much smaller than 20 Ω/square, we need to open a contact hole in the low-temperature oxide deposited over polysilicon, and cover the polysilicon with a metal layer.

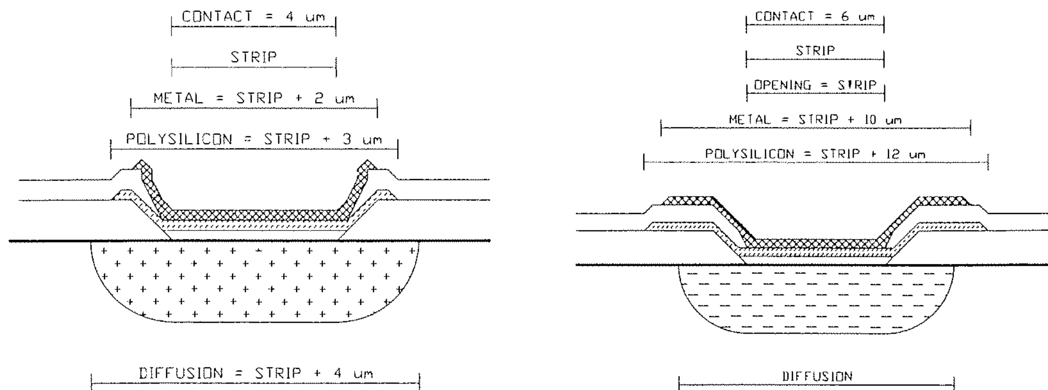

Figure 3.11. Cross-section of a p-strip (left) and an n-strip (right).

The main steps of the process are listed in table 3.5 and the specifications for the raw material, the wafers, are given in table 3.4. Double-side polished hyperpure thin silicon wafers were used as a starting material. A resistivity over 3500 Ωcm is needed to deplete the 300 μm thick wafer at a voltage smaller than 100 V. A generation lifetime of 1 ms gives a bulk leakage current of about 0.5 μA in a long detector, which is far less than the specification, 5 μA per detector. The process is carried out with 100 mm wafers, which is the diameter required by the automatic processing equipment. We have used mainly wafers with <111> orientation. Most of the surface of a strip detector is covered by silicon dioxide, and thus <100> wafers would give a smaller leakage current. Unfortunately thin <100> 100 mm wafers are so weak, that a large fraction of them were broken during a long process. The thickness (thinness) specification comes from the requirement that the high-energy particles should go through the detector without significant scattering. The flat is needed only by the automatic process equipment.

Table 3.4. Specifications for double-sided strip-detector wafers.

material	hyperpure silicon
growth	float zone
resistivity	> 3500 Ωcm
type/dopant	n/phosphorus
lifetime	> 1 ms
diameter	100 ± 0.5 mm
orientation	<111>
thickness	300 ± 25 μm
polished	both sides
flat	30 - 35 mm

Table 3.5. Process steps in making double-sided ac-coupled strip detectors.

alignment marks	plasma etched to silicon			
passivation oxidation	1030 °C	wet	85 i	600 nm
opening the diffusion areas	wet etch	BHF	35 °C	
n-side implantation	P	30 keV	3E15 cm^{-2}	
p-side implantation	B	30 keV	3E14 cm^{-2}	
coupling oxide	1030 °C	wet 15 i	dry 25 i	200 nm
amorphous silicon	570 °C	500 mtorr	250 nm	
amorphous silicon implantation	As	120 keV	1.44E14 cm^{-2}	
amorphous silicon patterning	plasma etch			
low temperature oxide	425 °C	280 mtorr	500 nm	
n-side first contacts	wet etch	BHF	35 °C	
annealing	800 °C	N_2	60 i	
n-side first metal	molybdenum	250 nm		
metal patterning	wet etch	aluminum etchant		25 °C
low temperature oxide	425 °C	280 mtorr	1000 nm	n-side only
n-side second contacts	wet etch	BHF	35 °C	
p-side contacts	wet etch	BHF	35 °C	
n-side second metal	aluminum	500 nm		
metal patterning	wet etch	aluminum etchant		35 °C
p-side metal	aluminum	500 nm		
metal patterning	wet etch	aluminum etchant		35 °C
sintering	425 °C	N_2/H_2	15 i	

Alignment marks

The ASM stepper uses alignment marks, that are etched into the silicon as the first process step. This is called mask level zero. The alignment marks are 120 nm deep relief patterns 90 mm apart from each other at the horizontal center axis of the wafer. They are etched into silicon by plasma.

To protect the silicon from dirt and scratches during this first process step, we grew a 50 nm oxide on the wafers at 800 °C in wet atmosphere. The furnace was cleaned with HCl before oxidation. The wafers went through RCA cleaning before oxidation. This oxidation is not considered to greatly affect the bulk lifetime.

The alignment marks were etched on both sides of the wafer according to the standard two-sided lithography as described earlier. Before exposing and etching the process wafers, a test wafer was exposed with a special job that makes graticule marks at the corners of the flat edge. The rotation and symmetry were inspected with a microscope. If needed, x-shifts were updated in the process jobs.

The photoresist was usually stripped by wet processing, with acetone, photoresist stripper or piranha. O_2 plasma ashing is avoided because of feared defects, but is necessary after some process steps.

Plasma etching generally is avoided in radiation detector processes, because it is considered to create radiation damage in the wafer. This damage is at least partially annihilated during high temperature treatments. In addition there is no comprehensive knowledge available, which plasma treatment causes significant damage and which doesn't. Measuring the effect is difficult, because an electrically good detector may have trapping centers that deteriorate the charge collection efficiency. To etch silicon or polysilicon accurately, plasma is however very necessary.

Passivation oxidation

To keep the surface generated leakage current low, the silicon surface must be passivated by a high quality oxide with a small mobile charge and few surface states. A thickness of at least 500 nm is needed, because later implantations are done with this oxide as a mask. The oxide is grown at the best temperature for <111> wafers, 1030 °C, in wet pyrogenic atmosphere for 85 minutes. The resultant oxide thickness is 600 nm. This is the most critical high temperature treatment, and furnace cleaning with HCl and wafer cleaning with RCA are a prerequisite for the success of the whole process.

The recombination lifetime is measured after passivation oxidation by a microwave reflection method to reveal serious contamination. For a thin wafer like these, where surface recombination is dominating, a value of 100 μs is sufficient after wet oxidation.

Opening the diffusion areas

Standard two-sided lithography is used in opening the oxide for diffusions. The thermal oxide of thickness 600 nm is etched in buffered hydrofluoric acid (BHF) at 35 °C for about 5 minutes. Photoresist is removed in acetone plus piranha. The resultant cross sections in selected places is shown in figure 3.12.

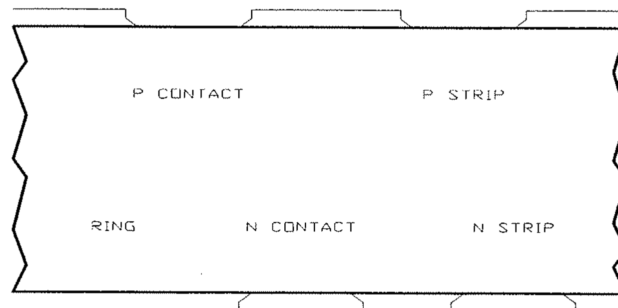

Figure 3.12. Cross section of the device in selected places after opening the diffusion areas.

Doping

The passivation oxide acts as a mask during dopant introduction. The n-side diffusions are implanted with a phosphorus dose of $3 \cdot 10^{15}$ cm^{-2} at 30 keV, and the p-side diffusions with a boron dose of $3 \cdot 10^{14}$ cm^{-2} at 30 keV. On the p-side a deep junction would be beneficial, but higher implantation energies can't be used when the passivation oxide is the only masking layer.

Before implantation a 50 nm protective oxide is grown at 800 °C in wet atmosphere just like before making the alignment marks. In this phase it is meant to protect the silicon against metallic impurities, which come from contacts with ion-implanter wafer handling mechanics and from the ion-beam induced sputtering of metals during implantation. This oxide together with its impurities is removed in BHF soon after implantation. The etching time is 60 s at 35 °C and about 150 nm of the passivation oxide is also removed. The impurities on the surface of the passivation oxide are thus also removed. In addition, about 80 % of the boron dose and about 100 % of the phosphorus dose in the passivation oxide is removed.

The coupling capacitor

A 200 nm thermal oxide is grown on the strips to form the coupling capacitance dielectric layer. To protect this oxide, a 250 nm amorphous silicon layer is deposited on the oxide immediately after oxidation.

This is the second high temperature treatment in the process. HCl cleaning of the furnace and a good RCA-cleaning of the wafers are necessary. The oxide is grown at 1030 °C. To grow the oxide as fast as possible, the first 15 minutes are wet oxidation. The last 25 minutes are dry oxidation for two reasons. First, the resultant junction depth on the p-side should be near 2 μm to withstand a 100 V reverse bias. Secondly, the surface recombination velocity is lower after dry oxidation (the last grown nanometers of the oxide are the most critical ones).

After oxidation the wafers are transferred directly from the oxidation furnace to the polysilicon furnace. The amorphous silicon is deposited at 570 °C at 500 mtorr. This same layer is also going to form the polysilicon bias resistors.

The junction depth and the sheet resistances are determined by the implantation and the growth of the coupling oxide. The resultant values are:

p-diffusion:	sheet resistance	545 Ω	junction depth	1.64 μm
n-diffusion:	sheet resistance	69 Ω		

The simulated final diffusion profiles are shown in figures 3.13 and 3.14. To make the n-strip isolation easier with the MOS-method, the n-diffusion should be as shallow as possible. In this process the n-diffusion falls to the background level at a depth smaller than 2 μm.

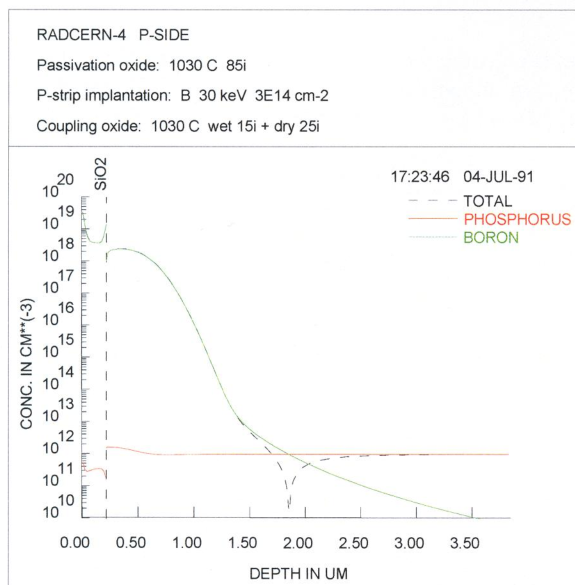

Figure 3.13. The final diffusion profiles on the p-side.

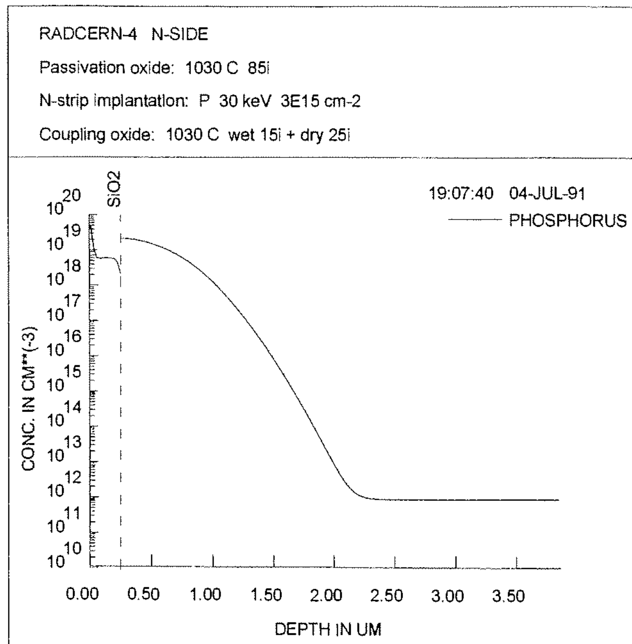

Figure 3.14. The final diffusion profiles on the n-side.

Doping the amorphous silicon

The resistivity of the bias resistors is adjusted by arsenic implantation dose of $1.44 \cdot 10^{14}$ cm^{-2} at 120 keV. Both sides of the wafer are implanted with no mask. The resultant sheet resistance after annealing at 800 °C is 30 kΩ/square . The cross section of the device in this phase is shown in figure 3.15.

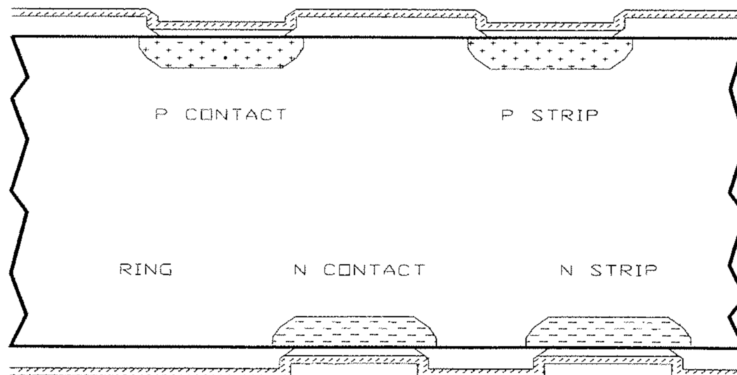

Figure 3.15. Selected parts of the device after doping the amorphous silicon.

Patterning the amorphous silicon

To achieve a good linewidth control and accuracy of the bias resistors, plasma etching is obligatory in etching the amorphous silicon. This was done in standard Cl_2 / He plasma for about 1 minute.

First intermediate dielectric

A 500 nm low temperature CVD oxide (LTO) is deposited on both sides of the wafer at 425 °C and 280 mtorr after polysilicon patterning. This layer passivates the bias resistors and forms a dielectric layer between the polysilicon and the first metallization.

Contacts are then opened into the LTO layer on the n-side only. The oxide is etched in BHF for about 5 minutes. The LTO must be over etched, because there is an additional 200 nm of thermal oxide in the diffusion contacts.

To decrease the contact resistance, an additional arsenic implant could be made to the contact openings.

Annealing

The amorphous silicon must be crystallized and its dopants activated to achieve a correct bias resistor value. This is done in nitrogen at 800 °C for 1 h.

The first metal on the n-side

After annealing the wafers are dipped for 60 s in diluted hydrofluoric acid (HF 1/50) at room temperature to remove any oxide from the contact openings on the n-side. A 250 nm layer of molybdenum is sputtered on the n-side to form the first metallization layer. Molybdenum was chosen, because it is as easy as aluminum to wet-etch, and because it could tolerate higher processing temperatures than aluminum. However, probably no problems would be encountered by using aluminum as the first metal. The resistivity of sputtered molybdenum is so high, that the sheet resistance of this layer is about 1 Ω/square.

The molybdenum is etched in aluminum etchant at 25 °C for 2 to 3 minutes and the photoresist is removed in acetone.

The second intermediate dielectric

A thick dielectric must be deposited between the two metal layers on the n-side to reduce the capacitance between crossing metal lines. We grew an LTO layer of a thickness 1000 nm. The p-sides are protected and almost no oxide grows on the p-side.

For n-side second contacts between the two metal layers the oxide is etched in BHF at 35 °C for about 5 minutes, and the photoresist is stripped in acetone.

P-side contacts

Before making the top metallizations, the contacts on the p-side of the wafer are opened. In poly contacts the 500 nm LTO layer must be overetched, because there is an additional thermal oxide layer of 200 nm in diffusion contacts.

Final metals

After a short dip in 1/50 HF, 500 nm of aluminum is sputtered on the n-side of the wafer. This is patterned and etched in aluminum etchant.

An aluminum layer of the same thickness is sputtered also on the p-side of the wafer, and patterned and etched.

The final treatment is metal sintering in a forming atmosphere, H_2/N_2, at 425 °C for 15 minutes. The final cross sections are shown in figure 3.16.

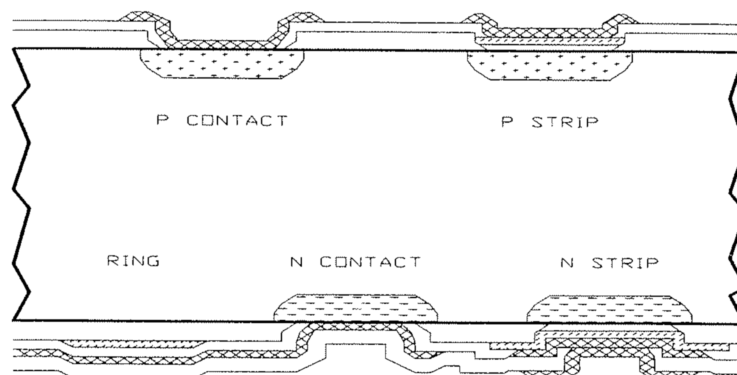

Figure 3.16. The final cross section in selected places of the strip detector.

Chapter 4

Characterization

When talking about characterization of radiation detectors, the subject must be divided into two categories: electrical measurements and radiation measurements. Most process-related electrical measurements were made at VTT. Many electrical measurements were also done in CERN and in Helsinki University in the department of High Energy Physics. All position resolution measurements with high-energy particles were done in CERN. Measurement of voltages and electric fields with a scanning electron microscope were done in Lappeenranta University of Technology.

4.1 Lifetime measurement

The most important question after processing energy dispersive radiation detectors is: what is the leakage current. Also with position sensitive detectors it is one of the most important concerns. The leakage current of a good silicon detector should be dominated by the bulk generation current, which is determined by the generation lifetime according to equation 2-15. In energy dispersive detectors a lifetime of several milliseconds is always desired, even 100 ms would be needed for some applications. In position sensitive strip detectors a lifetime smaller than 1 ms can be tolerated.

The hyper-pure silicon supplier measures the recombination lifetime of the ingot by the photoconduction decay method (Schroder). A laser pulse is shot on the ingot and the conductivity decrease as a function of time after the pulse is measured. The time constant of the exponential decay is the recombination lifetime.

In our radiation detector processes we had at least two lifetime monitoring wafers. One was measured after the first high-temperature oxidation of the process to reveal the quality of the starting material and the success of this process step. The other monitor went through all high-temperature steps, and its lifetime was measured at the end of the process. In addition we had some monitors that participated only in some intermediate high-temperature step.

We can measure the recombination lifetime in a wafer with the equipment shown in figure 4.1. A 25 W GaAs laser pulse of width of about 100 ns is shot on the wafer. It generates a cloud of electron-hole pairs. The wafer rests on the end of a waveguide, where we have a microwave radiation of 24 GHz . The microwave intensity reflected from the wafer is a function of the density of free charge carriers in the wafer. By measuring the change of the microwave reflectivity as a function of time after the laser pulse, we get the recombination lifetime in the wafer. Again the change is exponential, and the lifetime is the time constant of the wave form.

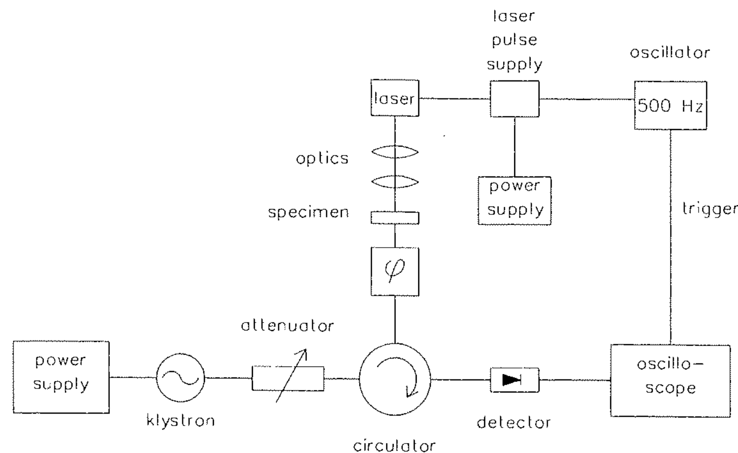

Figure 4.1. The block diagram of a lifetime measurement system.

Very high lifetimes can't be measured from a thin wafer with this method, because the surface recombination is dominating over the bulk recombination. Generally the diffusion length of the charge carriers should be at most half of the wafer thickness to facilitate measuring the lifetime accurately. With thin wafers this method is very sensitive to surface quality, which could be measured at least qualitatively very easily.

A lifetime of a non-oxidized wafer can't be measured easily with this equipment. It is however possible to immerse the wafer to some suitable acid (HF for example) that passivates the surface during the measurement. In a radiation detector process we usually measured the lifetime after the first oxidation, which passivates the surface of the wafer. The highest lifetimes of about 800 μs are measured when there is a pn junction on both sides of the wafer. The built-in electric field of the junctions forces the electrons to stay in the n-type bulk so that they can't recombine in the surface.

This is the only measurement that without polemics suggests that dry oxidation produces a better silicon-silicon dioxide interface than wet oxidation. Lifetimes measured by this method are always larger after dry oxidation than after wet oxidation.

The generation lifetime is measured with a diode processed on the wafer together with other structures. The measurement is a two-step process.

First, the resistivity of the silicon bulk must be measured. We do it with the diode capacitance-voltage (CV) method. The diode capacitance is plotted as a function of the reverse bias voltage applied over the pn junction. The length of the depletion layer is calculated from equation 2-23 and the corresponding doping density from equation 2-16. The resistivity in n-type material is obtained with equation 2-19. This gives the average resistivity of the material. If a profile is wanted, we must calculate the change of the length of the depletion layer as a function of the change in the reverse voltage. As a result we can calculate the resistivity ρ in kΩcm .

$$\rho = 2.50\, q\, \varepsilon\, A^2 \cdot \frac{\Delta(1/C^2)}{\Delta V} \quad , \qquad (4\text{-}1)$$

where ε is expressed in pF/cm, A in cm^2 and C in F,
as a function of depth in silicon d

$$d = \frac{\varepsilon A}{C} \quad . \tag{4-2}$$

After obtaining the resistivity of the material, the leakage current of a diode is measured as a function of the reverse bias voltage. As shown in figure 4.2 the same bias is applied to both the center diode and the first guard ring, and both currents are measured. With this method we can separate the bulk generation and lateral leakage (generation under the oxide plus possible junction break down) providing that the radius of the central area is much larger than the wafer thickness.

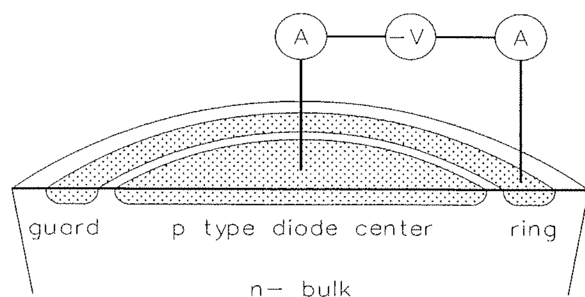

Figure 4.2. Measurement of the vertical and lateral leakage currents of a pn diode detector.

The generation lifetime can be calculated on the basis of equations 2-15 and 2-21, which give

$$\tau = \frac{n_i \, q}{2 \, I_l} \cdot A \sqrt{280 \, V \rho} \tag{4-3}$$

for n-type silicon. ρ is expressed in kΩcm, A in cm^2 and n_i in cm^{-3}.

4.2 Electrical tests

In the use of strip detectors only a very small leakage current flows through the structure. Large voltages are however applied to deplete the whole wafer thickness. This means that during electrical measurement of the detectors we do not need to worry about high contact resistances, but the isolations between conductive layers are critical. After ensuring that the structure in itself is in condition, the main interest focuses on pinholes in the 200 nm coupling oxide, on the coupling capacitance, on the accuracy of the polysilicon bias resistors and on the detector bias current.

The coupling capacitance was measured to be 1.0 nF in a 7 mm^2 test capacitor on both sides of the wafer, or 0.14 nF/mm^2 at a measurement frequency of 36 kHz which gave the best Q-value of the capacitance ($Q > 4$).

The design value of the bias resistors was 10 MΩ on the p side and 20 MΩ on the n side. The histograms of the measured values are displayed in figures 4.3 and 4.4. The average on the p side is 9.5 MΩ and on the n side 24.8 MΩ.

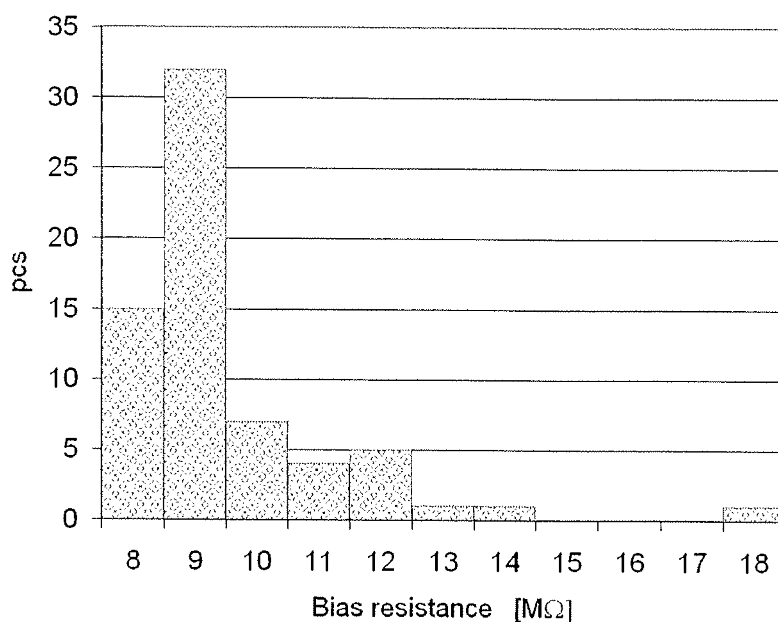

Figure 4.3. Histogram of the bias resistance values on p side. The bin averages are shown at the category axis.

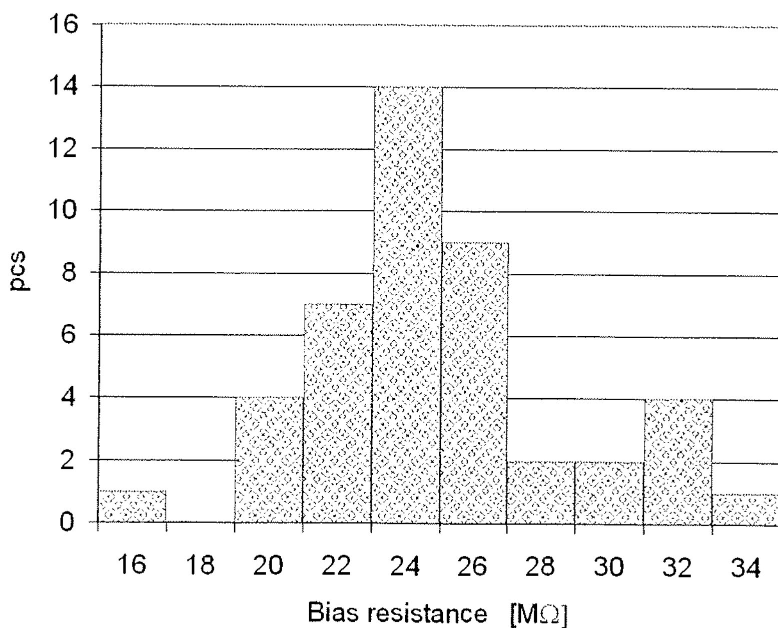

Figure 4.4. Histogram of the bias resistance values on n side.

The preliminary specification for the bias current at full depletion was $5\ \mu A$ per a long detector shown in figure 3.9. The resistivity of the bulk was measured to be about $4100\ \Omega cm$, which gives a depletion voltage of $84\ V$ for a $300\ \mu m$ thick wafer. The bulk lifetime was measured to be 3.1 ± 0.6 ms, which produces a bulk leakage current of $0.15\ \mu A$ for the long detector. The oxide-generated leakage is however dominating and the average bias current is $1.6\ \mu A$. A histogram of the measured leakage currents is shown in figure 4.5. The guard ring is connected to the same potential as the bias line. Its current is negligible at 80 V. At 100 V the guard ring current is over $10\ \mu A$ in some detectors.

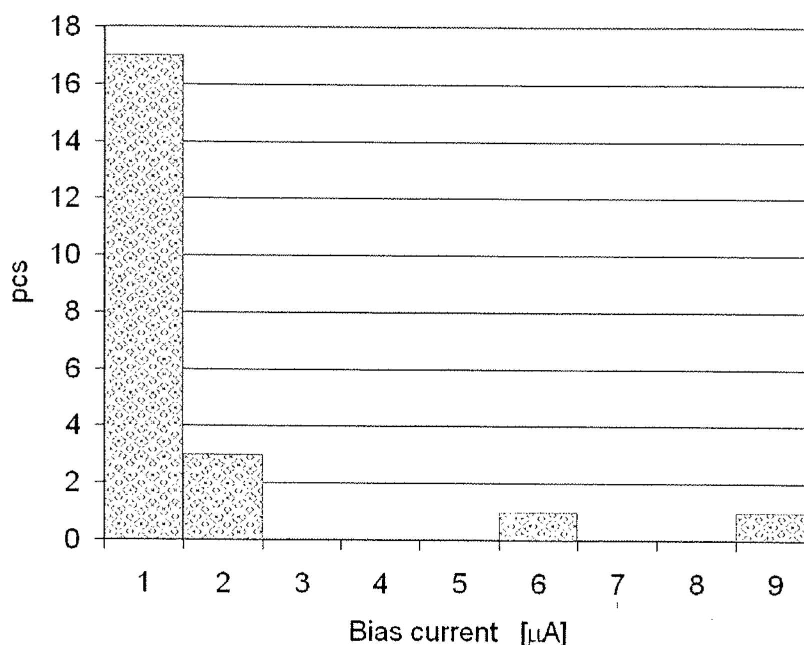

Figure 4.5. Histogram of the long detector bias current at full depletion. The detector area is $16.6\ cm^2$.

4.3 Beam tests

Two parameters were measured in beam tests: the signal-to-noise ratio and the position resolution.

The signal-to-noise ratio was measured with ^{90}Sr betas with a special setup shown in figure 4.6. Analog data from the readout chips was AD converted in a SIROCCO unit (Lang & Vanuxem) and further transferred into a computer. In order to achieve readout coincidence, i.e. detector readout when the actual signal from an electron was present in the detector, the readout timing had to be synchronized with the scintillator trigger signal. The wide energy range (< 2.2 MeV) of the ^{90}Sr source also required a certain energy threshold for the acceptable trigger signals. The cluster algorithm of the analysis software accepted a maximum of two adjacent strips in a cluster, demanding signals above $3 \cdot RMS$ or $4 \cdot RMS$ in both strips. One additional strip on both edges was added to the cluster to enable partial cancellation of noise clusters.

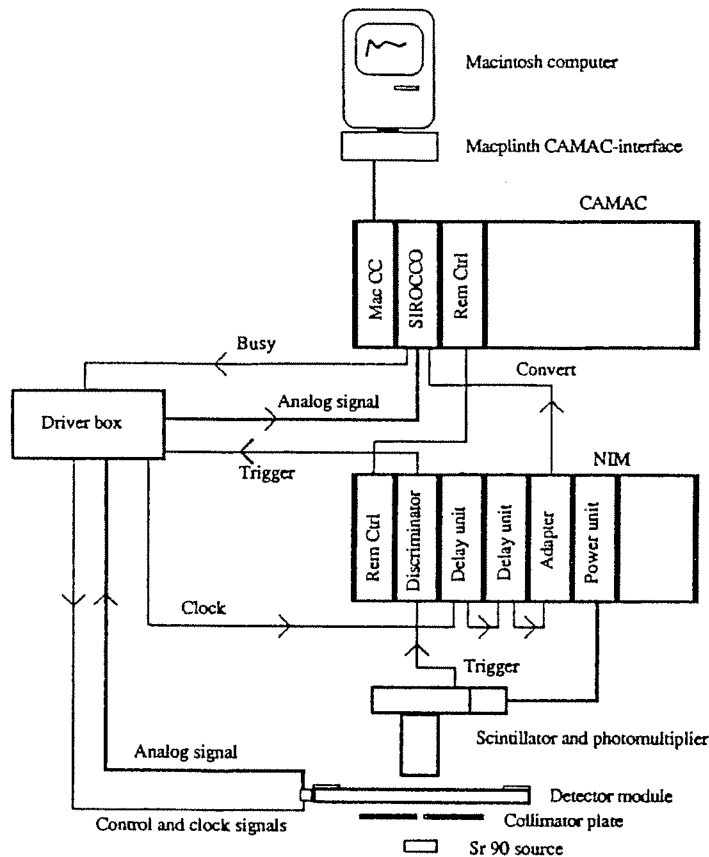

Figure 4.6. Setup used in beta-measurements .

Results from two separate runs with trigger level at 3·RMS (a and b) and at 4·RMS (c and d) are shown in figure 4.7. The signal-to-noise ratio 14 is obtained for a single-sided dc-coupled strip detector processed in the first trial described in chapter 3 (Publication I). With relativistic high energy pions this result was improved to a value 30 (Hietanen et al. 1991 (1)). On the p-side of a double-sided ac-coupled strip detector the signal-to-noise ratio was 35 for ^{90}Sr betas (Publication II) and 31 for pions (Hietanen et al. 1991 (2)). On the n-side of a double-sided ac-coupled strip detector the signal to noise ratio was 18 for ^{90}Sr betas (Publication III).

The position resolution measurements were done in CERN in SPS collider of the North Area using a relativistic particle beam consisting mainly of pions. Figure 4.9. shows the measurement system, where the test detector is located in the same beam line as four pairs of reference counters and three scintillators. The exact position of the beam was measured in two dimensions with the reference counters. The scintillator signals were used to trigger the readout.

The best measured position resolution was obtained for the first noisy dc-coupled strip detectors with a readout pitch of 25 μm and a strip width of 5 μm . Using a gaussian fit for the distribution of position signal and subtracting the predicted impact point error, a position resolution 3.9 μm was obtained. Using FWHM values, the corresponding sigma was 2.6 μm with LSI readout electronics (Hietanen et al. 1991 (1)).

For the p-side of a double-sided ac-coupled strip detector with a readout pitch of 50 μm , strip pitch of 25 μm and strip width of 5 μm the measured position resolution was 4.9 μm with gaussian fit (Hietanen et al. 1991 (2)). Figure 4.8 shows the result of this cluster analysis.

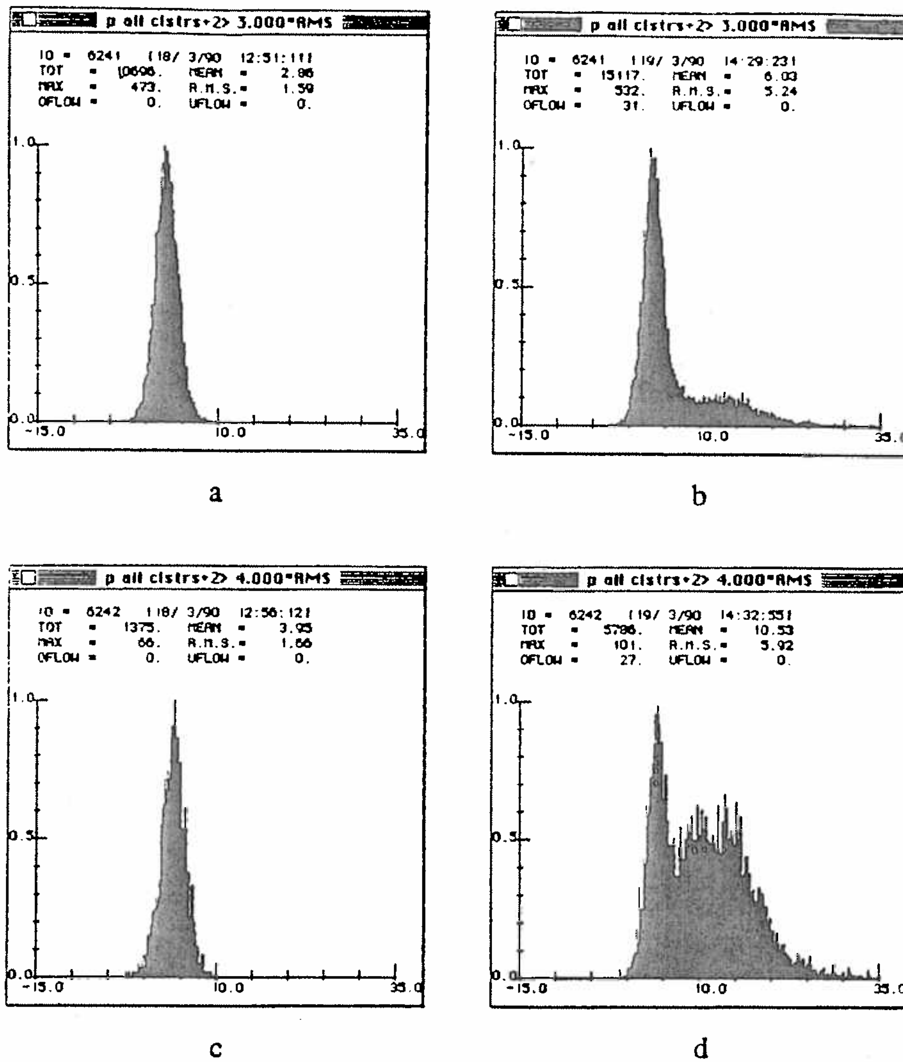

Figure 4.7. Results of beta measurements for a one-sided strip detector. a and c present the system noise, obtained with continuous triggering. b and d present the results when scintillator triggering is used (Publication I).

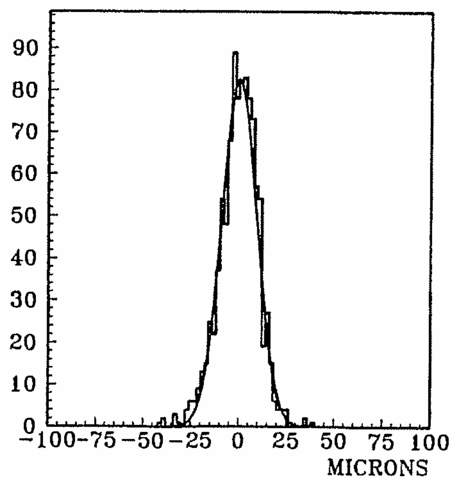

Figure 4.8. Result of the cluster analysis to obtain the position resolution (Hietanen et al. 1991 (2)).

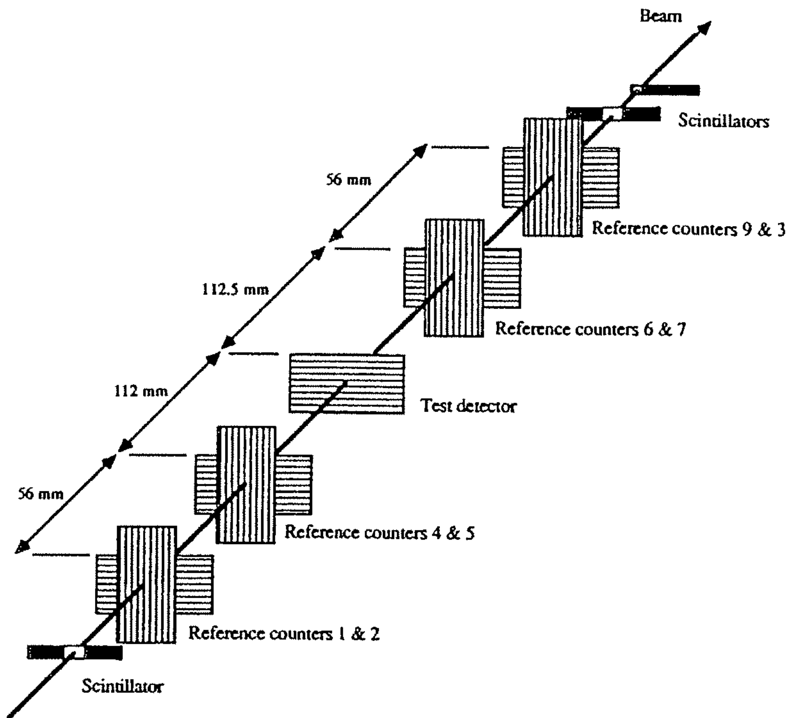

Figure 4.9. Measurement of the position resolution (Hietanen et al. 1991 (1)).

For efficiency calculations the signals of three strips around the predicted impact point on the tested detector were studied. The probability to find a $4.5 \cdot \mathrm{RMS}$ signal in one of the three strips was 0.996 . This figure includes also the inefficiency of the electronics. No pedestal, noise etc. cuts were used when selecting the events.

4.4 SEM measurements

As explained in chapter 1.4, the luminosity of the accelerators is continuously increasing. This places the particle detectors in to a very harsh environment. The radiation will cause irreversible damage in the detector bulk material. At a macroscopic level the leakage current will increase, the depletion voltage will change and the charge collection efficiency will decrease.

The diode depletion voltage is proportional to the absolute value of the effective doping concentration N_{eff} (solved from equation 2-16)

$$|N_{eff}| = 2\,\varepsilon \cdot \frac{V_{dep} - V_0}{q\,W^2} \quad , \qquad (4\text{-}4)$$

where ε is the absolute dielectric constant of silicon, q is the electron charge, W is the diode thickness and $V_0 \approx 0.6$ V is the junction built-in potential. Defects generated by radiation in the substrate cause variation of the effective doping concentration and consequently of V_{dep} . The two microscopic mechanisms related to the N_{eff} variation in n-type float zone (FZ) silicon

are the donor removal and the deep acceptor generation, which are macroscopically modeled as a function of the particle fluence Φ by

$$N_{eff} = N_{eff,0} \cdot e^{-c\Phi} - \beta\,\Phi \qquad , \qquad (4\text{-}5)$$

where $N_{eff,0} > 0$ is the donor concentration before irradiation, c is the donor removal coefficient and β is the acceptor introduction rate. By increasing the fluence, N_{eff} decreases up to type inversion of the semiconductor bulk, that is the density of the radiation induced deep acceptors causes N_{eff} to become negative. Beyond type inversion, the $| N_{eff} |$ increase is proportional to the particle fluence ($| N_{eff} | \propto \beta\,\Phi$) (Candelori). This behavior is visualized in figure 4.10 for 10 MeV proton irradiation.

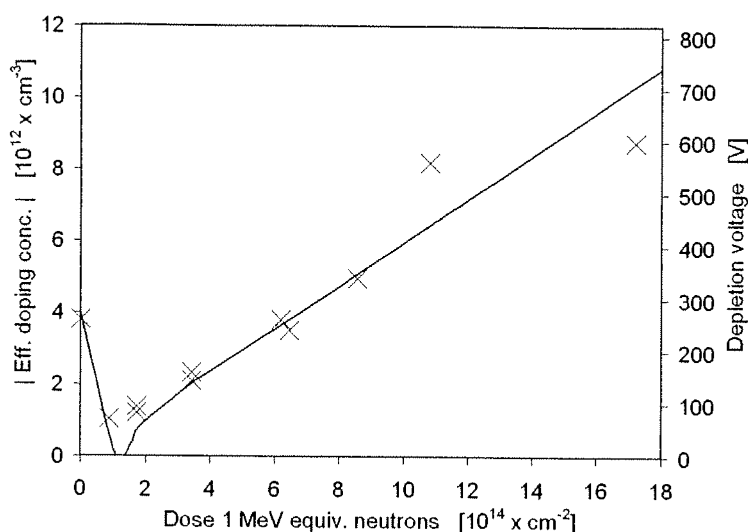

Figure 4.10. The evolution of the effective doping concentration (N_{eff}) in n-type FZ-Si pad detectors irradiated with 10 MeV protons. Crosses are CV-measured points, and the solid line is a tendency curve.

Type-inversion means that an irradiation fluence-threshold exists above which the n-type bulk material becomes p-type. This process is connected to the Space Charge Sign Inversion (SCSI) effect (Beattie et al., Li et al. 1999) and gives rise to a nearly intrinsic bulk, slightly p-type, for fluences next to the inversion point. It also seems like two depleted regions originate at the extreme sides of the device from the two contacts for fluences above the inversion threshold. This is called a double-junction effect (Li et al. 1992, Casse et al., Leroy et al.).

The type inversion and the double-junction effect have been investigated with several indirect methods: capacitance-voltage (CV) measurements, which yield the depletion voltage and the effective doping concentration, transient current technique (TCT), which gives information about the position of the electric field maximum inside the detector through observing the shape and the delay of a current pulse after generating carriers near one surface of the detector with a short laser pulse (Eremin & Li, Eremin et al. 1996), optical beam induced current (OBIC) (Castaldini et al.) and measuring the surface potential with a mechanical probe from a cleaved sample (Castaldini et al.). The electric field profile has also been calculated based on the material data got from various measurements (Eremin et al. 2004). The voltage-contrast effect in the scanning electron microscope (SEM) provides a more direct way to measure the desired quantities, voltage and electric field, inside the detector structure.

Figure 4.11 presents the physical measurement system. The drawing displays how a split detector is placed in the vacuum chamber of the scanning electron microscope into an upright position. The bias voltage is fed over the detector from an Agilent semiconductor parameter analyzer, V_{SMU} and its associated voltage (V) and current (A) meters constituting one SMU (Source Measure Unit). In line scan measurements the electron beam scans over the cross section of the split detector from left to right at a speed of 2 to 5 μm/s. In voltage-contrast imaging, 800 or 2000 horizontal lines are scanned at a speed of 20 or 40 ms/line.

The primary 5 keV electron beam generates secondary electrons at most a few nanometers below the examined surface. These electrons are pulled to a secondary electron detector (SEI = Secondary Electron Image) by a positive voltage V_{SEI} around this detector. The value of V_{SEI} is fixed to 10 kV in this microscope. The secondary electron signal is amplified and converted digital in a 12-bit ADC. This signal plus the horizontal and vertical timing signals of the scanning electron microscope are read to a PC using a homemade c++ software. In line scan measurements 850 contrast values are converted and saved per one scanned line. In voltage-contrast imaging the resolution was 440 x 400 or 850 x 680 pixels.

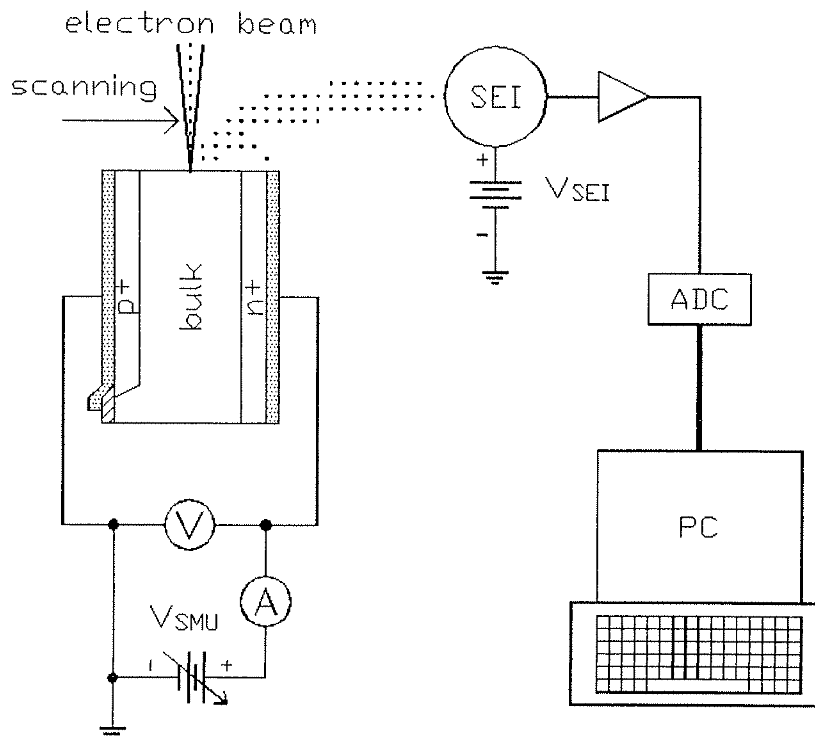

Figure 4.11. The principal construction of the measurement system. An electron beam scans over the cross section of the biased detector. The generated secondary electrons are detected, amplified and AD-converted. A PC software displays the images and waveforms and calculates voltages and electric fields.

The energy of the secondary electrons is small, less than 50 eV . So even a small positive voltage on the sample can decrease the number of electrons arriving to the secondary electron detector and hence cause a phenomenon called voltage-contrast. This has been utilized in the measurement of voltages and electric fields inside the detectors.

As important as the physical measurement system, is the software used to acquire the numerical data from the physical system. A simplified flow of the developed data acquisition software is listed in table 4.1.

Table 4.1. The data acquisition software.

```
sem.cpp

read the color palette for color images
        4096 RGB values
        PALETTI.TXT

wait for vertical sync and possible key strikes
        if first time
                D               stop data acquisition and display
                H               rapid High speed
                L               start  Line scan mode
        if key strike
                in case of  P   start  Picture mode
                in case of  L   start  Line scan mode
                in case of  O   start  spot mode
                in case of  D   stop
                in case of  Q   Quit the program
                in case of  K   change the channel  (SEI, horizontal scan, vertical scan)
                in case of  B   make the image area Black
                in case of  Z   adjust image contrast and brightness the same as in the sem display
                in case of  C   Colors on/off
                in case of  F   save line scan file  VIIVAi.CSV
                in case of  G   save image file  KUVAj.BMP
                in case of  Y   save a combination file (screen capture)  KUVAj.BMP
                in case of  V   photo speed     850 x 680 pixels, 80 s/frame, 40 ms/line
                in case of  S   Slow speed      440 x 400 pixels, 10 s/frame, 20 ms/line
                in case of  R   Rapid speed                       0.5 s/frame, 1 ms/line
                in case of  H   High speed                        0.02 s/frame, 0.12 ms/line
                in case of  T   Test mode  (bypasses synchronization)
                in case of  0   integration off
                in case of  1-8 integrate  2^(1-8)  frames
                in case of  9   integrate continuously

Picture mode:
        y times
                wait for horizontal sync
                read one line
                draw one line
                integrate

Line scan mode:
        wait for horizontal sync
        x times
                read one value
                draw one value
                integrate
        calculate line minimum, average and maximum values

Spot mode:
        read  x
        read  y
        update image
```

The method to measure the voltage and the electric field inside a biased radiation detector is explained in detail in Publication IV. The measured contrast values are first converted to voltages according to equation

$$V = -M \ln(1 + C/K) \quad , \qquad (4\text{-}6)$$

where V is the voltage, C the contrast, and the contrast scaling factor K and the voltage constant M are found with the procedure described in Publication IV. After finding out the voltage curve, the procedure is opposite to the one described in chapter 2.1: the voltage curve is differentiated to get the electric field curve,

$$E = -\frac{dV}{dx} \quad . \qquad (4\text{-}7)$$

Using the Poisson's equation, we can further differentiate the electric field curve to get the charge density ρ,

$$\rho = \varepsilon \frac{dE}{dx} \quad . \qquad (4\text{-}8)$$

The net doping density is found by dividing charge density ρ in the depletion region by the elementary charge q.

Figure 4.12 displays the SEM voltage measurement result of a non-irradiated sample with a doping density of about $3 \cdot 10^{12}$ cm^{-3} at eight bias voltages. This should be compared qualitatively with figure 2.6, where similar curves were drawn analytically.

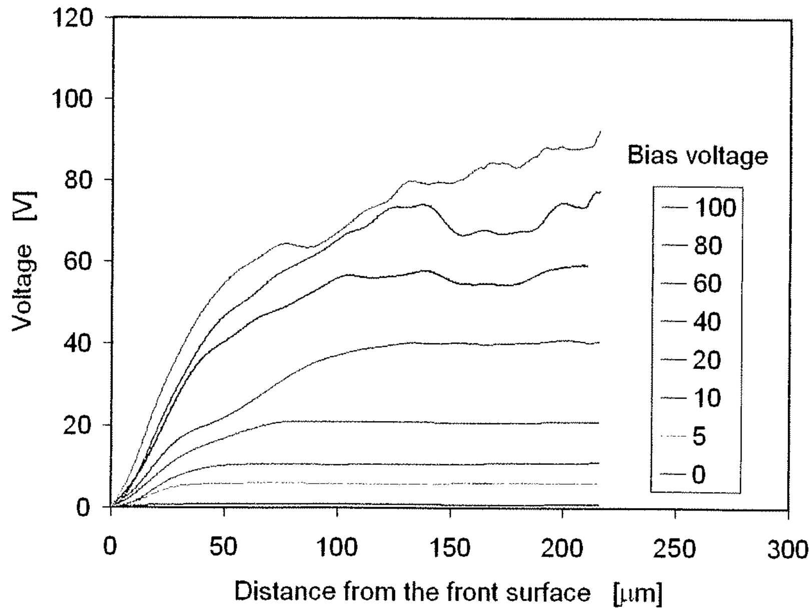

Figure 4.12. The voltage distribution in a non-irradiated radiation detector at eight bias voltages.

It is clear that the SEM method produces nice results up to 40 volts, but at higher voltages there will be noise originating from the fact that the dependence of voltage on the contrast is very steep above 40 volts. Differentiation enhances the noise, but by a suitable averaging this noise can be kept tolerable, and rather satisfactory electric field curves can be generated at least up to 100 volts which was the highest tested bias voltage. The measured electric field curves are displayed in figure 4.13. The results of 2D simulations with Silvaco software (Silvaco International) are shown in figures 4.14 and 4.15.

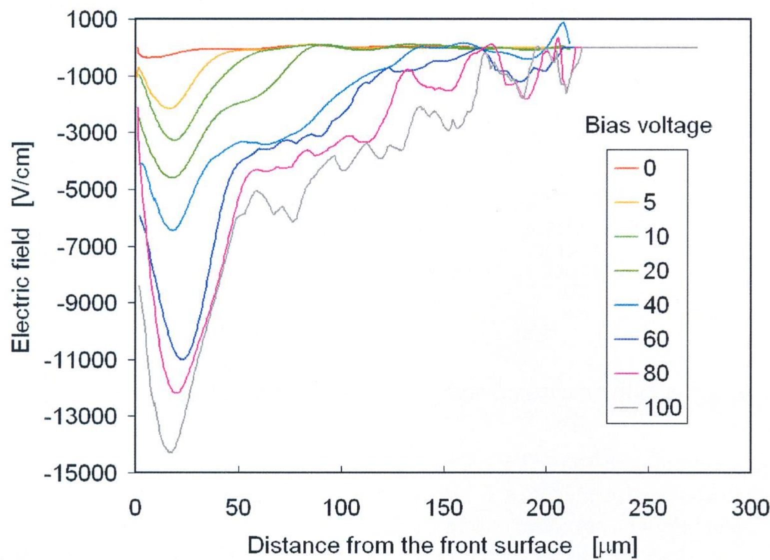

Figure 4.13. The electric field curves in the same detector.

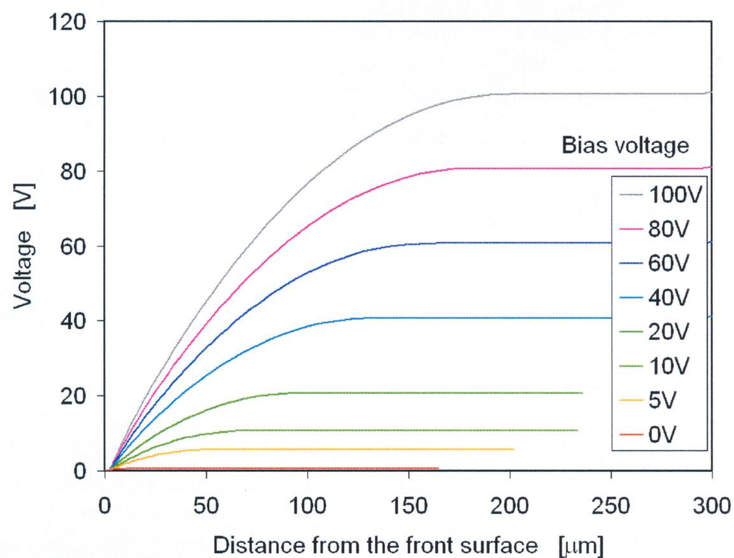

Figure 4.14. Simulated voltage curves in the same detector.

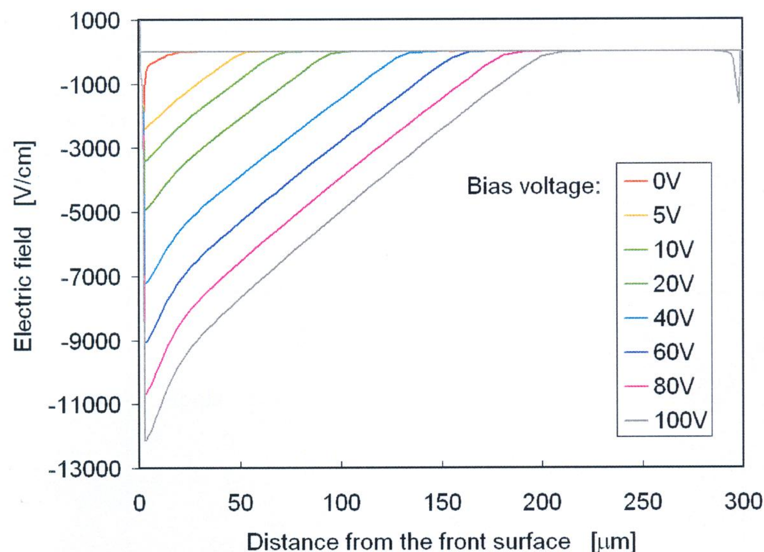

Figure 4.15. Simulated electric field curves.

The main difference between the measured and the simulated curves is the noise above 40 volts in the measured curves.

Comparing the peak positions in figures 4.13 and 4.15 reveals that the peak of the electric field is deeper in the measured result than in the simulated result. This can be partly explained by the averaging: because of the very steep slope of the electric field on the p-side and a gentle slope on the n-side, the peak seems to travel towards the n-side. This averaging effect comes from the calculation but maybe partly also from the measurement physics. The accuracy could be improved by investigating the junction with a higher magnification. In the case of a very lightly doped n-side in a radiation detector this is however not possible, because the voltage calibration requires that all the depletion region must be seen during the measurement. The bias voltage at the detector also causes the voltage-contrast curves to travel a little in horizontal direction. The curves were considered to travel as whole: no local variation was observed. This phenomenon was however not investigated further.

The parameters of the SEM voltage-contrast measurement were developed with a non-irradiated detector. The main purpose was however the investigation of irradiated detectors. With other methods it was deduced earlier that a radiation fluence threshold exists, above which the n-type bulk of a p+/n-/n+ radiation detector inverts its type to p. An electric field maximum also develops near the backside of the detector; this is called the double-peak effect. The former investigations showed however an exception: samples irradiated with high energy protons seemed not to have the double peak, but this was uncertain, and there seemed to be differences with the silicon wafer type, if it was Czochralski (CZ) or Float Zone (FZ) grown.

A series of measurements were made to confirm the earlier observations and to get new information. Two FZ detectors irradiated with 10 MeV protons with a fluence near to the kink in figure 4.10 ($\Phi = 1.09 \cdot 10^{14}$ cm^{-2}) and a higher fluence ($\Phi = 6.45 \cdot 10^{14}$ cm^{-2}) were analyzed with the SEM voltage-contrast method for Publication V. Four detectors with the energies and fluences given in table 4.2 were further measured to see the differences between high-energy and low-energy protons and with FZ and CZ silicon. The measured voltage curves are displayed in figures 4.16 to 4.19 and the electric field curves in figures 4.20 to 4.23.

Table 4.2. Irradiation energies and fluences of SEM samples.

	FZ	CZ	1 MeV neutron equivalent fluence
10 MeV	$2.5 \cdot 10^{14}$ p/cm^2	$2.5 \cdot 10^{14}$ p/cm^2	$1.1 \cdot 10^{15}$ n_{eq}/cm^2
24 GeV	$3.0 \cdot 10^{15}$ p/cm^2	$3.0 \cdot 10^{15}$ p/cm^2	$1.8 \cdot 10^{15}$ n_{eq}/cm^2

For the transformation of the proton fluence values for 10 MeV and 24 GeV to the equivalent values of 1 MeV neutron fluence, the hardness factors 4.32 and 0.6, respectively, were used (Vasilescu & Lindstroem).

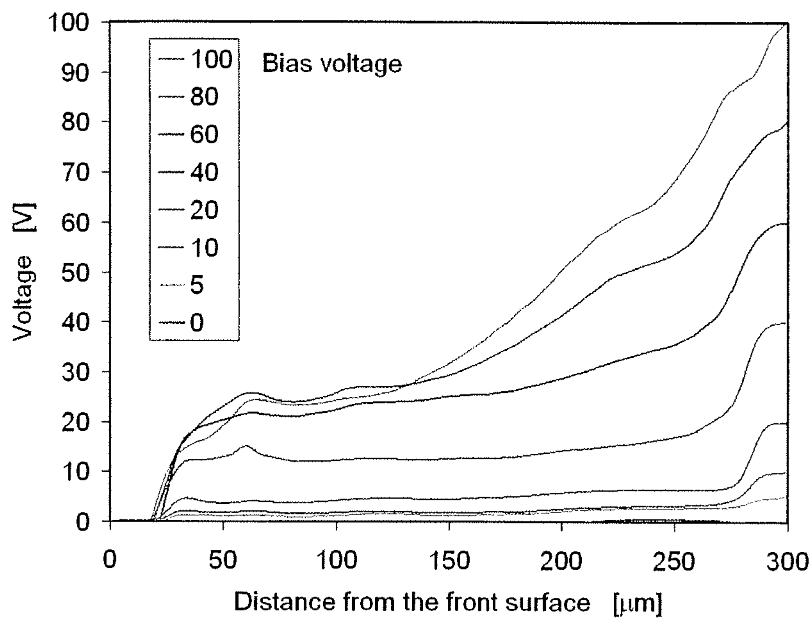

Figure 4.16. The voltage curves in the FZ sample irradiated with 10 MeV protons with a 1 MeV neutron equivalent fluence of $1.1 \cdot 10^{15}$ n/cm^2.

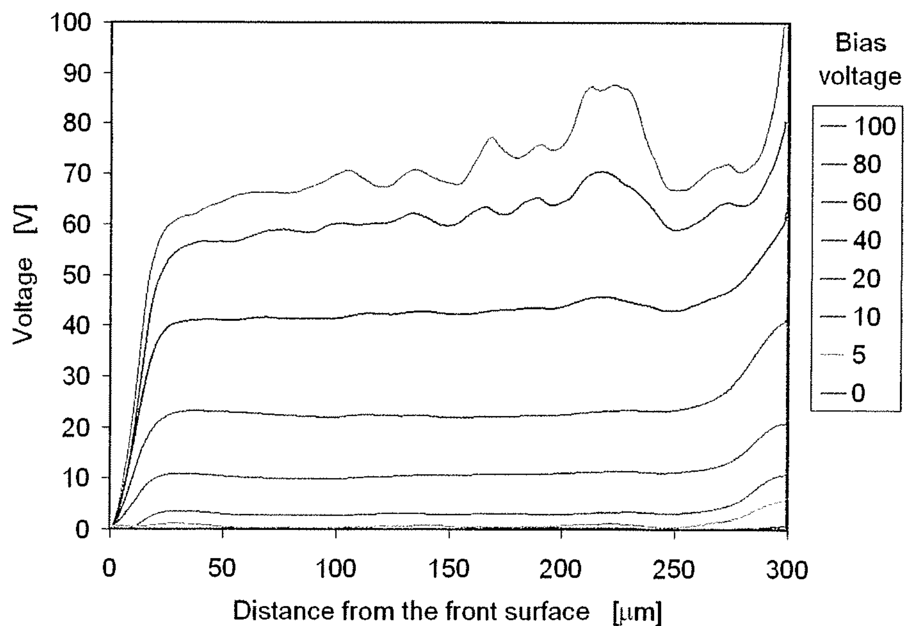

Figure 4.17. The voltage curves in the CZ sample irradiated with 10 MeV protons with a 1 MeV neutron equivalent fluence of $1.1 \cdot 10^{15}$ n/cm^2.

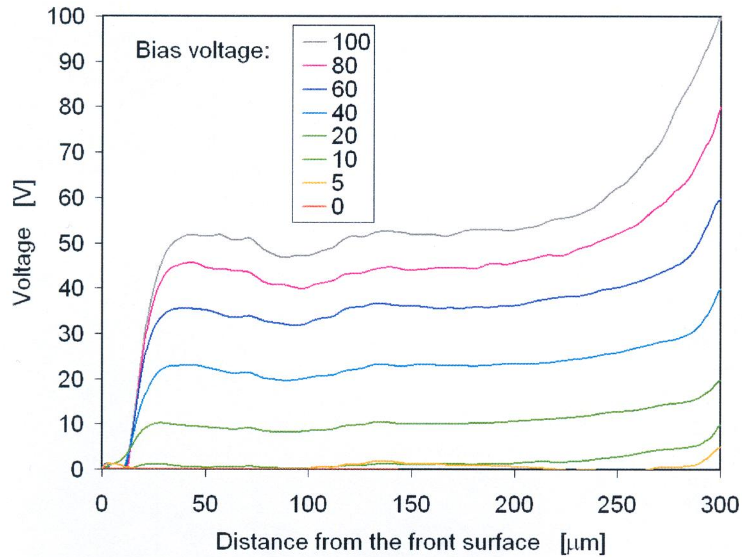

Figure 4.18. The voltage curves in the FZ sample irradiated with 24 GeV protons with a 1 MeV neutron equivalent fluence of $1.8 \cdot 10^{15}$ n/cm^2 .

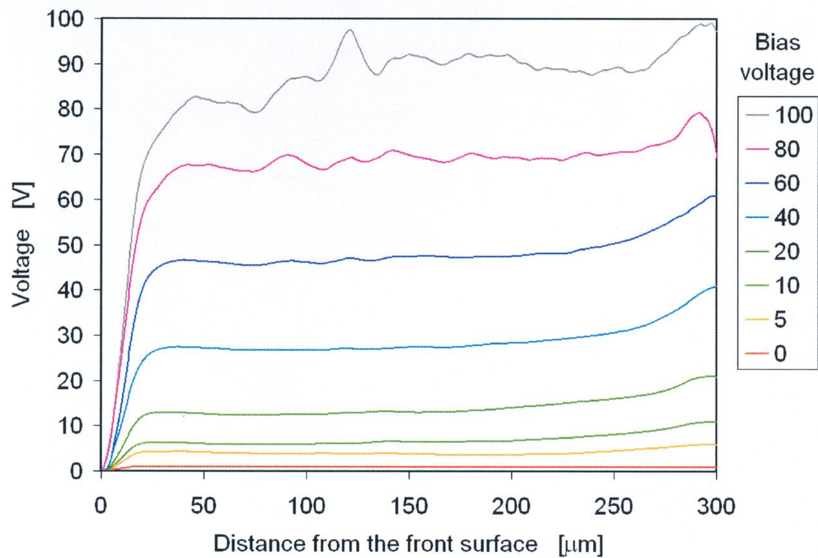

Figure 4.19. The voltage curves in the CZ sample irradiated with 24 GeV protons with a 1 MeV neutron equivalent fluence of $1.8 \cdot 10^{15}$ n/cm^2 .

In the voltage curves it is easy to see that the depletion of the bulk starts from the back in all samples except the CZ detector irradiated with 24 GeV protons, where the depletion starts from the front. This is not however the only result of this detector. In some measurements the

depletion starts from the back at low bias voltages, but at larger bias voltages the detector starts to deplete mainly from the front side.

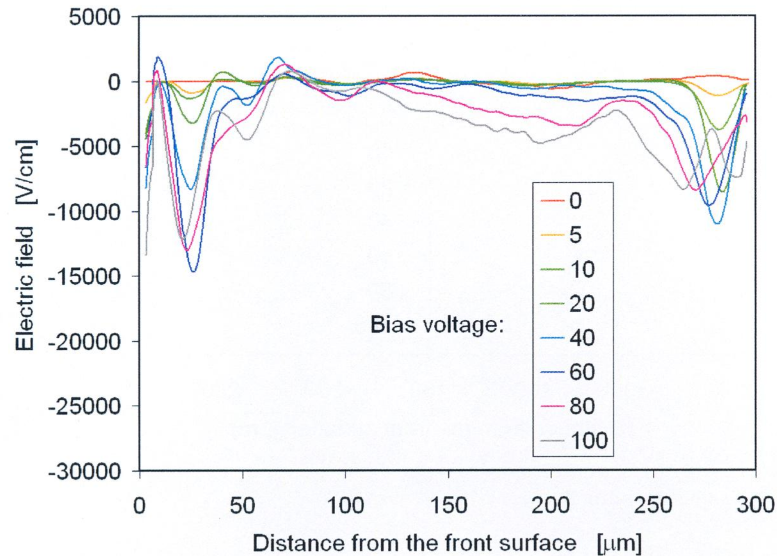

Figure 4.20. The electric field curves in the FZ sample irradiated with 10 MeV protons with a 1 MeV neutron equivalent fluence of $1.1{\cdot}10^{15}$ n/cm^2 .

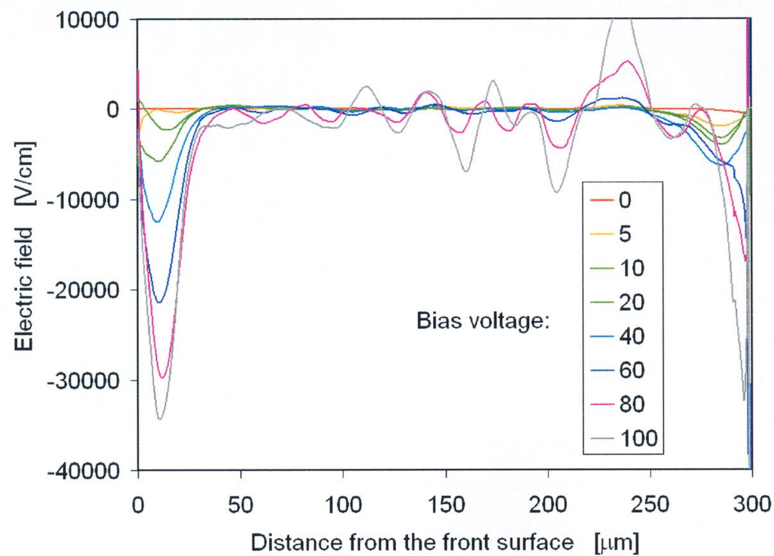

Figure 4.21. The electric field curves in the CZ sample irradiated with 10 MeV protons with a 1 MeV neutron equivalent fluence of $1.1{\cdot}10^{15}$ n/cm^2 .

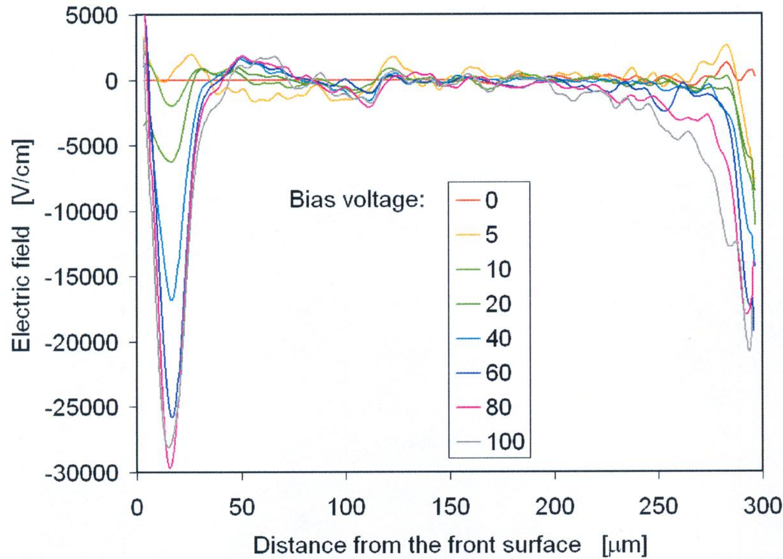

Figure 4.22. The electric field curves in the FZ sample irradiated with 24 GeV protons with a 1 MeV neutron equivalent fluence of $1.8 \cdot 10^{15}$ n/cm^2 .

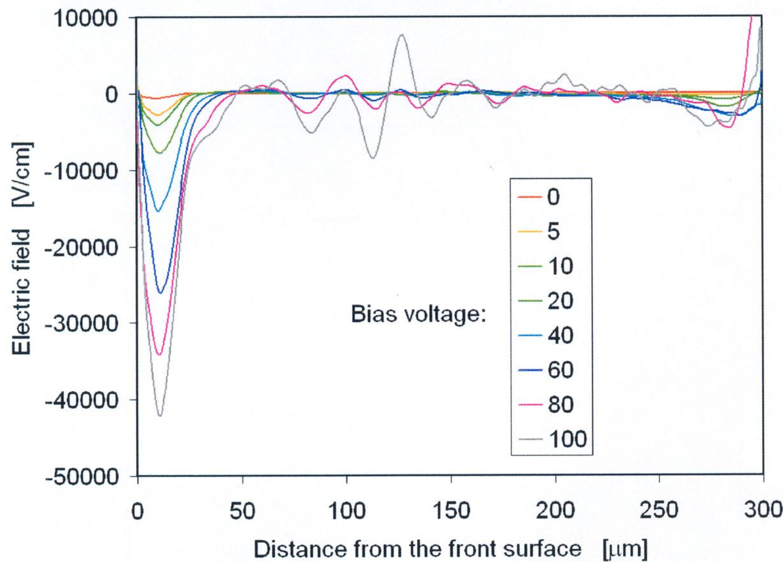

Figure 4.23. The electric field curves in the CZ sample irradiated with 24 GeV protons with a 1 MeV neutron equivalent fluence of $1.8 \cdot 10^{15}$ n/cm^2 .

Considering the electric field curves, the double-peak effect is very clear in all other detectors except the CZ detector irradiated with 24 GeV protons. A very small second peak exists also in that detector, but in no measurement this peak was of comparable intensity with the front side

peak. The differences between these four charts indicate that CZ silicon is more radiation tolerant than FZ silicon, especially considering that the 1 MeV neutron equivalent fluence was a little higher with 24 GeV than with 10 MeV .

At these bias voltages an area of very low electric field intensity exists in the central part of the detectors, which could decrease the charge collection efficiency. Also the leakage current during the SEM measurements was very high in every irradiated detector. An electron beam induced current (EBIC) measurement was tried to test the charge collection efficiency of the irradiated detectors, but with no success. The EBIC measurement did not prove that the detectors were bad; it just proved that the method was not suitable.

Chapter 5

Conclusions

Individual process steps and the total processes to fabricate defect free low leakage current silicon position sensitive particle detectors for high energy physics applications were developed in this work. One of the most important individual subjects was the development of the best oxidation parameters to reduce the surface state density and further the detector leakage current. The leakage current was further minimized by finding optimum gettering conditions to remove harmful metallic impurities from the active volume of the detector thus increasing and maintaining the carrier lifetimes. Accurate and stable polysilicon resistors were also developed. The main product after the initial development period was the double-sided ac-coupled strip detector with integrated coupling capacitors and bias resistors. Many details of its structure, like the polysilicon field plate ring around the ends of n-strips, were developed during this work.

After processing a few batches of strip detectors, the need to automate the patterning of large area detectors grew urgent. A new method was developed to pattern large area strip detectors with a reduction wafer stepper.

After developing the detector structures and good manufacturing processes, a need for a better radiation tolerance became evident. Ever increasing luminosities of the particle accelerators made the well made semiconductor detectors suffer. The high radiation fluence causes damage to the detector bulk material, decreases carrier lifetimes, decreases the charge collection efficiency and increases the leakage current dramatically.

All aspects related to the radiation damage in semiconductor particle detectors are not yet understood. In this work a scanning electron microscope method was developed to measure directly the electric potential and field inside irradiated radiation detectors to shed light on the observed phenomena, like type reversal of n-type bulk material and the double-junction effect. The accuracy of the voltage measurement was very satisfactory for this purpose, but there is still room for further development: increasing the voltage measurement accuracy and the electric field peak position accuracy and understanding better the physics in the specimen chamber of the scanning electron microscope during voltage-contrast measurements.

New materials, new structures and new fabrication processes must now be developed so that the semiconductor particle detectors will survive in the nasty radiation environment of future high luminosity particle accelerators like the LHC and the Super-LHC. It could even be found out the good fabrication practices like maintaining carrier lifetimes and decreasing surface states, is not relevant at all. The main question is now: what is the leakage current after five years of operation in a high luminosity environment.

The diagnosis given in this work, that the tradition to fabricate radiation detectors solely on <111> crystal oriented substrates is not necessarily correct, is now cured: most radiation detectors are now fabricated on <100> silicon, which decreases the surface state density and accordingly the leakage current. The sensitivity to mechanical breakage is however increased.

Traditionally silicon radiation detectors have been fabricated purely on float zone grown substrates because of its purity, higher resistivity, longer lifetimes and less defects compared to Czochralski grown silicon. The demand for better radiation tolerance has changed this situation. Good microstrip detectors can as well be fabricated on Czochralski silicon (Härkönen et. al). It is also found that Czochralski silicon, especially magnetic Czochralski silicon with suitable oxygen content, produces detectors with a better radiation tolerance than float zone silicon (Tuominen et. al). No charge collection data is however yet available.

References

Assmann R. W. for the LEP team, LEP luminosity revisited: design and reality, Proceedings of the Second Asian Particle Accelerator Conference, Beijing, China, 2001, pp. 74-78.

Beattie L. J., Brodbeck T. J., Chilingarov A., Hughes G., McGarry S. A., Ratoff P. N., Sloan T., The electric field in irradiated silicon detectors, Nuclear Instruments and Methods in Physics Research A 418 (1998), pp. 314-321.

Bruzzi M. for the RD50 Collaboration, Silicon and other sensor materials for CMS upgrade, Second CMS Workshop on Detectors and Electronics for SLHC July 12-13 2004, Imperial College, London.

Caccia M., Evensen L., Hansen T. E., Horisberger R., Hubbeling L., Peisert A., Tuuva T., Weilhammer P., Zalewska A., A Si Strip Detector with Integrated Coupling Capacitors, Nuclear Instruments and Methods in Physics Research A 260 (1987), pp. 124-131.

Candelori A. on behalf of the RD50 Collaboration, Radiation-hard detectors for very high luminosity colliders, Vertex 2004, 13.-18. September 2004, Menaggio-Como, Italy.

Casse G., Glaser M., Grigoriev E., Study of evolution of active volume in irradiated silicon detectors, Nuclear Instruments and Methods in Physics Research A 426 (1999), pp. 140-146.

Castaldini A., Cavallini A., Polenta L., Nava F., Canali C., Electric field distribution in irradiated silicon detectors, Nuclear Instruments and Methods in Physics Research A 476 (2002), pp. 550–555.

Eremin V., Li Z., Determination of the Fermi level position for neutron irradiated high resistivity silicon detectors and materials using the transient charge technique (TChT), IEEE Transactions on Nuclear Science vol. 41 (1994), pp. 1907-1912.

Eremin V., Strokan N., Verbitskaya E., Li Z., Development of transient current and charge techniques for the measurement of effective net concentration of ionized charges (Neff) in the space charge region of p-n junction detectors, Nuclear Instruments and Methods in Physics Research A 372 (1996), pp. 388-398.

Eremin V., Li Z., Roe S., Ruggiero G., Verbitskaya E., Double peak electric field distortion in heavily irradiated silicon strip detectors, Nuclear Instruments and Methods in Physics Research A 535 (2004), 622–631.

Evensen L., Avset B. S., Turan R., Finstad T. G., Boron Doped LPCVD Polysilicon: Reversible Variations of Resistance during Low Temperature Cycling, 14th Nordic Semiconductor Meeting, June 17-20, 1990, Århus, Denmark, Proceedings, pp. 179-182.

Fretwurst E., Hönniger F., Kramberger G., Lindström G., Moll M., Pintilie I., Röder R., Radiation tolerant epitaxial silicon detectors of different thickness, 6th RD50 workshop, Helsinki, 2-4 June 2005.

Grove A. S., Physics and Technology of Semiconductor Devices, John Wiley & Sons, 1967, 366 p.

Hietanen I., Lindgren J., Orava R., Tuuva T., Brenner R., Andersson M., Leinonen K., Ronkainen H., Hubbeling L., Turala M., Weilhammer P., Dulinski W., Husson D., Lounis A., Schaeffer M., Turchetta R., Chauveau J., Beam Test Results of an Ion-Implanted Silicon Strip Detector on a 100 mm Wafer, Nuclear Instruments and Methods in Physics Research A 305 (1991), pp. 173-176.

Hietanen I., Lindgren J., Orava R., Tuuva T., Brenner R., Andersson M., Leinonen K., Ronkainen H., Turala M., Weilhammer P., Dulinski W., Husson D., Lounis A., Schaeffer M., Turchetta R., Chauveau J., Beam Test Results of an Ion-Implanted Capacitively Coupled Silicon Strip Detector Processed on a 100 mm Wafer, Nuclear Instruments and Methods in Physics Research A 310 (1991), pp. 677-680.

Holland S., Fabrication of Detectors and Transistors on High-Resistivity Silicon, presented at the Workshop on Pixel Detectors, Leuven, Belgian, May 31 - June 2, 1988, published in Nuclear Instruments and Methods in Physics Research A 275 (1989), pp. 537-541.

http://cmsinfo.cern.ch/Welcome.html/CMSdetectorInfo/TrackingDetectors/page3.html

http://hands-on-cern.physto.se/hoc_v21en/index.html

http://hands-on-cern.physto.se/wired/ch/cern/wired/html/z0_1998_01.html

http://hyperphysics.phy-astr.gsu.edu/hbase/forces/funfor.html

http://greybook.cern.ch

http://particleadventure.org/particleadventure/frameless/chart.html

http://public.web.cern.ch/Public/Content/Chapters/AboutCERN/HowStudyPrtcles/CERNAccelComplex/CERNAccelComplex-en.html

http://public.web.cern.ch/Public/Content/Chapters/AboutCERN/HowStudyPrtcles/HowSeePrtcles/HowSeePrtcles-en.html

http://public.web.cern.ch/Public/Content/Chapters/AboutCERN/WhatIsCERN/InvolvedCountries/InvolvedCountries-en.html

Härkönen J., Tuominen E., Tuovinen E., Mehtälä P., Lassila-Perini K., Heikkilä P., Ovchinnikov V., Yli-Koski M., Palmu L., Kallijärvi S., Nikkilä H., Anttila O., T. Niinikoski T., Ereming V., Ivanov A. Verbitskaya E., Processing of microstrip detectors on Czochralski grown high resistivity silicon substrates, Nuclear Instruments and Methods in Physics Research A 514 (2003), pp. 173-179.

Kang J. S., Schroder D. K., Gettering in Silicon, Journal of Applied Physics, 65 (1989), pp. 2974-2985.

Kemmer J., Fabrication of Low Noise Silicon Radiation Detectors by the Planar Process, Nuclear Instruments and Methods 169 (1980), pp. 499-502.

Kemmer J., Burger P., Henck R., Heijne E., Performance and Applications of Passivated Ion-Implanted Silicon Detectors, IEEE Transactions on Nuclear Science, Vol. NS-29 (1982), pp. 733-737.

Kemmer J., Strahlungsdetektor mit einem passivierten pn-Halbleiterübergang, Patentschrift, DE 3003391 C2, Bundesrepublik Deutschland, 30.8.1984.

Kemmer J, Verfahren zur Herstellung von Halbleiterdetektoren, Offenlegungschrift, 2649078, Bundesrepublik Deutschland, 3.5.1978.

Kemmer J, Passivated Semiconductor Junction of High Electric Strength and Process for the Production thereof, United States Patent, 4,442,592, Apr. 17, 1984.

Kemmer J., Halbleiterdetektor mit niedriger Kapazität, Offenlegungschrift, DE 3415439 A1, Bundesrepublik Deutschland, 31.10.1985.

Kemmer J., Kombinierter Halbleiterdetektor, Offenlegungschrift, DE 3415426 A1, Bundesrepublik Deutschland, 31.10.1985.

Kemmer J, Halbleiterelement, Offenlegungschrift, DE 3427476 A1, Bundesrepublik Deutschland, 31.10.1985.

Kemmer J., Improvement of Detector Fabrication by the Planar Process, Nuclear Instruments and Methods in Physics Research 226 (1984), pp. 89-93.

Kern W., The Evolution of Silicon Wafer Cleaning Technology, Journal of the Electrochemical Society, Vol. 137 (1990), pp. 1887-1892.

Knoll G. F., Radiation Detection and Measurement, John Wiley & Sons, 2nd edition, 1989, 784 p.

Leroy C., Roy P., Casse G., Glaser M., Grigoriev E., Lemeilleur F., Study of charge transport in non-irradiated and irradiated silicon detectors, Nuclear Instruments and Methods in Physics Research A 426 (1999), pp. 99-108.

Lang A., Vanuxem J. P., CERN-EP-Electronics note 86-01 (1986).

Li Z., Dezillie B., Eremin V., Li C. J., Verbitskaya E., First charge collection and position-precision data on the medium-resistivity silicon strip detectors before and after neutron irradiation up to 2×1014 n/cm^2, Nuclear Instruments and Methods in Physics Research A 426 (1999), pp. 38-46.

Li Z., Kraner H. W., Fast neutron radiation effects in silicon detectors fabricated by different thermal oxidation processes, IEEE Transactions on Nuclear Science 39 (1992), pp. 577-583.

Millman J., Grabel A., Microelectronics, McGraw-Hill International Editions, Second Edition, 1987, 1001 p.

Muller, R. S., Kamins T. I., Device Electronics for Integrated Circuits, John Wiley & Sons, 1977, 404 p.

Pang S. K., Rohatgi A., Sopori B. L., Fiegl G., A Comparison of Minority-Carrier Lifetime in As-Grown and Oxidized Float-Zone, Magnetic Czochralski, and Czochralski Silicon, Journal of the Electrochemical Society, Vol. 137 (1990), pp. 1977-1981.

Quick Reference Manual for Silicon Integrated Circuit Technology, edited by Beadle W. E., Tsai J. C. C., Plummer R. D., John Wiley & Sons, 1985.

Schroder D. K., Semiconductor Material and Device Characterization, John Wiley & Sons, 1990, 599 p.

Silvaco International, http://www.silvaco.com.

Tuominen E., Härkönen J., Tuovinen E., Lassila-Perini K., Luukka P., Mehtälä P., Nummela S., Nysten J., Zibellini A., Li Z. , Heikkilä P., Ovchinnikov V., Yli-Koski M., Laitinen P., Pirojenko A.; Riihimäki I., Virtanen A., Radiation Hardness of Czochralski Silicon studied by 10 MeV and 20 MeV protons, IEEE Transactions on Nuclear Science 50 (2003), pp. 1942-1946.

Vasilescu A., Lindstroem G., Displacement damage in silicon, on-line compilation, http://sesam.desy.de/members/gunnar/Si-dfuncs.html

Walton J. T., Haller E. E., Silicon Radiation Detectors - Materials and Applications, Material Research Society Symposium Proceedings, Vol. 16 (1983), pp. 141-160.